Protonic Conduction in Porous Oxides

Sindre Østby Stub

Dissertation for the degree of Philosophiae Doctor

Department of Chemistry
Faculty of Mathematics and Natural Sciences

UNIVERSITY OF OSLO

March 2017

Series of dissertations submitted to the
Faculty of Mathematics and Natural Sciences, University of Oslo
No. 1864

ISSN 1501-7710

Cover: Hanne Baadsgaard Utigard.
Print production: Reprosentralen, University of Oslo.

Preface

This dissertation represents part of the work required for the degree of Philosophiae Doctor (PhD) at the Department of Chemistry, Faculty of Mathematics and Natural Sciences, University of Oslo. The doctoral scholarship has been funded by The Research Council of Norway through the project "Nanoceramics – a new class of proton conductors for hydrogen fuel cells and electrolysers" (NaProCs, #216039*) within the RENERGI program. The work has been carried out at Centre for Materials Science and Nanotechnology (SMN) at the Section for Solid State Electrochemistry (FASE) during the period from September 2013 to March 2017 under the supervision of Professor Truls Norby, Dr. Einar Vøllestad and Professor Reidar Haugsrud.*

First of all, I would like to thank my main supervisor, Truls Norby, for the collaboration, allowing me to work independently and develop my own ideas, and for the many stimulating discussions when everything looked like most hopeless. I am also very grateful for all constructive tips and helpful advice I have got from Reidar Haugsrud, and not to mention all discussions in the mornings about everything important for living the life during the PhD period. I would also give special thanks to Einar Vøllestad who joined the project during the second year. Your door was always open; you had always time for a discussion. And maybe the most important; guiding me from hopeless paper drafts to almost complete manuscripts. It is safe to say that this work would never have been this good without your help!

I would also thank all colleagues involved in the NaProCs project at Sintef Materials and Chemistry, especially Drs. Per Martin Rørvik and Knut Thorshaug. I would like to acknowledge Professor Sangtae Kim for stimulating discussions during my stay at UC Davis.

A big "thank you" also goes to all former and present colleagues at FASE. I will especially thank Matthias Schrade and Andreas Løken for all fruitful scientific discussions and all discussions just about life. And, I am very thankful to Anna Evans and Ragnhild Hancke for all their help with proofreading of manuscripts and the thesis.

I am very grateful to my parents and family for all support and all good moments throughout life. My warmest feelings and gratitude finally goes out to my dearest Sigrid, who is always there for me.

Oslo, March 2017

Sindre Østby Stub

Summary

Nanocrystalline porous oxides are recently shown to exhibit high protonic conduction at ambient and moderately elevated temperatures in wet atmospheres, and have thus gained interest as candidate materials for energy conversion technologies such as fuel cells and electrolysers. It is well established that the protonic transport in nanocrystalline porous oxides is related to adsorption of chemisorbed and physisorbed water on the pore surfaces. However, there has been a lack of fundamental understanding of the relation between the conductivity, the concentration of water, formation of protonic charge carriers, and the transport mechanism. Understanding protonic surface transport can form a basis for improvements and utilisation of a new class of proton conductors.

The present work comprises investigations of the protonic conductivity in porous oxides at various temperatures and partial pressures of water. Porous samples of yttria-stabilised zirconia (YSZ) and titania (TiO_2) are chosen as model systems, as they previously have shown high protonic surface conductivity at low temperatures, while having well-established bulk transport properties at elevated temperatures.

The electrical properties of porous YSZ samples are investigated by impedance spectroscopy and show that the protonic surface conduction under wet conditions displays two distinct transport processes connected in series; *intra-grain* and *inter-grain* transport. *Intra-grain* transport is related to transport along the surface of individual grains whereas the *inter-grain* transport is related to the transport between adjacent grains. A modified brick layer model and an equivalent circuit for parallel ionic volume transport through the oxide matrix and protonic surface transport is presented and discussed.

Adsorption measurements show that the water layer thickness on the surfaces of porous oxide is less than 1.5 nm for typical conditions used for studies of porous oxides. The protonic transport through the water layer is therefore strongly influenced by the interface between the oxide surface and the water layer. The concentration of protonic charge carriers is found to depend on the acid-base reaction between the adsorbed water and the dominating acidic sites on the surface of the host oxide matrix. Moreover, intra-grain transport on grain surfaces is shown to be highly dependent on the water layer thickness, where the mobility and defect formation increase exponentially with the water layer thickness until it shows liquid-like properties around 1 nm. The protonic intra-grain conductivity of porous YSZ samples is shown to increase by three orders of magnitude (~10^{-8} to 10^{-5} Scm^{-1}) as the relative humidity is increased from 20% to 84%. This is attributed to increasing formation and mobility of

protons as the activation energy is shown to decrease from 0.43 to 0.28 eV from low to high relative humidity.

Inter-grain transport across grain boundary intersects is shown to be highly resistive, attributed to a depletion of the protonic charge carriers above the positively charged grain boundaries. The inter-grain conductivity increases from ~10^{-12} Scm^{-1} at a water layer thickness of 0.5 nm (13% RH) to 10^{-5} Scm^{-1} at a thickness of 1.5 nm (84% RH), measured at 25 ºC, as the depletion effect of the potential of the grain boundary decreases.

Fourier transform infrared spectroscopy and impedance measurements have been employed to investigate the acid-base properties and protonic surface conductivity of aliovalent doped porous TiO_2. The conductivity of donor doped samples is shown to be significantly higher than for undoped and acceptor doped samples, and the conductivity of donor doped samples is five and two times higher, at low and high relative humidity, respectively, at 25 ºC. This large difference in conductivity occurs because higher valent dopants make the surface more acidic and therefore increase the formation and mobility of protons, whereas acceptor dopants show the opposite effect.

Transport number measurements and H/D isotope studies of YSZ are applied to determine the type of charge carrier and charge carrier mechanism. By varying the relative humidity, the transport mechanism is shown to change from Grotthuss type migration of protons at low relative humidity to vehicular transport of hydroxonium ions (H_3O^+) when the relative humidity exceeds 60%. This coincides with when the water layer starts showing liquid-like properties. For basic surfaces Grotthuss type transport of proton holes and vehicular transport of hydroxide ions at low and high humidity, respectively, is expected.

Altogether, the present work highlights and investigates many of the most important aspects of protonic conduction in porous oxides. This has resulted in a deeper fundamental understanding of protonic surface conduction. The best protonic conductivity of a porous sample in this work lies in the range of 10^{-4} Scm^{-1}, far below the best material reported in literature which shows a similar conductivity as the state-of–the-art proton conducting electrolyte, Nafion (~0.1 Scm^{-1}). An advantage of the porous oxide proton conductors is that they can be made electronically conductive through aliovalent doping of the host oxide, unlike polymeric membranes which are exclusive ionic conductors. This may open new possibilities in making mixed conducting composite-like systems that could be used for instance as electrodes in low- and intermediate temperature electrochemical cells, which is crucial for realisation of nanocrystalline porous oxides as a new class of proton conductors in electrochemical devices.

Contents

1 Introduction

1.1 Motivation – develop a climate solution

It was inspiring to start the last year of my PhD with the awaited climate agreement in Paris in December 2015. Finally, the World's leaders managed to agree on a roadmap and target that is below the limit of what Nature can endure. The approved 2 °C target, which may even be sharpened to 1.5 °C, is a really challenging goal to achieve. It will force all countries to sharpen their domestic targets and instruments to decrease the emissions of climate gases.

In order to meet the 2 °C target, the CO_2 emissions in the period from 1861 to 2100 can be at most 2900 Gt. Already two thirds of this carbon budget is spent, and the rest of the budget is locked-in in existing infrastructure, industrial plants and power plants. Basically it means that we can meet the 2 °C target only in two ways: build all new infrastructures with zero emission technology, or implement large use of carbon negative strategies. The first option is obviously both cheaper and less risky.

Renewable energy must substitute carbon based energy, wherever it is used, to meet the 2 °C target. Photo voltaic (PV) solar cells are emerging as the most important technology for renewable energy production. Worldwide there is an exponential growth in installed capacity. PV has already reached grid parity in several areas around the world, such as in California, Germany and Argentina. With increasing amount of intermittent renewables on the market, the demand for storage, both short-term and more long-term, is also increasing. Batteries are already in use in a lot of vehicle models and also in smaller solar systems for buildings.

Hydrogen has for decades been foreseen as a candidate for more long-term energy storage and as a clean fuel for heavy transport and shipping. Hydrogen technology has however just recently been introduced into the first serial produced vehicles (*e.g.* Hyundai iX35/Tucson 2014 and Toyota Mirai as of 2015) and has not had its big breakthrough yet.

Materials science will play an indispensable role in developing these environment friendly energy technologies. Our job as researchers is to show possibilities and develop technologies, and make the technologies better and cheaper so that clean technologies can reach the market. The policy-makers must on the other hand encourage the market, either by taxes on fossil fuels or by subsidies for renewables, so that renewables become cheaper than fossils.

The major drawback for the hydrogen technology is the low energy efficiency of the electricity-hydrogen-electricity conversion and expensive materials. In a system based on intermittent renewables, there is no doubt that the relative price of capacity will increase at the expense of the relative price of energy. If the policy-makers are doing their job and

encouraging the market, the surplus of cheap solar energy can perhaps pay for the drawback of the low energy efficiency of the electricity-hydrogen-electricity conversion? My scientific contribution to society is presented in this thesis, where the focus is on gaining new knowledge about proton conduction in porous oxides, a new class of materials for hydrogen-based fuel cells and electrolysers.

1.2 Fuel cells and electrolyser cells – technologies and challenges

Fuel cells convert chemical energy into electrical energy. Fig. 1.1, left, shows the principles of a proton conducting fuel cell. Hydrogen is oxidised at the anode, forming protons which migrate through the electrolyte and react with oxide ions (forming water) on the cathode side. The chemical potential gradient occurring from having H_2 on the anode side and O_2 on the cathode side gives rise to an electrical voltage. The current is collected by the electrodes and transported via an external circuit where electrical energy can be utilised. The principle of an electrolyser cell is depicted to the right in Fig. 1.1. Instead of creating a voltage, an external voltage is applied to split water into oxide ions and protons, followed by oxidation and reduction to O_2 and H_2, respectively. With a pure proton conducting membrane, the protons and electrons take separated ways through the electrolyser cell and can be collected on the cathode side. The ideal electrolyte is a pure proton conductor with at least 99% pure ionic conductivity for both purposes and 0.01 Scm^{-1} is considered as the minimum ionic conductivity needed in order to utilize the material for fuel cells and electrolysers cell [2].

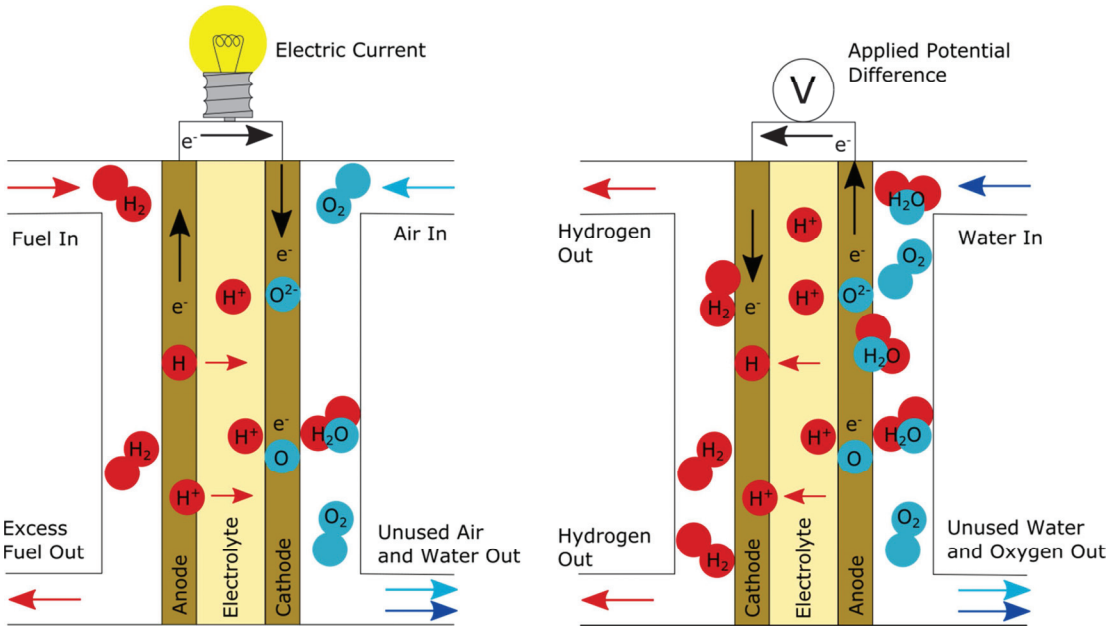

Fig. 1.1. Illustration of proton conducting fuel cell (left) and electrolyser cell (right).

Today's leading fuel cell technology is based on water-containing proton conducting polymer electrolytes, limiting the operating temperature to 100 ºC which necessitates the use of expensive platinum nano particles on the carbon electrodes to counteract slow electrode kinetics [3]. The tolerance to fuel impurities such as CO and H_2S is furthermore low due to high adsorption at the low operating temperature. Proton conducting ceramic fuel cell (PCFC), solid oxide fuel cell (SOFC), and solid acid fuel cell (SAFC) operating at higher temperatures have therefore been foreseen as alternative technologies, but have not achieved their breakthrough yet. The most important challenge for both SOFC and PCFC has been slow electrode kinetics at the cathode, and for SAFC the temperature is not high enough to avoid the use of expensive platinum.

1.3 Porous oxide – new type of proton conductor

Fig. 1.2 summarizes the conductivity versus temperatures for the different fuel cell (electrolyte) technologies. The latest addition to the family of proton conducting materials is porous oxides, marked in red in Fig. 1.2. They cover an important temperature range between the polymers and the high temperature oxides. In 2008 S. Kim *et al.* showed for the first time, a power generation at room temperature (RT) from nanocrystalline yttria-stabilised zirconia (YSZ) in a gradient of water [4]. This was surprising, as YSZ is known as a pure oxide ion conductor [5]. Protonic conduction was later observed also in nanocrystalline gadolinium-doped ceria (GDC) [6], and shown to be around 10^{-7} Scm^{-1} for both nanocrystalline YSZ and GDC in humidified atmosphere [7, 8].

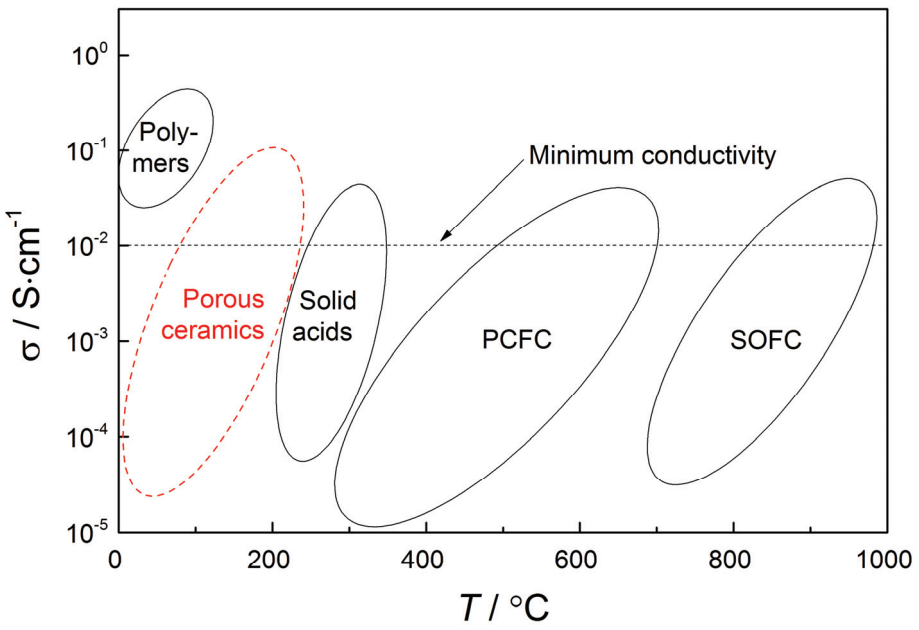

Fig. 1.2. Conductivity versus temperature for different fuel cell technologies. Conductivity data are based on [7, 9-12] and are just schematically drawn. I may therefore not be exact. Minimum ion conductivity to utilize the material for fuel cells and electrolysers cell are indicated.

Protonic conduction in nanocrystalline YSZ and GDC was initially met with scepticism since these oxides are known not to hydrate [5] and not to be proton conducting, and because such reports often reflect merely H_3O^+ or OH^- transport in liquid-like water. However, given these observations really reflect true protonic conduction, how is it possible that a pure oxide ion conductor can be transformed into a proton conducting material by making it nanocrystalline? Further, how are the protons incorporated into the material and what is the transport path in the material giving rise to such high conductivity?

S. Kim *et al.* suggested and substantiated shortly after the first reports that the proton transport is an interfacially controlled phenomenon where the protons migrate along the percolating grain boundaries [7]. H. J. Avila-Paredes *et al.* showed an inverse correlation between the conductivity and grain size, which could verify the hypothesis that the protons were conducted along the grain boundaries and explain why the highest conductivity was observed in samples with the smallest grains and largest specific surface area [13].

The proton conduction path has later been widely debated in literature, discussing whether the protons are conducted along the parallel grain boundaries, along the relatively open triple-grain boundaries, or in the layers of water adsorbed on the inner and outer surfaces [4, 7, 14-17]. B. Scherrer *et al.* showed that only thin films of YSZ with open porosity conducted protons under wet conditions at low temperatures [18]. Dense nanocrystalline samples showed no improvement upon switching from dry to wet conditions at low temperatures, showing that the conduction must take place in the adsorbed water layers on the sample. Several studies have later underpinned that the protonic conduction mostly occurs via chemisorbed and physisorbed water on the inner surface (pore) walls [18-21].

In the previous years, many observations of proton conductivity in nanocrystalline oxides have been reported. Fig. 1.3 summarizes some of the most important conductivity reports of different porous oxides under wet conditions. Films of meso-porous functionalised silica showed the highest conductivity with 0.1 Scm^{-1} at 90% RH at 100 °C [22]. The highest conductivity in a pure oxide was reported to be 3.8×10^{-2} Scm^{-1} at 80 °C and 81% RH in a thin film of TiO_2 back in 2006 [10].

It must be said that the introduction of porous oxides as a new class of proton conductors is slightly misleading as several older studies reporting on proton conduction in porous oxides can be found in literature. These include proton transport on silica, investigated back in 1964 [23], proton transport on YSZ powder [21], and not to mention the works investigating the use of porous oxides as humidity sensors, *e.g.* summaries given in Refs. [24, 25]. In retrospect, what was new almost ten years ago was that it was shown that the new class of proton-conducting materials could be utilised in applications and had taken the first stage from pure basic research.

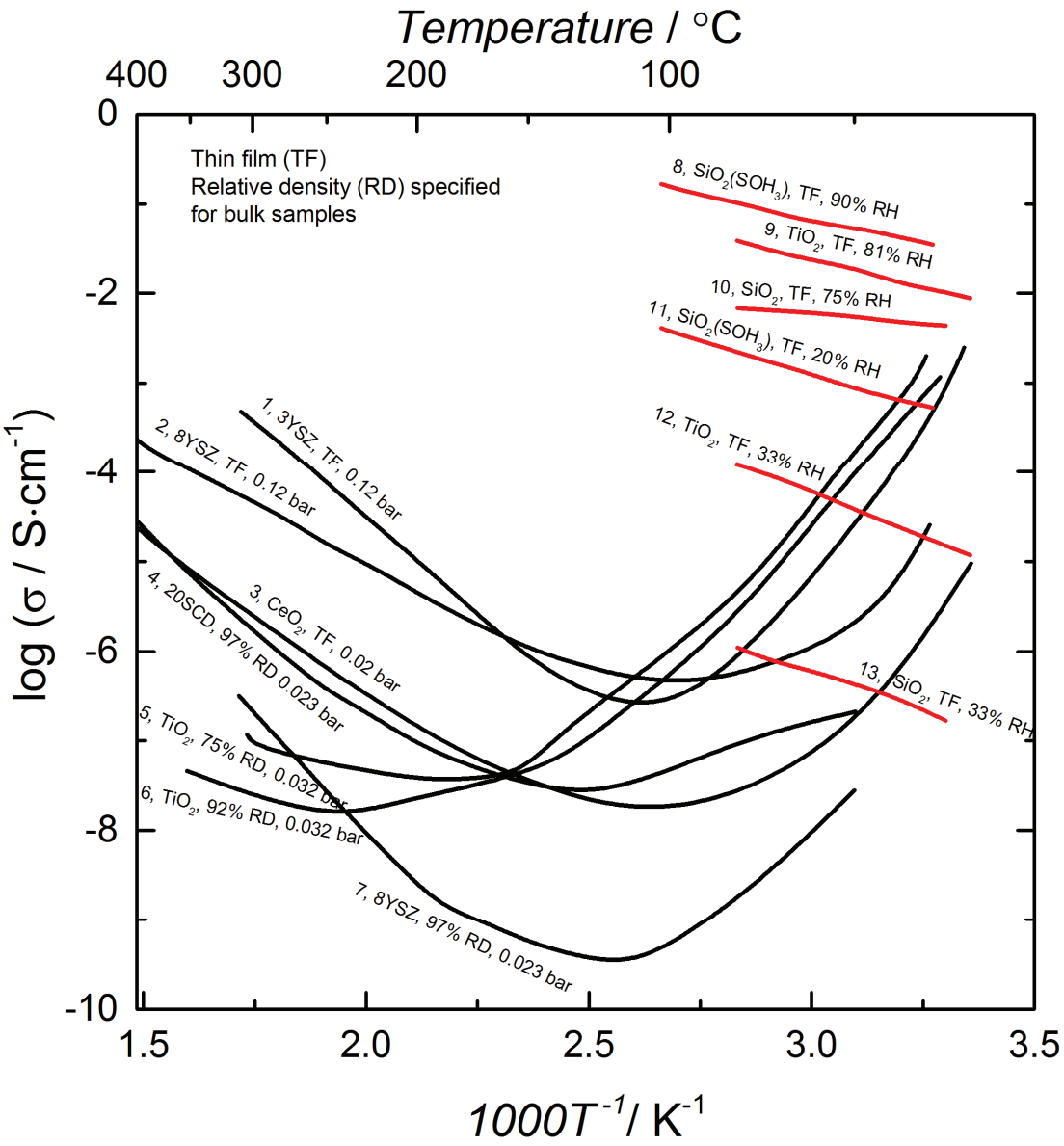

Fig. 1.3. Conductivity of different porous oxides under fixed partial pressure of water (given in bar) or under fixed relative humidity (RH). Relative densities (RD) of samples are specified, porous thin film is marked with TF. 1: 3YSZ [18], 2: 8YSZ [18] 3: CeO_2 [14], 4: 20SCD [26], 5: TiO_2 [20], 6: TiO_2 [20], 7: 8YSZ [26], 8: SOH_3 functionalised SiO_2 [22], 9: TiO_2 [10], 10: Silica xerogel [27], 11: SOH_3 functionalised SiO_2 [22], 12: TiO_2 [10], 13: Silica xerogel [27].

1.4 Aim and content of the thesis

Low temperature protonic conduction is, as presented in the previous subsection, by now reported for many different types of porous oxides where the conductivity at intermediate and low temperature shows similar behaviour. The primary objective of this thesis is therefore to get a fundamental understanding of protonic conduction in porous oxides and on oxides' surfaces and to study the applicability of the theory for different types of porous oxides. This

comprises not only hydration of the oxides, type of charge carrier, transport mechanism, charge carrier concentration, and mobility of the protonic charge carrier, but also methodologies to study conduction in porous oxides.

For high temperature proton conductors, the hydration reaction is an acid-base reaction, where hydration of the oxide and formation of protons is described by one reaction. In comparison, hydration of porous oxides and the acid-base reaction giving rise to protonic charge carriers are two separate reactions for porous oxides [19, 21]. They are to some degree derived in literature, but one important objective for this thesis is to understand the hydration and the acid-base properties of the porous oxide in more detail and relate it to the protonic conductivity of the samples.

There is also uncertainty regarding the type of protonic charge carrier, but for acidic oxides it is reasonable, as suggested by Miyoshi *et al.*, that it changes from protons (H^+) at higher temperatures to hydronium ions (H_3O^+) at lower temperatures [19], and perhaps to more hydrated protons as the number of water layers increase with decreasing temperature and higher relative humidity (RH). The term "protonic" is used in this work because the charge carrier is yet to be determined. During this work, the type of protonic charge carrier will be investigated.

Since the protonic conduction takes place in the very thin layer of adsorbed water on the oxide's surfaces [18], the properties of both the oxide's surfaces and the water layer are of great significance for the protonic conduction. The properties of both the oxide's surfaces and the water layer will differ significantly from their bulk properties. This is because the surfaces and interfaces show rearrangements of the surfaces relative to bulk to lower the overall free energy of the system. This normally results in a charged zone close to the interface where the local electroneutrality is not fulfilled. The charged zone typically consists of an interfacial core with adjacent space charge layers to compensate the charge of the core. An important objective of this thesis is therefore to understand and investigate how the space charge zone at interfaces and surfaces influence the protonic transport properties in porous oxides. The methodology and theory to investigate this are key topics.

Before the four manuscripts are presented in Chapter 5, I will first introduce the reader to fundamental knowledge of protonic conduction in porous oxides and interfaces in oxides. The experimental part in Chapter 4 should be considered as supplementary to what has been given in the manuscripts. Here, emphasis is put on the electrical measurements, especially impedance spectroscopy which is used as the main characterization technique. In Chapter 6 the most important perspectives of the manuscripts are discussed collectively. This overall discussion intends to sum up, bring the manuscripts together and allow for new insights. Finally, Chapter 7 offers some concluding remarks and gives some final perspectives on porous oxides as a new class of proton conductors.

2 Theoretical basis – proton conduction in porous oxides

As mentioned in the introduction, protonic conduction in porous ceramics has been shown to take place in the chemisorbed and physisorbed water layers on the pore surfaces under humidified conditions [18-21, 28]. The porous ceramics act as a host matrix for the water, and the properties of the surface and the water layer give rise to mobile protonic species that diffuse by thermal energy and can give rise to net charge transport under an electrochemical potential gradient. The properties of the porous oxides can in many ways be compared to proton conducting polymers. The proton conducting polymers - with all its nano channels - are able to keep the water inside the membrane, and the very acidic surface gives rise to the protonic defects that can be transported through the membrane.

With this basis and analogy established, this chapter will go through the fundamentals necessary to understand protonic transport in porous oxides. Central topics are the structure of water layer on surfaces in porous oxides, the properties giving rise to protonic species and conduction, and how the protons are transported through the material. This part will not cover all the general theory necessary to understand protonic conduction in porous oxides, but focus on important aspects and theories rarely considered in the study of ceramics. A literature review is included, and YSZ is chosen as the primary example material: the oxide is well known and thoroughly studied as a pure oxide ion conductor at high temperatures, much of the research on protonic conduction in porous oxides are done on YSZ, and it is used for most of the experiments in this thesis.

2.1 Water in porous materials

The amount of water adsorbed on the oxides' surface is determined by the thermodynamic equilibrium between the adsorbed water and the water vapour pressure in the gas phase. Adsorption of gases are well described by Langmuir- and BET-theories [29, 30], and with the addition of capillary condensation, the amount of water can be determined as a function of temperature and partial pressure of water. However, before I derive the procedure for quantifying water in the sample, I will describe the water layer structure on the surfaces of oxides.

2.1.1 Water structure on oxides

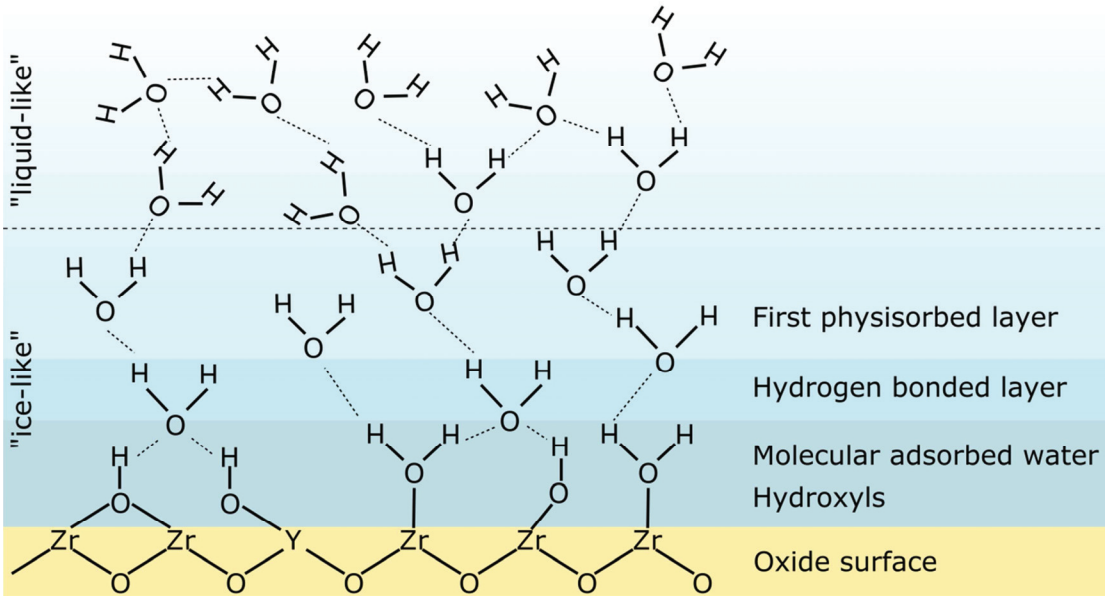

Fig. 2.1. Qualitative sketch of the water layer struture on a YSZ surface.

Fig. 2.1 shows qualitatively how the water structure on surfaces of oxides is build up [19, 31-33]. The two inner layers comprise the chemisorbed layer, and the additional adsorbed water forms the physisorbed water layer. The first chemisorbed layer consists of terminal- and multi-coordinated hydroxyls which are stable up to 800-1000 °C [19] and molecular adsorbed water [33]. The next layer is a hydrogen bonded water layer, where the water molecules have double hydrogen bonds to the hydroxyls. The hydrogen bonded water layer is complete and thermally stable up to around 200 °C under wet conditions (p_{H_2O} = 0.025 atm) [19, 34]. It is not clear from literature whether the hydrogen bonded layer is a chemisorbed or physisorbed water layer [21, 35], but it should be relatively clear that water molecules that are stable at temperatures above 200 °C [19] must be bonded much stronger to the surface than the average hydrogen bond strength in water – a bond strength typically referred to as physisorption.

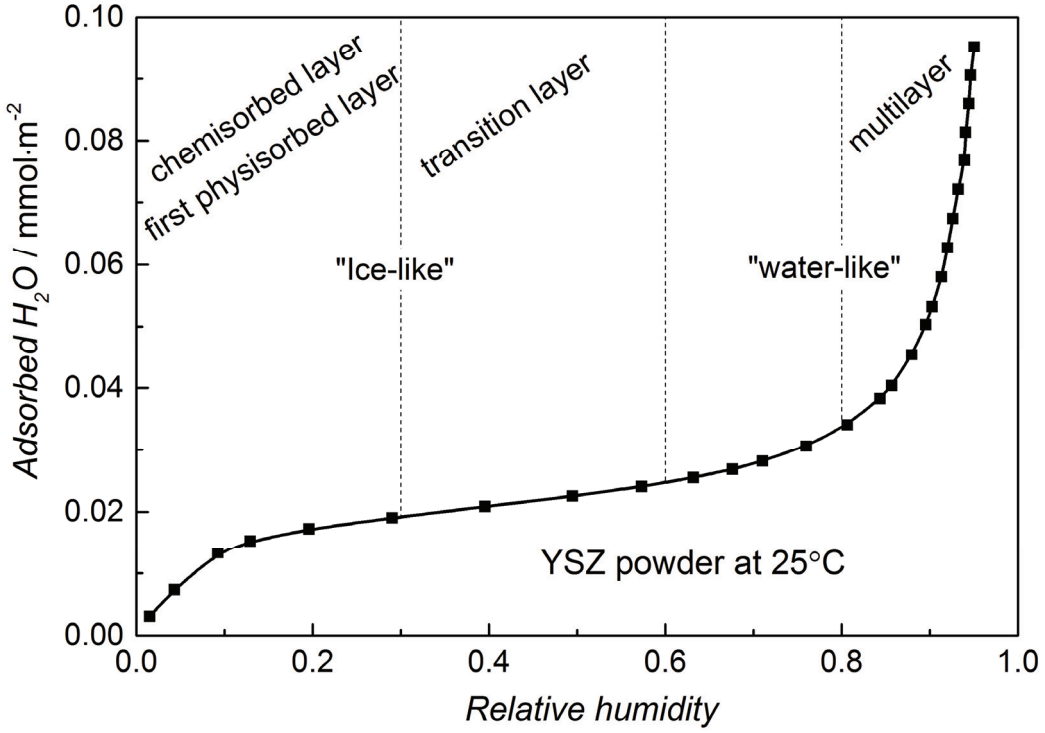

Fig. 2.2. Water adsorption profile of 8 mol% YSZ (TOSOH Corporation, Japan) as a function of relative humidity (RH) at 25 °C. The different indicated regions are based on measurements on SiO_2 [31].

The amount of physisorbed water adsorbed to the surface is determined by the relative humidity. Fig. 2.2 shows water adsorption measurement on 8 mol% doped Y-stabilised zirconia (8YSZ, TOSOH Corporation, Japan) as a function of relative humidity at 25 °C. From measurements on SiO_2 (generally transferable to YSZ and Fig. 2.2) it is shown that the three first layers (the two chemisorbed and the first physisorbed) are adsorbed on the surface at 0.3 RH [31]. Together these three layers have an atomic structure similar to ice. From 0.3 RH to 0.6 RH, the second physisorbed layer adsorbs and comprises a transitional structure between "ice-like" and "water-like" structure. At RH above 0.6, the structure of the layers is more similar to free water and multilayers form. Others have argued that multilayers only form above 0.8 RH [36], and the adsorption data for YSZ certainly seem to agree. Most important is however, the change from a fixed "ice-like" structure to "water-like" which seems to happen at 0.6 RH [31].

2.1.2 Concentration of water in chemisorbed water layer

Surface proton conduction in porous oxides is reported to be significant at temperatures as high as 450 °C [18]. At this temperature under wet conditions (p_{H_2O}=0.025 atm), the surface will be covered with hydroxyls and molecular bonded water, and the hydrogen bonded layer is partly filled [19]. In order to later be able to derive the conduction in the chemisorbed

water layer from 450 °C to RT, it is essential to derive an expression relating the coverage in the hydrogen bonded water layer to temperature and partial pressure of water. The equilibrium concentration of water in the hydrogen bonded layer can be expressed by the Langmuir equation [29]:

$$\frac{\theta_{ch}}{1-\theta_{ch}} = p_{H_2O} K_0^{ch} \exp\left(-\frac{Q_{ch}}{RT}\right) \tag{2.1}$$

where θ_{ch} is the relative coverage, p_{H_2O} is the water vapour pressure, K_0^{ch} is the equilibrium constant, R is the gas constant and Q_{ch} is the enthalpy of chemisorption of water.

The Langmuir relation is also suggested to be valid when describing the coverage of the hydroxyl layer [29], but seems irrelevant for the further analyses of porous oxides since the proton conductivity in the hydroxyl layer is negligible compared to the bulk and grain boundary conductivity at temperatures where only the hydroxyl layer is filled. (>500 °C).

Eq. 2.1 can be rearranged to show the coverage in the water layer as a function of temperature and p_{H_2O}:

$$\theta_{ch}\left(T, p_{H_2O}\right) = \frac{1}{1 + p_{H_2O}^{-1} K_0^{ch\text{-}1} \exp\left(\frac{Q_{ch}}{RT}\right)} \tag{2.2}$$

The volume water in the chemisorbed water layer can be calculated by determining the specific surface area. For 8YSZ, this is found by calorimetric adsorption measurements to be 6 H_2O per nm^2 and to vary with the yttrium content [37].

Fig. 2.3 shows the relative coverage θ_{ch} as function of temperature using the measured value of -74 kJ/mol for chemisorption of water (Q_{ch}) on 8YSZ [37], an equilibrium constant K_0^{ch} $=3.8\times10^4$ atm^{-1} at a partial pressure of water of 0.025 atm which fulfils the requirement that the layer is completely filled around 200 °C and empty around 600 °C [19].

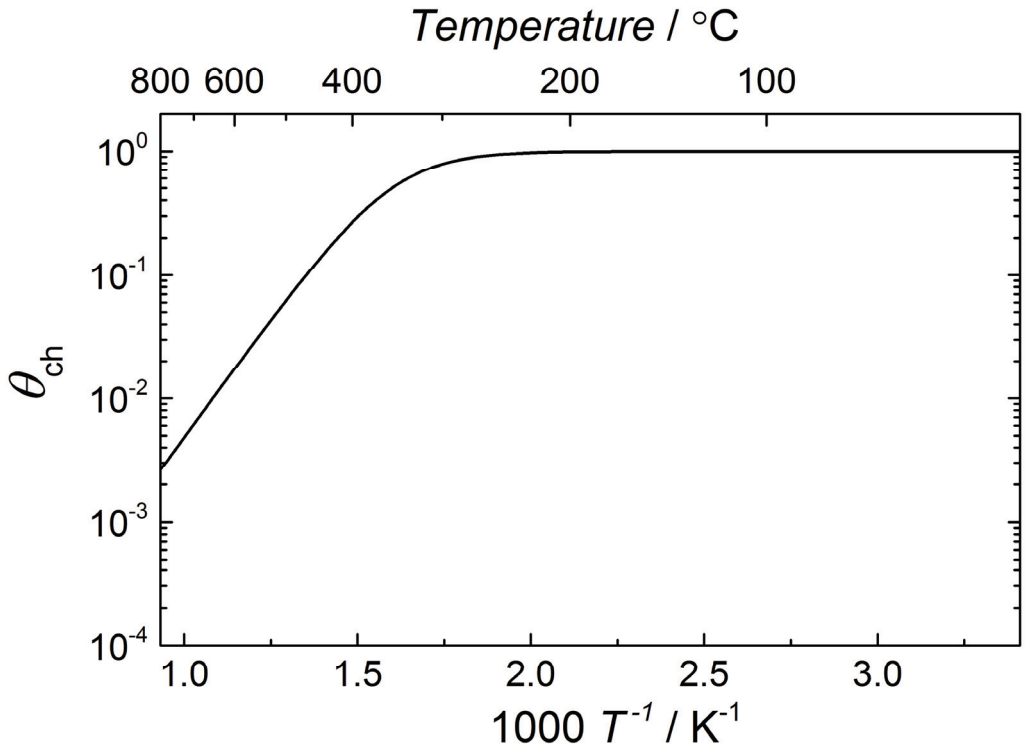

Fig. 2.3. Coverage of the oxide surface by hydrogen bonded water as function of inverse temperature for Q_{ch} = -74 kJ/mol [37], K_0^{ch} = 3.8×10^4 atm^{-1} and p_{H_2O} =0.025 atm.

2.1.3 Concentration of water in physisorbed water layer

Proton conduction in the physisorbed water layer is reported to be significant at temperatures below 150 °C [18] and is observed at even higher temperatures [20]. Physisorption of water is driven by the negative enthalpy of condensation. The amount of water in the samples is mathematically described by the BET isotherm [30]:

$$\frac{v}{v_m} = \frac{c\left(\frac{p}{p_0}\right)}{\left(1-\left(\frac{p}{p_0}\right)\right)\left(1+(c-1)\left(\frac{p}{p_0}\right)\right)} \tag{2.3}$$

where v is the volume water and v_m the monolayer volume, such that v/v_m gives the coverage on the surface in number of water layers. (p/p_0) is the RH and c is the BET constant which is defined as:

$$c \cong \exp\left(\frac{E_1 - E_L}{RT}\right) \tag{2.4}$$

where E_1 is the heat of adsorption for the first layer and E_L for the second and higher layers. E_L is usually more or less equal to the heat of condensation [38]. Here, when the chemisorbed layer is separately treated, the energy difference between the first and second physisorbed water layer is expected to be small, but still non-zero.

The equilibrium pressure p_0 is a strong function of temperature, dominated by the standard enthalpy of condensation of water, having a value of -44.0 kJ/mol at 25 °C. Since the enthalpy is strongly temperature dependent, the work in this thesis will use the Arden Buck equation to provide a more accurate approximation of the equilibrium water vapour pressure [39]:

$$p_0(T) = 0.0060 \exp\left(\left(19.843 - \frac{T}{234.5}\right)\left(\frac{T - 273.15}{T - 16.01}\right)\right) \tag{2.5}$$

In Fig. 2.4 the BET and Arden Buck equations have been employed to calculate how the coverage of physisorbed water with different binding energies between the first and the rest of the layers (E_1-E_L) increases with temperature at p_{H_2O} = 0.025 atm. The values of E_1-E_L are arbitrarily chosen, but are known to be small. The amount of water increases by more than three orders of magnitude from the temperature where the chemisorbed layer is completely filled (200 °C) and down to RT. The first physisorbed monolayer is only completely covered around 33 – 40 °C, dependent on differences in the adsorption energies.

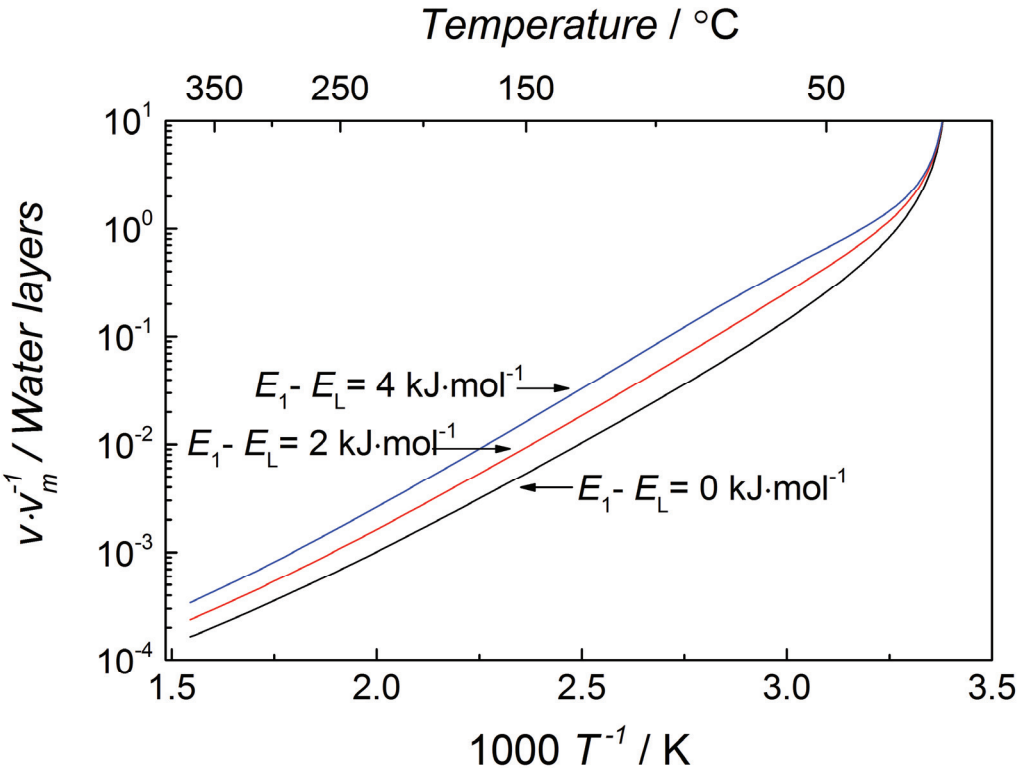

Fig. 2.4. Theoretical adsorption of water as function of temperature and difference in binding energies between the first and the rest of the adsorbed water layers at isobaric water conditions, p_{H_2O}=0.025atm, calculated on the bases of the BET and Arden Buck equations.

2.1.4 Capillary condensation

Due to capillary condensation, water condenses more easily in pores in the nanometer regime. Capillary condensation is a phenomenon where gas condensates to a liquid-like phase at a lower pressure than the equilibrium bulk pressure due to curvature of the surface. Whereas our fundamental studies will focus on samples without capillary condensation, it is important – for applications – to know when capillary condensation occurs because this phenomenon enables the membrane to keep the water inside at lower water vapour pressures and possibly also to keep a porous membrane gas tight. The further analysis will give insight into when we can expect pore condensation.

The Kelvin equation relates the spherical curvature radius r_w of the liquid phase with the surrounding vapour phase with a partial pressure p at temperature T [40]. For long, infinite, spherical channels with a defined contact angel φ of the solid, the Kelvin equation is:

$$r_w = \frac{2\gamma \bar{V} \cos\varphi}{RT \ln\left(\frac{p}{p_0}\right)} \qquad (2.6)$$

where p_0 is the equilibrium pressure over a flat water surface, $\overline{V}$ is the molar volume of water, which may be taken as $1.88 \cdot 10^{-5}$ m^3. The surface tension of water γ is 72.8 $mN \cdot m^{-1}$ at 25°C and decreases approximately linearly to 0 at the critical point of 374°C.

For 5YSZ, with a given contact angle φ of 72° [41], capillary condensation takes place in pores with a radius of 2 nm at p_{H_2O} = 0.03 atm at 25 °C. Fig. 2.5 shows the pore diameter as a function of temperature when capillary condensation occurs.

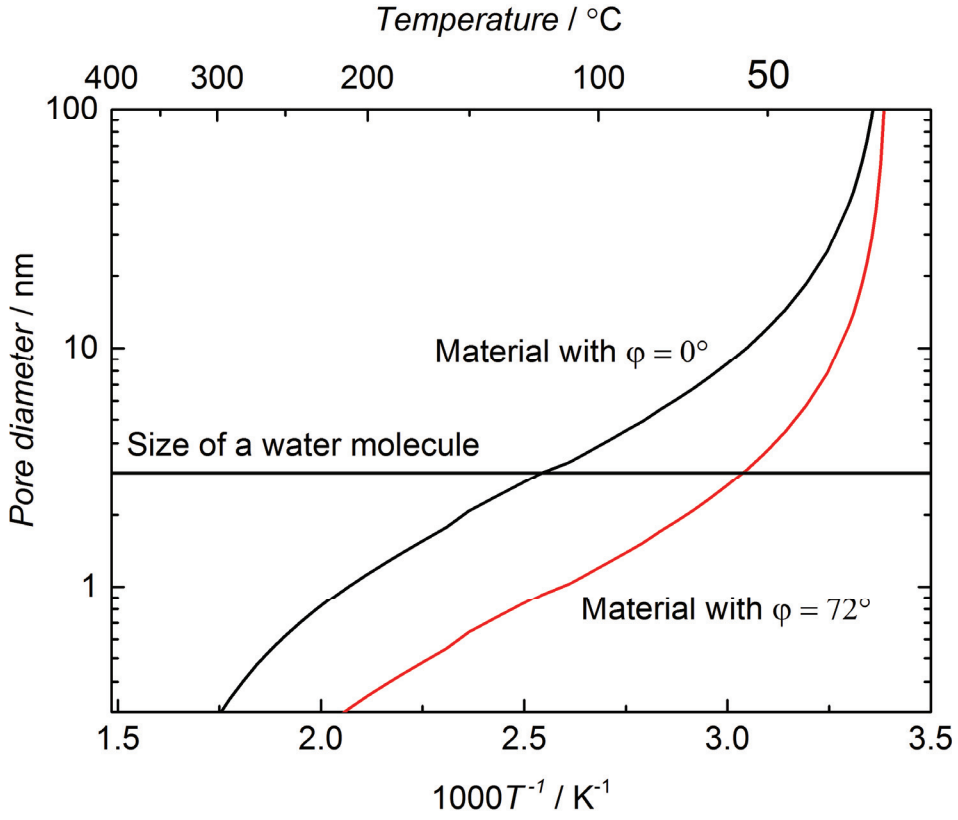

Fig. 2.5. Limiting pore diameter required for capillary condensation as a function of temperature for two different contact angles at p_{H_2O} = 0.025atm.

By multilayer adsorption, the effective radius of the pore channels reduces, and capillary condensation will take place in even larger pores. The Kelvin equation may be rewritten as:

$$r_w - t_c = \frac{2\gamma \overline{V} \cos\varphi}{RT \ln\left(\frac{p}{p_0}\right)} \qquad (2.7)$$

where t_c describes the critical thickness of the water layer prior to condensation [38].

In principle the amount of condensed water can be calculated, given a pore size distribution as Shimizu *et al*. have shown earlier [42]. The work in this thesis is focused on sample without capillary condensation, and further analysis is considered to be beyond the scope of this work.

2.2 Acid–base properties of surface and charge carrier concentration

The theory reviewed thus far expresses the amount of water on the surface as function of temperature and partial pressure of water. In this section, the focus will be on strategies to derive the concentration of charge carriers in the chemisorbed and physisorbed water layer as function of temperature and partial pressure of water. There is still uncertainty regarding the type of charge carrier, whether it is protons (H^+ or "proton holes"), hydroxide ions (OH^-), hydroxonium ions (H_3O^+), or even more hydrated protons ($H^+(H_2O)_m$). The charge carrier is however, as we will see, dependent on the acid–base properties of the surface and the concentration of water. General concepts about the acid–base properties of the surfaces will be reviewed before we focus on the detailed mechanisms and quantification of the charge carriers in the chemisorbed and physisorbed water layers.

The acidity of surfaces differs from the acidity of liquids. The term "acidic strength" of a solution may either refer to stronger acid or increased concentration. When considering the acidity of surfaces, it is however, important to distinguish between the number of acidic sites (concentration) and the strength of the acidic sites: two surfaces may have the same number of acidic sites, but the dominating acid-base sites show different ability to disproportionate, thereof different acidic strength [43]. Acidic sites are divided into both Brønsted-acidic and Lewis-acidic sites. Brønsted-acidic sites are able to donate a proton and hence give rise to proton conduction [19]. Lewis-acidic sites accept pairs of electrons, *e.g.* cations, and OH^- is a suitable example of a Lewis-base that can donate electrons to a Lewis acidic site.

2.2.1 Charge carrier concentration in the chemisorbed water layer

The protonic charges in the chemisorbed water layer result from acid-base reactions between the adsorbed water and the oxide surface. Anderson and Parks studied the conductivity in the chemisorbed water of porous silica in the early 60's and suggested the proton conduction to originate from the self-protonation of the surface [44]. Rewritten for the ZrO_2 system it reads:

$$\equiv \mathrm{ZrOH} + \equiv \mathrm{ZrOH} \Leftrightarrow \equiv \mathrm{ZrO^-} + \equiv \mathrm{ZrOH_2^+} \qquad (2.8)$$

where $\equiv \mathrm{Zr}$ denotes the surfaces bonded zirconia atoms. However, the acid–base reactions on the surface of ZrO_2 in presence of water were recently investigated by *ab initio molecular dynamics* (AIMD) by Sato *et al.* who showed that it is dissociation of molecularly adsorbed water on the cations on the surface that is giving rise to protonic charge carriers in the water layer [33]. They argued that acidity and basicity of $\equiv \mathrm{ZrOH_2^+}$ and $\equiv \mathrm{ZrO^-}$, respectively, is too strong to occur. By AIMD simulations they showed that $\equiv \mathrm{ZrOH_2}$ and $\equiv \mathrm{ZrOH^-}$ sites are the

dominating acid and basic Brønsted sites, giving rise to proton conduction either by direct jumping from ≡Zr-OH_2 to ≡Zr-OH^- or by Grotthuss transport in the hydrogen bonded water layer.

In the further derivations of the charge carrier concentration, the first water layer consisting of hydroxyls and molecularly bonded water is assumed to be filled, which is valid below approximately 450 ºC at p_{H_2O} = 0.025 atm [19]. The proportion between molecular and dissociative adsorption on the surface is further given by the equilibrium between deprotonation and protonation of $\equiv ZrOH_2$ sites and oxygen surface atoms >O (double bonded to surface), such that the dominating acid-base reaction on the surface of ZrO_2 can be written:

$$\equiv ZrOH_2 + > O \Leftrightarrow \equiv ZrOH^- + > OH^+ \tag{2-9}$$

The equilibrium constant ($K_{D,ch}$) for the acid-base reaction can be expressed in terms of the activities of each participating species, and further as their concentrations divided by the standard concentration:

$$K_{D,ch} = \frac{a_{\equiv ZrOH^-} \cdot a_{>OH^+}}{a_{\equiv ZrOH_2} \cdot a_{>O}} = \frac{\frac{[\equiv ZrOH^-]}{[\equiv ZrOH_2]^0} \cdot \frac{[> OH^+]}{[> O]^0}}{\frac{[\equiv ZrOH_2]}{[\equiv ZrOH_2]^0} \cdot \frac{[> O]}{[> O]^0}} = \frac{[\equiv ZrOH^-] \cdot [> OH^+]}{[\equiv ZrOH_2] \cdot [> O]} \tag{2.10}$$

Here, the concentrations are expressed as mol per surface area, and it may be noted that the same standard concentration is used for both types of adsorbed species, given by the Zr surface sites. In the presence of solely chemisorbed water, it is reasonable to assume, as done by Sato *et al.* [45], that the electroneutrality must hold for the surface layer itself (no electrical double layer forms) which is [≡$ZrOH^-$] = [>OH^+]. Moreover, the protons are considered to be mobile as "protons holes", diffusing from ≡Zr-OH_2 to ≡Zr-OH^- (via direct jump or via Grotthuss transport), such that the charge carrier concentration of proton holes is:

$$[\equiv ZrOH^-] = \sqrt{[\equiv ZrOH_2][> O] K_{D,ch}} = \sqrt{[\equiv ZrOH_2][> O]} \cdot \exp\left(\frac{\Delta S^0_{D,ch}}{2R}\right) \exp\left(\frac{-\Delta H^0_{D,ch}}{2RT}\right) \tag{2.11}$$

where $\Delta S^0_{D,ch}$ and $\Delta H^0_{D,ch}$ are the entropy change and the enthalpy change for the defect formation (Eq. 2.9). As seen from Eq. 2.11, the charge carrier concentration in the chemisorbed water layer is independent on the concentration of water when the first water layer is filled. Moreover, assuming a dilute system where the concentrations of $ZrOH^-$-defects

and >OH^+-defects remain small compared to the $ZrOH_2$-sites and >O-sites, [$ZrOH_2$] and [>O] can be replaced by [$ZrOH_2$]^0 and [>O]^0, respectively, such that Eq. 2.11 becomes:

$$[\equiv \mathrm{ZrOH}^-(T)] = \sqrt{[\equiv \mathrm{ZrOH_2}][>\mathrm{O}]K_{\mathrm{D,ch}}} = \sqrt{[\equiv \mathrm{ZrOH_2}]^0[>\mathrm{O}]^0} \cdot \exp\left(\frac{\Delta S^0_{\mathrm{D,ch}}}{2R}\right)\exp\left(\frac{-\Delta H^0_{\mathrm{D,ch}}}{2RT}\right) \quad (2.12)$$

2.2.2 Charge carrier concentration in the physisorbed water layer

The protonic charge carriers in the physisorbed water layer result from dissociation of the adsorbed surface water governed by the acid-base properties of the surface. Anderson and Parks suggested two possible reactions for the silica system, namely auto proteolysis of water and an acid-base reaction between the oxide and water [44], here rewritten for zirconia:

$$2\mathrm{H_2O\,(ads)} \Leftrightarrow \mathrm{H_3O^+\,(ads)} + \mathrm{OH^-\,(ads)} \quad (2.13)$$

$$\equiv \mathrm{ZrOH} + \mathrm{H_2O\,(ads)} \Leftrightarrow \equiv \mathrm{ZrO^-} + \mathrm{H_3O^+(ads)} \quad (2.14)$$

The equilibrium constant of the reaction between the oxide and the water pK_a (Eq. 2.14) is orders of magnitude higher than the auto proteolysis of water pK_w (Eq. 2.13) [11, 21, 44]. Moreover, an electrical double layer will be formed as a result of the dissociation of the adsorbed surface water. The carrier concentration in the adsorbed water (in the double layer) will be dominated by the acid-base properties of the surface. For acidic surfaces, it is reasonable to assume a negatively charged surface compensated by hydroxonium ions in the water layer, and for basic oxides a positively charged surface compensated by hydroxide ions in the water layer. Detailed derivation of the electrical double layer on oxides' surfaces will be treated in Chapter 3.3.

According to the finding of Sato *et al.* [33], it is reasonable to assume the acidity of water layer on ZrO_2 surfaces to be dominated by dissociation of ≡$ZrOH_2$, with the following equilibrium reaction:

$$\equiv \mathrm{ZrOH_2} + \mathrm{H_2O\,(ads)} \Leftrightarrow \equiv \mathrm{ZrOH^-} + \mathrm{H_3O^+(ads)} \quad (2.15)$$

The equilibrium constant ($K_{\mathrm{D,ph}}$) for the acid-base reaction in presence of physisorbed water can be expressed in terms of the activities of each participating species, and further as their concentrations divided by the standard concentration:

$$K_{\mathrm{D,ch}} = \frac{a_{\equiv \mathrm{ZrOH}^-} \cdot a_{\mathrm{H_3O^+}}}{a_{\equiv \mathrm{ZrOH_2}} \cdot a_{\mathrm{H_2O}}} = \frac{\frac{[\equiv \mathrm{ZrOH}^-]}{[\equiv \mathrm{ZrOH_2}]^0} \cdot \frac{[\mathrm{H_3O^+}]}{[\mathrm{H_2O}]^0}}{\frac{[\equiv \mathrm{ZrOH_2}]}{[\equiv \mathrm{ZrOH_2}]^0} \cdot \frac{[\mathrm{H_2O}]}{[\mathrm{H_2O}]^0}} = \frac{[\equiv \mathrm{ZrOH}^-] \cdot [\mathrm{H_3O^+}]}{[\equiv \mathrm{ZrOH_2}] \cdot [\mathrm{H_2O}]} \tag{2.16}$$

Here, the concentrations are expressed as mol per surface area, and it may be noted that the same standard concentration is used for both types of adsorbed species, given by the Zr surface sites. The protons are considered to be the mobile charged species in the water layer [46], such that the conduction is dominated by the protonic charge carrier. Moreover, the electro neutrality condition $[\mathrm{ZrOH}^-] = [\mathrm{H_3O^+}]$ has to be satisfied and the charge carrier concentration can be expressed in terms of mol per surface area:

$$[\mathrm{H_3O^+}] = \sqrt{[\equiv \mathrm{ZrOH_2}][\mathrm{H_2O}]K_{\mathrm{D,ph}}} = \sqrt{[\equiv \mathrm{ZrOH_2}][\mathrm{H_2O}]} \cdot \exp\left(\frac{\Delta S^0_{\mathrm{D,ph}}}{2R}\right) \exp\left(\frac{-\Delta H^0_{\mathrm{D,ph}}}{2RT}\right) \tag{2.17}$$

where $\Delta S^0_{\mathrm{D,ph}}$ and $\Delta H^0_{\mathrm{D,ph}}$ are the entropy and the enthalpy for the defect formation (Eq. 2.15). Assuming a dilute system, where the concentration of protons and ZrOH^--defects remain small compared to the $\mathrm{ZrOH_2}$-sites, $[\mathrm{ZrOH_2}]$ can be replaced $[\mathrm{ZrOH_2}]^0$. The concentration of water can further be expressed by the multilayer BET-equation (Eq. 2.3), such that Eq. 2.17 becomes:

$$[\mathrm{H_3O^+}(p,T)] = \sqrt{\frac{c\left(\frac{p}{p_0}\right)v_m}{\left(1-\left(\frac{p}{p_0}\right)\right)\left(1+(c-1)\left(\frac{p}{p_0}\right)\right)}} \sqrt{[\equiv \mathrm{ZrOH_2}]^0} \cdot \exp\left(\frac{\Delta S^0_{\mathrm{D,ph}}}{2R}\right) \exp\left(\frac{-\Delta H^0_{\mathrm{D,ph}}}{2RT}\right) \tag{2.18}$$

Here v_m expresses the "volume" of a monolayer defined in terms of mol per surface area. The enthalpy of the dissociation reaction is considered to be endothermic, such that the concentration of protonic charges increases with increasing temperature. Furthermore, $\Delta H^0_{\mathrm{D,ph}}$ reflects the strength of the dissociation reaction and are considered to be endotherm.

In general, the acidity of oxides increases with increasing oxidation number of the cation and decreasing ionic radius. $\mathrm{MO_2}$ oxides, as studied in this work, are typically slightly acidic [47]. Interestingly, uniform doping of both $\mathrm{TiO_2}$ and $\mathrm{SiO_2}$ with both higher and lower valence cations are reported to increase the acidity of the surfaces [48]. This is most probably a result of that some of the surface sites increase their acidity such that the overall dissociation in the

water layer increases. However, from conductivity measurements of nanocrystalline, porous samples of gadolinium-doped ceria (GDC, 0.5, 10 and 20 mol%) there is on the contrary concluded that the proton conductivity is independent on the bulk defect chemistry of the oxide [16]. The surface area, particle size and porosity of the samples have never been reported in that particular study, so the results may not be general. Moreover, it should also be mentioned that surfaces often have other compositions than the bulk. This can further lead to space charge potentials and charge depletion close to the surfaces that may influence the oxidation states and thereby the acidic properties. Space charge theory will be considered in the next chapter, and the acidic properties and protonic conduction of different doped samples of porous TiO_2 will be the topic in Manuscript IV.

2.3 Protonic conductivity in porous oxides

The conductivity of protonic and ionic species is a product of their charge, mobility and concentration, here exemplified with protons: $\sigma_{H^+} = e\mu_{H^+}c_{H+}$. The total conductivity in a sample, σ_{tot} is the sum of the partial conductivities. In the previous section I have derived in detail how the number of charge carriers in porous oxides can be calculated. In this part, I will review the existing theory about charge carrier mobility and transport mechanisms. The section will end with expressions for the total conductivity of porous oxide samples, shown with detailed expressions for the partial conductivity in the chemisorbed and physisorbed water layers.

2.3.1 Grotthuss mechanism and vehicle mechanism

As outlined in section 2.2, the surface acidic properties determine whether protons or proton holes (and possibly hydrated protons or hydroxide ions) are the majority charge carriers in the water layer in porous oxides. Under acidic properties, protons are in surplus and diffuse via structural diffusion (Grotthuss mechanism) or as hydrated ions (vehicle mechanism). With surplus of hydroxide ions in the water layer, the protonic charges diffuse via structural diffusion (proton holes) [49-51] or as hydroxides ions. In the Grotthuss mechanism, excess protons diffuse through the hydrogen network of water molecules and hydroxide ions on the surface; bonds are continuously broken and new ones are formed. Under basic conditions, the structural diffusion rather happens with transport of *proton holes* - such that protons are moving the opposite way, from a water molecule to a hydroxide ion in the water layer. When protons are transported as hydroxide ions, hydroxonium ions, or higher hydrated protons ($H^+(H_2O)_m$), the proton uses the water molecule as a "vehicle", thereof the mechanism's name. A schematic of the two different mechanisms exemplified with an acidic surface is presented in Fig. 2.6.

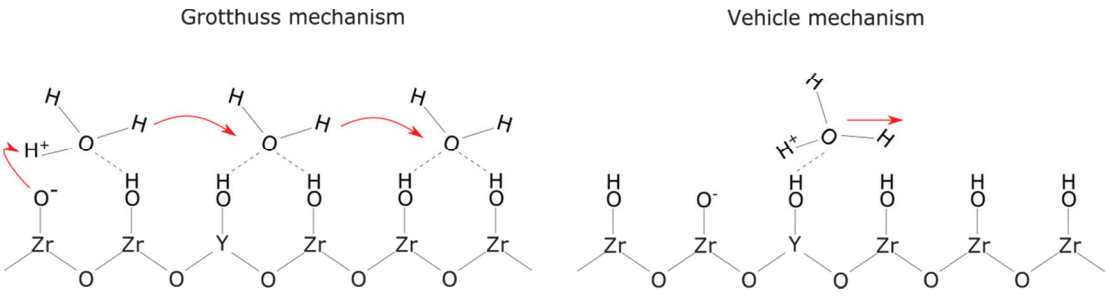

Fig. 2.6. Left: Grotthuss mechanism where an "excess" proton diffuses through the hydrogen bond network of water molecules. Hydrogen bonds are broken and new are made. Right: Protons are transported together with a water molecule functioning as a vehicle in the vehicle mechanism.

There seems to be some disagreements about the transport mechanism with just hydroxyls present on the surface. Protons are assumed to migrate via a hopping mechanism from hydroxide to hydroxide or oxide sites dependent on the degree of coverage [18, 19, 21, 44]. However, transport in the hydroxyl layer is rarely significant for the total conductivity, since volume conduction in most oxides are orders of magnitude higher than surface conduction at temperatures where only hydroxyls are present at the surface (500-600 °C) [19]. Because of the unmeasurable partial conductivity, it is difficult to verify the conduction mechanism, but it is reasonable to assume structural diffusion (Grotthuss transport) because of the similarities to bulk transport of protons in hydrated oxides.

For the hydrogen bonded layer, the transport mechanism has long ago been suggested to be vehicle-type at low coverage and Grotthuss like at higher degree of coverage [21, 44]. The recent results from Sato *et al.* indicate protons (as protons or "proton holes") to be the dominating charge carrier, migrating by the Grotthuss mechanism for acidic, neutral and basic surfaces [33]. Furthermore, a study performed by Miyoshi *et al.* showed an H/D-effect of around 2 in the temperature range between 150-250 °C on YSZ, under humidified conditions. In this temperature span, transport in the hydrogen bonded layer dominates, and a H/D-effect of around 2 can only be consistent with a Grotthuss type transport of protons [19]. It thus seems reasonable that the transport mechanism is Grotthuss type also in the hydrogen bonded layer.

The proton conducting mechanism in the physisorbed water layer is yet to be determined. It is suggested to be Grotthuss diffusion [18] and to change from Grotthuss to vehicular transport at more liquid-like conditions [19]. Thus it can substantiate that the transport mechanism in the physisorbed water layer is dependent on the water layer thickness and water structure. Kreuer *et al.* on the contrary argue that vehicular transport of protons is the only effective path because the polar environment from the host material induces a static solvent effect that prevents Grotthuss diffusion [11]. Apparently this is observed for the layered compound $H_3OUO_2AsO_4{\times}3H_2O$ [52].

As stated earlier, proton conduction in porous oxides has probably more in common with proton conduction in polymers than in dense ceramics. In proton conducting polymers and bulk water, both Grotthuss and the vehicle mechanisms are generally considered to be present [22, 53]. Moreover, Jac *et al.* have shown, by means of transport number measurements (see section 4.3), that the electro-osmotic drag coefficient of protons is approximately 2.5 water molecules in fully hydrated Nafion, thus showing vehicular transport of protons [54]. The nature of the conduction mechanism will be discussed in more detail in Manuscript III.

2.3.2 Mobility

Protonic species migrate in water layers by thermally activated diffusion. The ionic diffusivity and the ionic mobility are linked through the Nernst-Einstein relation:

$$D_{\mathrm{i}} = \mu_{\mathrm{i}} \frac{RT}{z_{\mathrm{i}} F} \tag{2.19}$$

where D_{i} and μ_{i} denote the random diffusion coefficient and the electrical mobility of charge carrier i. R is further the universal gas constant and F the Faraday constant.

The mobility of protonic species follows Arrhenius behaviour and can be expressed as:

$$\mu = \mu_0 \frac{1}{T} \exp\left(\frac{-\Delta H_{\mathrm{mob}}}{RT}\right) \tag{2.20}$$

where ΔH_{mob} and μ_0 are the enthalpy and pre exponential of the mobility of charged specie. The enthalpy can be considered as the energy required for the protonic species to migrate from one surface atom to the next, or to break a hydrogen bond in a Grotthuss chain. The pre-exponential term can further be expanded into:

$$\mu_0 = \Gamma_0 \alpha s^2 \frac{zF}{R} \exp\left(\frac{\Delta S_{\mathrm{mob}}}{R}\right) \tag{2.21}$$

where Γ_0 is the attempt frequency, α is a structure and system dependent parameter, s is the average jump distance and ΔS_{mob} is the activated entropy of mobility. The structure parameter is further dependent on the number of vacant neighbouring sites to jump to and concentration of defects.

The enthalpy of mobility of the protonic charge carrier in the water layer of porous oxides is yet to be determined. So far, only activation energies of the conductivity at fixed RH have been reported [10, 22, 27]. These values span from 6-37 kJ/mol, but the activation energy reflects both the enthalpies of mobility and defect formation of protons as we will see later. The wide spread activation energies are discussed in more detail in section 2.3.5

2.3.3 Conduction in the chemisorbed water layer

As pointed out in Section 2.1, it is not precisely defined in literature whether the chemisorbed layer is comprised of just the hydroxyl layer or also the hydrogen bonded layer. The following derivation of the conductivity will only be valid for the conduction in the hydrogen bonded layer when the hydroxyl layer is complete (below ~450 ºC, $p_{H_2O} = 0.0025\,\text{atm}$ [19]).

Eq. 2.12 describes the charge carrier concentration in the chemisorbed water layer, when the first layer is filled. As stated earlier, the protons can move either by direct jumps from ≡Zr-OH_2 to ≡Zr-OH^- or via Grotthuss transport in the hydrogen bonded water layer. These two paths show significant different transport properties, which affects the mobility term.

As derived in the previous section, the mobility term μ_0 is dependent on a structure parameter α (Eq. 2.21), which is further dependent on the number of defects and the vacant sites where the protons can move to. Thus the mobility term for the two types of movements must be described by two different functions. The direct jump from ≡Zr-OH_2 to ≡Zr-OH^- is dependent on the concentration of vacant ≡Zr-OH_2 sites where the "proton holes" can move to. The transport via the hydrogen bonded water layer is on the other side dependent on the concentration of available water molecules in the hydrogen bonded layer where a Grotthuss type transport can occur. This can be summarised into the following equations:

$$\mu_{OH} = \mu'_{0,OH}[ZrOH_2]\frac{1}{T}\exp\left(\frac{-\Delta H_{mob,OH}}{RT}\right) \tag{2.22}$$

$$\mu_{HB} = \mu'_{0,HB}[H_2O]\frac{1}{T}\exp\left(\frac{-\Delta H_{mob,HB}}{RT}\right) \tag{2.23}$$

where the first one gives the mobility within first layer (denoted OH) and the second via the hydrogen bonded layer (denoted HB). Here, $\mu'_{0,OH}$ and $\mu'_{0,HB}$ are modified versions of the pre exponential term given in Eq. 2.21, where the number of available sites the protons can move to are specified outside structure parameter. The proton mobility is further assumed to be much higher in the hydrogen bonded layer, based on the results in Ref. [33].Furthermore, the concentration of water in Eq 2.23 can be described by the Langmuir isotherm, as derived in Section 2.1.2 (Eq. 2.2). As we see from Eq 2.23, the mobility via the hydrogen bonded layer will be directly proportional to the coverage of water in the hydrogen bonded layer.

With both an expression for the charge carrier concentration and mobility, we are ready to derive the full expression of the conductivity in the chemisorbed water layer. To express the conductivity of a specific sample, the charge carrier concentration given in Eq. 2.12 must be multiplied by the specific surface area of the sample (S_{BET}) and the geometric density of the sample (ρ). The charge carrier concentration is thus expressed in terms of mol per volume. The expression for the conductivity in the chemisorbed water for a specific sample then reads:

$$\sigma_{\mathrm{ch}}(T,p_{\mathrm{H_2O}})=\frac{1}{\left(1+p_{\mathrm{H_2O}}^{-1}K_0^{\mathrm{ch\text{-}1}}\exp\left(\frac{Q_{\mathrm{ch}}}{RT}\right)\right)}\sqrt{[\equiv \mathrm{ZrOH_2}]^0[>\mathrm{O}]^0}\cdot$$
$$S_{\mathrm{BET}}\rho F\exp\left(\frac{\Delta S^0_{\mathrm{D,ch}}}{2R}\right)\frac{\mu'_{0,HB}}{T}\exp\left(-\frac{\frac{1}{2}\Delta H^0_{\mathrm{D,ch}}+\Delta H_{\mathrm{mob,HB}}}{RT}\right) \tag{2.24}$$

Here, F denotes the Faraday constant.

Fig. 2.7 shows the partial conductivity of a model oxide given in $\mathrm{Scm^{-1}}$ (a.u.) of bulk and grain boundaries, as well as the protonic conductivity in the chemisorbed water layer, as function of temperature under fixed partial pressure of water. At lower temperatures the total conductivity is dominated by surface transport. The surface related conductivity increases with increasing temperature and shows Arrhenius behaviour below 200 °C. The associated activation energy is related to the enthalpy of defect formation and mobility as defined in Eq. 2.18. At 200 °C the surface coverage starts decreasing with increasing temperature, yielding a maximum in the protonic surface conduction at around 350 °C.

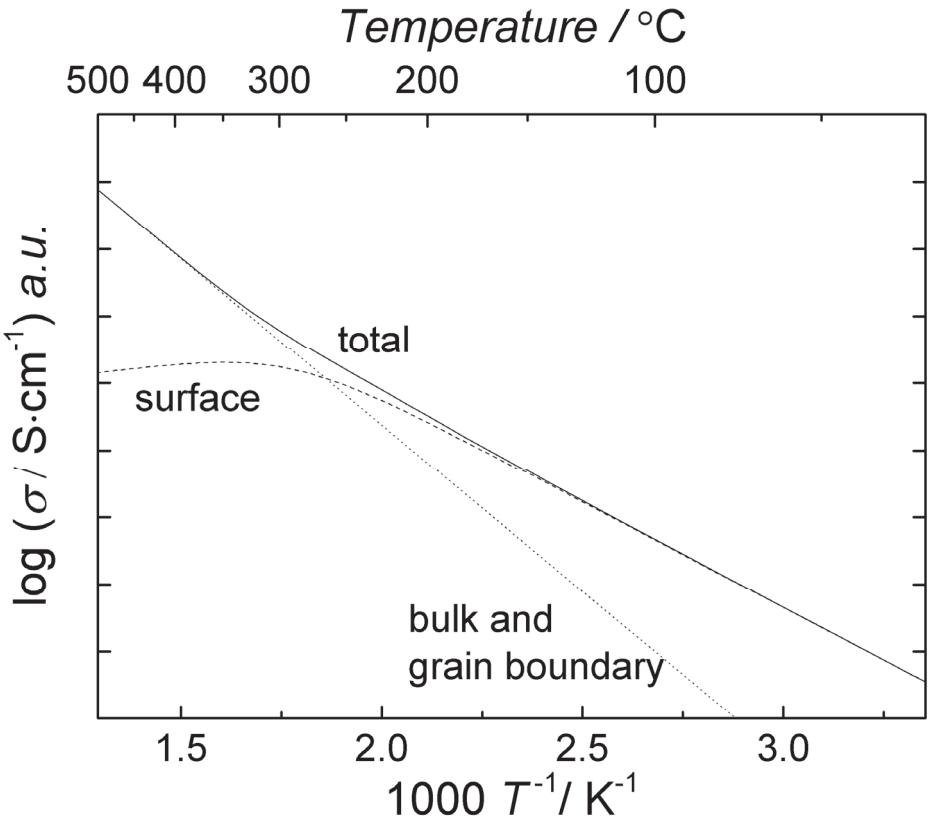

Fig. 2.7. Partial conductivity of bulk and grain boundary and in the chemisorbed surface layer as function of temperature under fixed $p_{\mathrm{H_2O}}$.

The conductivity in the chemisorbed water layer is to a small degree studied in literature and hereby follows the most important results. Recent measurements on different samples of porous YSZ undertaken by Scherrer *et al.* result in activation energies ranging from 39 to 106 kJ/mol for the total conductivities in the temperature regime 120 – 450 °C, reflecting a combination of both oxygen ions and proton conductivities [18]. Electrical conductivity measurements of 6YSZ carried out at a fixed frequency under wet conditions has yielded an activation energy of 29 kJ/mol [21]. Hinterberg *et al.* have by HNMR determined the activation energy of the chemically bond water of 9.5YSZ to be 63±19 kJ/mol and 63±13 kJ/mol on two different samples [55]. All in all, the reported activation energies vary considerably.

2.3.4 Conduction in the physisorbed water layer

Here I will derive the full expression for the protonic conductivity in the physisorbed water layer. The charge carrier concentration is given by Eq. 2.18 and the mobility is assumed to be temperature dependent and independent on the concentration of water, thus Eq. 2.20 can be used as is. At this point of the derivation, the charge carrier mechanism is considered to be the same at all temperatures and water layer thicknesses. Moreover, all enthalpies and pre-exponentials are generally considered to be specific for the physisorbed water layer, independent on the water layer thickness. Similar to the conductivity in the chemisorbed water layer, the charge carrier concentration is multiplied by the specific surface area of the sample (S_{BET}) and the geometric density of the sample (ρ) to express it in terms of mol per volume for a specific sample. The protonic conductivity in the physisorbed water, expressed in terms of the sample specific conductivity is thus written as:

$$\sigma_{\mathrm{ph}}(T,p) = \sqrt{\frac{c\left(\frac{p}{p_0}\right)v_m}{\left(1-\left(\frac{p}{p_0}\right)\right)\left(1+(c-1)\left(\frac{p}{p_0}\right)\right)}}\sqrt{[\equiv \mathrm{ZrOH_2}]^0 S_{\mathrm{BET}}\rho}\cdot F\frac{\mu_{0,\mathrm{ph}}}{T}\exp\left(\frac{\Delta S^0_{\mathrm{D,ph}}}{2R}\right)\exp\left(-\frac{\frac{1}{2}\Delta H^0_{\mathrm{D,ph}}+\Delta H_{\mathrm{mob,ph}}}{RT}\right) \tag{2.25}$$

where F denotes the Faraday constant.

It should be noted that an area factor taking values between 2/3 and 1 dependent on the pore structure can be added for both conduction in the chemisorbed and physisorbed water layer. It is 2/3 for perfect cubic grains and 1 for percolating straight channels, as the water parallel to the electrodes does not give contribution to the measured conductivity. Since this factor does not appreciable change the conductivity and is hard to determine accurately, it is omitted from the expressions.

Fig. 2.8 summarizes the partial and the total conductivities in a porous oxide sample as a function of temperature at a fixed partial pressure of water. (Note that the equilibrium pressure of water is strongly dependent on the temperature, as derived in section 2.1.2). The bulk and grain boundary conductivities dominate at high temperatures and obey an Arrhenius behaviour. In the intermediate temperature range, the proton conductivity in the chemisorbed layer dominates. At low temperatures, the total conductivity increases with decreasing temperature as a result of increasing amount of water and protons in the sample. The slope of the physisorbed conductivity is given by the sum of the enthalpies of condensation of water, mobility, and defect formation, with the exception at the lowest temperatures (below ~40 ºC) where multilayer adsorption occurs.

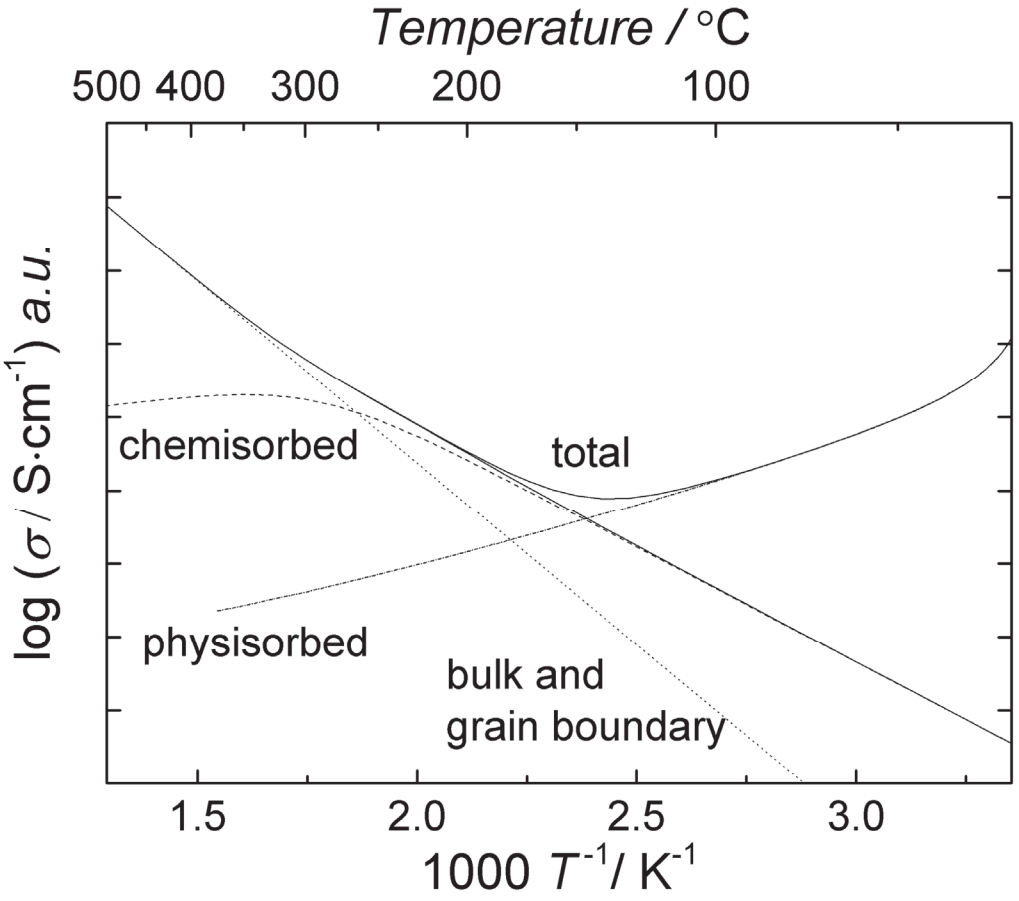

Fig. 2.8. Partial and total conductivity as function of temperature under fixed p_{H_2O}.

Eq. 2.25 can be evaluated in two other ways. First of all, by keeping the temperature *T* fixed and by evaluating the equation as a function of the partial pressure of water *p*. The equilibrium pressure of water $(p_0(T))$, mobility, and dissociation will in this case be constant.

The only variable term in Eq. 2.25 will be the BET-expression. The conductivity as a function of partial pressure of water is thus expected to take a similar form as an adsorption isotherm.

Secondly, by keeping the relative humidity (p/p_0) fixed, Eq. 2.25 is evaluated as a function of temperature. The concentration of water is then constant as function of temperature, in contrast to the simulation in Fig. 2.8 where p_{H_2O} are kept fixed. The surface conductivity follows Arrhenius behaviour in a plot of the logarithm of the conductivity vs inverse temperature (log σ vs $1/T$). In such a plot the slope will be given by the sum of the enthalpies of defect formation and mobility $(1/2\Delta H^0_{D,ph} + \Delta H_{mob,ph})$. This behaviour is observed in Refs. [10, 22, 27], where the results have been presented in red in Fig. 1.3 in the introduction.

From Eqs. 2.24 and 2.25, we also see that the conductivity scales with the surface area (S_{BET}) of the sample. Increasing the specific surface area will therefore increase the proton conductivity. Comparing different samples and obtaining the material specific conductivity should therefore be done by correcting for the specific surface area. If the pore size of the sample is in the range where capillary condensation occurs, a term of the related increased amount of water in Eq. 2.25 must be included. This was briefly discussed earlier, see Section 2.1.3.

2.3.5 Concentration effect of charge carrier concentration and mobility

It is pointed out in several studies that the conductivity in the physisorbed region increases much faster with decreasing temperature than what is predicted from the enthalpy of condensation [14, 18, 20]. According to Eq. 2.25, the slope is a result of the enthalpies of condensation, dissociation, and mobility. Specifically, the conductivity shows a square root dependency with the concentration of water. Thus the numerical value of the observed slope at low temperatures in graphs like Fig. 2.8 should be significantly *less* than the enthalpy of condensation ($slope > \Delta H_{cond}$ = -44 kJ·mol^{-1}). Since the exact opposite is observed, there must be some other cause.

In studies of zeolites, Kreuer *et al.* argue for a strong thickness-dependent enthalpy and entropy of dissociation and a slight thickness-dependent enthalpy of mobility. This is due to a decreasing binding energy between the wall and the water molecules, and a changing water structure with increasing distance from the surface [28]. Temperature dependent activation energies of the conductivities - determined under fixed RH - are shown by others to decrease with increasing water layer thickness [10, 22, 27, 28], observations which thus are consistent with the claim of Kreuer *et al.* Furthermore, thickness dependent enthalpy and entropies of dissociation and enthalpy of mobility will thus in a *log* σ vs $1/T$ plot (similar to Fig. 2.8) be observed as a change of the slope. This can therefore explain why such high increases in the conductivities with decreasing temperature are observed. The enthalpies and entropy decrease gradually with temperature due to a change in the water layer thickness.

However, we should keep in mind that the conductivity mechanism (Grotthuss or vehicle type) are yet to be determined, which also can give rise to changes in the enthalpy and pre-exponential of the mobility. We will also see that the surface conduction consists of two series connected transport processes that affect the interpretation of the conductivity data. I therefore refer to the forthcoming manuscripts for further discussion.

3 Interfaces and aspects relevant for transport in porous ceramics

The theory reviewed in Chapter 2 described the basics of protonic conduction in porous oxides. For more complicated systems and materials, the properties of the oxides' surfaces and interfaces have to be taken into consideration. Already, we have seen that the acidic properties at the surface of the oxides determine the number of charge carriers. As we will see later in the manuscripts, the interfaces of the oxide influence the overall transport of charged ions, in the oxides as well as in the liquid water layer. Therefore, this part focuses on the theoretical bases for surfaces, interfaces and the interactions important for protonic conduction in porous oxides.

3.1 Interfaces and origin of charged surface

An interface can be defined as the surface forming a common boundary, either as solid-liquid and solid-gas or internally in solid material as *e.g.* grain boundaries and phase boundaries. There is a wide range of different interfaces for solids and liquids. Fig. 3.1 summarizes the most important interfaces for determining the transport properties of porous oxides under wet conditions. The solid-solid interface is of significance for the transport through the solid phase, the solid-liquid interface which affects the protonic transport in the liquid phase, and the solid-gas interface which determines the thickness of the water layer. The solid-gas interface is treated under gas adsorption in Chapter 2.1, as well as the important aspect on the interface between the water layer and the humidified air. The latter is of importance for capillary condensation of water, where the surface tension between the liquid-gas and the interfaces gives rise to this phenomenon.

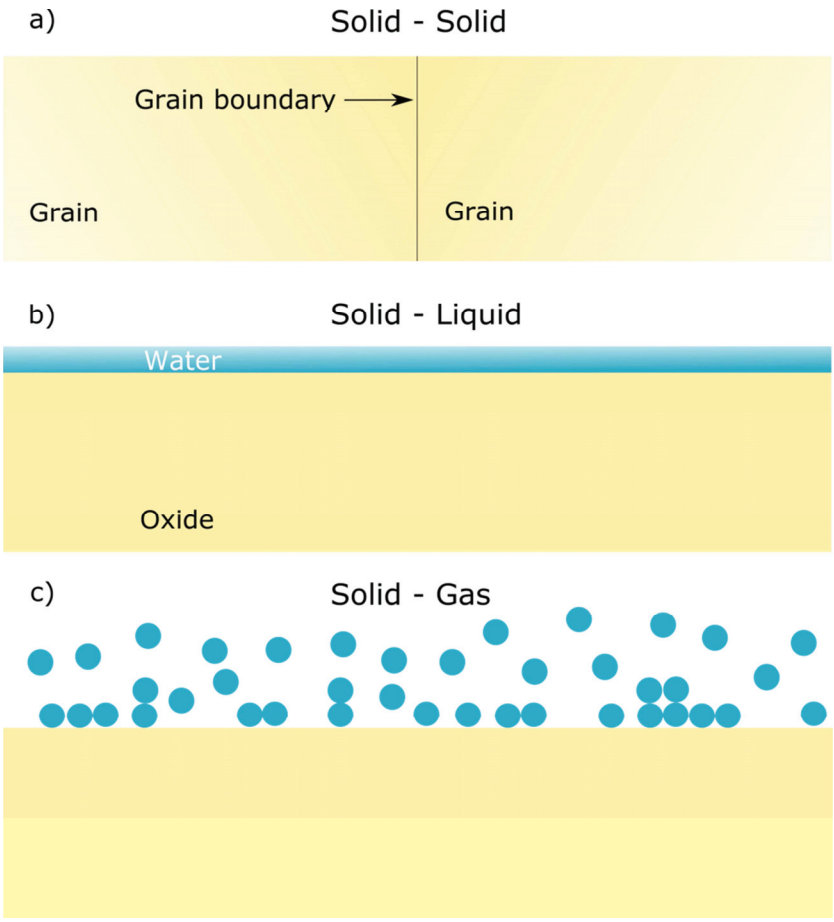

Fig. 3.1 Sketches of relevant interfaces between the solid porous oxides treated in this thesis. a) solid-solid, b) solid-liquid, and c) solid-gas.

Interfaces are caused by mismatch of chemical bonds. The break of symmetry leads to higher potential energy at the interface, where a rearrangement of the surface occurs in order to lower the free energy of the surface. We have already seen that the structure of water on the solid-liquid surface differs from the bulk structure in that the water layers close to the surface are less randomised and has a more ice-like structure. The rearrangement of the surfaces relative to bulk - to lower the overall free energy of the system - normally results in a charged zone close to the interface where the local electroneutrality is not fulfilled. In general, the interfaces are almost always charged, and this has four main reasons:

1. Dissociation of surface groups
2. Adsorption of ions
3. Dissolution of ions
4. Isomorphous substitutions

Dissociation is common for oxides' surfaces where the surfaces have an isoelectric point at a given pH and are either acidic, neutral or basic. The isoelectric point (IEP) is defined as the

pH where the surface is electrically neutral. *Adsorption* of ionic surface-active substances will often determine the charge, *e.g.* ionic surfactants. *Dissolution of ions* is typical for salts where the cations and anions have different sizes and are bound with different strength. "Neutral salt" will therefore have an excess of one of the ions on the surfaces. AgI particles in water are, by way of example, negatively charged. Finally, *isomorphous substitutions* mean that ions in crystal lattices are substituted by other ions of the same size, but with different charge. The crystal will then possess a deficit or an excess of charge. Typical examples are clay materials and layered double hydroxides (LDH).

3.2 Grain boundary transport in oxides

In this section, I will present the theory of the core-space-charge model applied to the grain boundary transport in solid materials. Transport properties of bulk are not the focus of this thesis, so I therefore refer readers to other literature such as *Defect and Transport in Crystalline Solids* by Per Kofstad and Truls Norby for more information about the topic.

Ionic conduction through bulk occurs via transport of defects, *e.g.* the migration of oxygen vacancies in YSZ. The transport properties of grain boundaries differ from those of bulk crystals due to a lack of symmetry. Only for situations where the conductivity of the grain boundaries is much higher than for bulk, the pathway along the parallel grain boundaries has to be taken into account. As mentioned earlier, parallel grain boundaries were at one point proposed to be the main diffusion path for protons in YSZ [7], but this has later been disproved [18]. Usually the conductivity thorough serial grain boundaries is significantly lower than the grain interior conductivity. The low grain boundary conductivity in acceptor doped ZrO_2 [56, 57], CeO_2 [58, 59], and $BaZrO_3$ [60] has been explained by the presence of excess positive charge in the grain boundary core resulting in a depletion of positive charge carriers in adjacent space charge layers (see Fig. 3.2). The reason for the redistribution of the defects at the grain boundaries is governed the by the occupation preference and the energy balance of each individual species along with possible interaction with the gas phase, which differ from the bulk state and giving rise to positive grain boundaries [61].

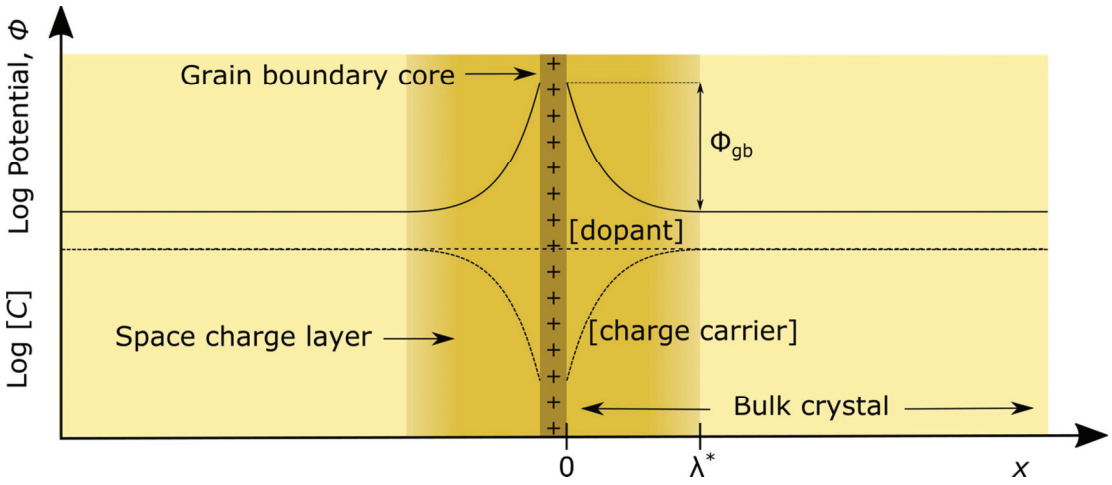

Fig. 3.2. Schematic grain boundary consisting of a positive core compensated by two adjacent space charge layers. Upper part: The unbroken line represents the potential profile and the Schottky barrier height is indicated. Lower part: The dashed lines represent concentration profiles for the charge carriers (positively charged) and the dopant under the Mott-Schottky approximation. The Debye length λ* is indicated.

For a full derivation of the resistance thorough the grain boundary relative to the bulk, see Ref. [62]. Here, I will only give the approximations and results for YSZ.

The positively charged core results in space charge layers where the positively charged oxygen vacancies are strongly depleted. By further considering the cations to be frozen-in (Mott-Schottky approximation), the acceptor concentration is assumed to be constant up to the grain boundary core and counter balancing the electroneutrality for the positively charged core. With these approximations, the Poisson equation can be solved analytically to find the space charge potential. The space charge zone is structurally a part of the bulk crystal, such that the mobility in the space charge zone can be assumed to be equal as in bulk. This allows solving the conductivity ratio between the bulk and grain boundary as function of the grain boundary potential, which for YSZ is:

$$\frac{\sigma_{\text{bulk}}}{\sigma_{\text{gb}}} = \frac{\exp\left(\frac{2e\varphi_{\text{gb}}}{k_{\text{B}}T}\right)}{\left(\frac{4e\varphi_{\text{gb}}}{k_{\text{B}}T}\right)} \tag{3.1}$$

From the equation we see that the grain boundary conductivity decreases with the barrier height φ_{gb}, which in reality is caused by depletions of charge carriers.

3.3 Solid-liquid interface: The Gouy-Chapmann model for electrical double layer

In the water layer above the charged surface there will exist a surface layer with opposite charge. Together, the charged solid surface and interfacial region of the liquid comprises the electric double layer. The theory required to describe the charge distribution near the surface – and which will later in the manuscripts be proven to be invaluable to understand protonic surface conduction – is presented in the following.

The Gouy-Chapmann model explains the capacitance-like qualities of the electric double layer, where the thermal motions of the ions are accounted for by assuming a Boltzmann distribution. In the Gouy-Chapmann approximation used for liquid (or solids at very high temperatures), all ions are considered mobile on the contrary to the Mott-Schottky approximation used for the solid-solid grain boundary.

Close to the surface, in the diffuse part of the double layer, there will be shortage of ions of same charge (co-ions) and excess of ions of opposite charge (counter-ions) to the surface charge. Fig. 3.3 illustrates the concentration of co-ions and counter ions and the net charge as function of distance from the surface.

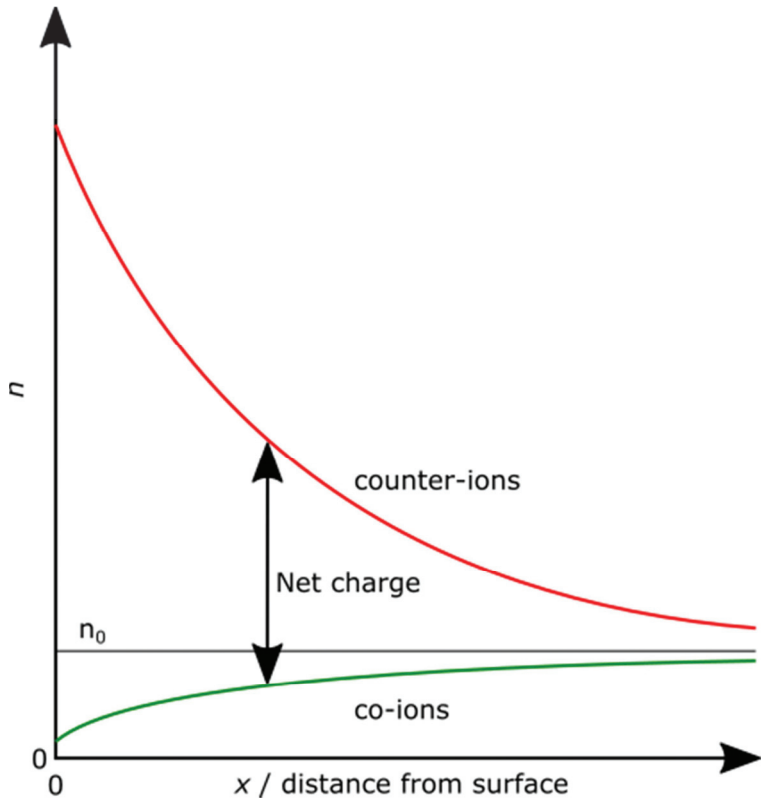

Fig. 3.3. Sketch of counter- and co-ion charge distributions as function of distance from the surface. Net charge is indicated.

The most important assumptions of the Gouy-Chapman model are that all ions in the solutions are considered to be point charges and follow a Boltzmann distribution. Further, the correlation between the ions is not taken into account, it is assuming symmetrical electrolytes, and the surface charge is assumed to be homogeneous. This allows for solving the full Poisson-Boltzmann equation in the water layer above the surface, which reads:

$$\nabla^2\psi = -\frac{Q_s}{\varepsilon} = \frac{-e}{\varepsilon\varepsilon_0}\left(c^+ - c^-\right) = \frac{-e}{\varepsilon\varepsilon_0}\left(c_0\exp(-e\psi) - c_0\exp(e\psi)\right) = \frac{-ec_0}{\varepsilon\varepsilon_0}\left(\exp(-e\psi) - \exp(e\psi)\right) \tag{3.2}$$

where ψ denotes the potential, Q_s the charge density, ε the dielectric constant of the medium, ε_0 the permittivity of free space, c^+ and c^- is the concentration of counter- and co-ions, c_0 the bulk concentration of ions in the solution, and e the elementary charge. $|e\psi|$ is the work required to bring a charged ion to the surface with a potential ψ.

The Poisson-Boltzmann equation can be solved analytically for planar surfaces, which is relevant for surfaces in porous oxides. (For full derivations of the solutions see *e.g. Principles of colloid and surface chemistry 3rd edition* by Hiemenz and Rajagopalan.) The general solution that must be used for high surface potentials, ψ is:

$$\psi(x) = -\frac{4k_BT}{e}\ln\frac{\exp\left(\frac{e\psi_0}{2k_BT}\right)+1+\left(\exp\left(\frac{e\psi_0}{2k_BT}\right)-1\right)\exp(-\kappa x)}{\exp\left(\frac{e\psi_0}{2k_BT}\right)+1-\left(\exp\left(\frac{e\psi_0}{2k_BT}\right)-1\right)\exp(-\kappa x)} \tag{3.3}$$

where ψ_0 is the potential at the surface, and κ^{-1} is the Debye length. κ^{-1} is generally mentioned as the "thickness" of the electric double layer and takes the following form:

$$\kappa = \left(\frac{2e2c_0}{\varepsilon\varepsilon_0 k_BT}\right)^{1/2} \tag{3.4}$$

For small potentials, when $e\psi < k_BT$ (ψ <25.7 mV), the linearized Boltzmann distributions can be used. This is mentioned as the Debye-Hückel approxiamtion. The solution of the Poisson-Boltzmann equation for a flat double layer then takes the much easier form:

$$\psi(x) = \psi_0\exp(-\kappa x) \tag{3.5}$$

We see from Eqs. 3.3 and 3.5 that the surface potential is ψ_0 at the surface and decays to 0 far away from the surface, which is reasonable.

3.3.1 Stern modification of the Gouy-Chapmann model.

In cases with high surface potentials, the assumption about a single diffusive double layer is unrealistic because of the size of the ions. Using the Boltzmann distribution simply gives higher ion concentration than the water itself. The observed capacitances of surfaces are also measured to be much lower than calculated from the Gouy-Chapmann model. A more realistic model has therefore been developed by Stern, and is called the Stern modification. The Stern layer is generally considered to be approximately 0.6-0.9 nm [63]. Typically water layers in porous oxides are in that range at 60% RH [31].

The Stern model takes the size of the ions and their binding characteristics into consideration and uses the Langmuir theory to describe the adsorption of ions on the inner surface layer. The potential drop then takes a linear drop in the Stern layer:

$$\psi(x) = \frac{-Q_s x}{\varepsilon\varepsilon_0} \tag{3.6}$$

where the Q_s is the surface charge density. Outside the Stern layer, the Gouy-Chapmann model is used and the $\psi_0$is replaced by the Stern potential ψ_δ.

Fig. 3.4 summarizes the electrical double layer on an YSZ surface, where the surface is negatively charged and protons function as the counter-ions and hydroxide ions as the co-ions. The potential drop in the water layer is sketched on the right of the figure. The shear plane in the figure corresponds to the “slip plane”, where the surface and the bulk move relative to each other. Zeta potential is the potential that is measured experimentally during shear process.

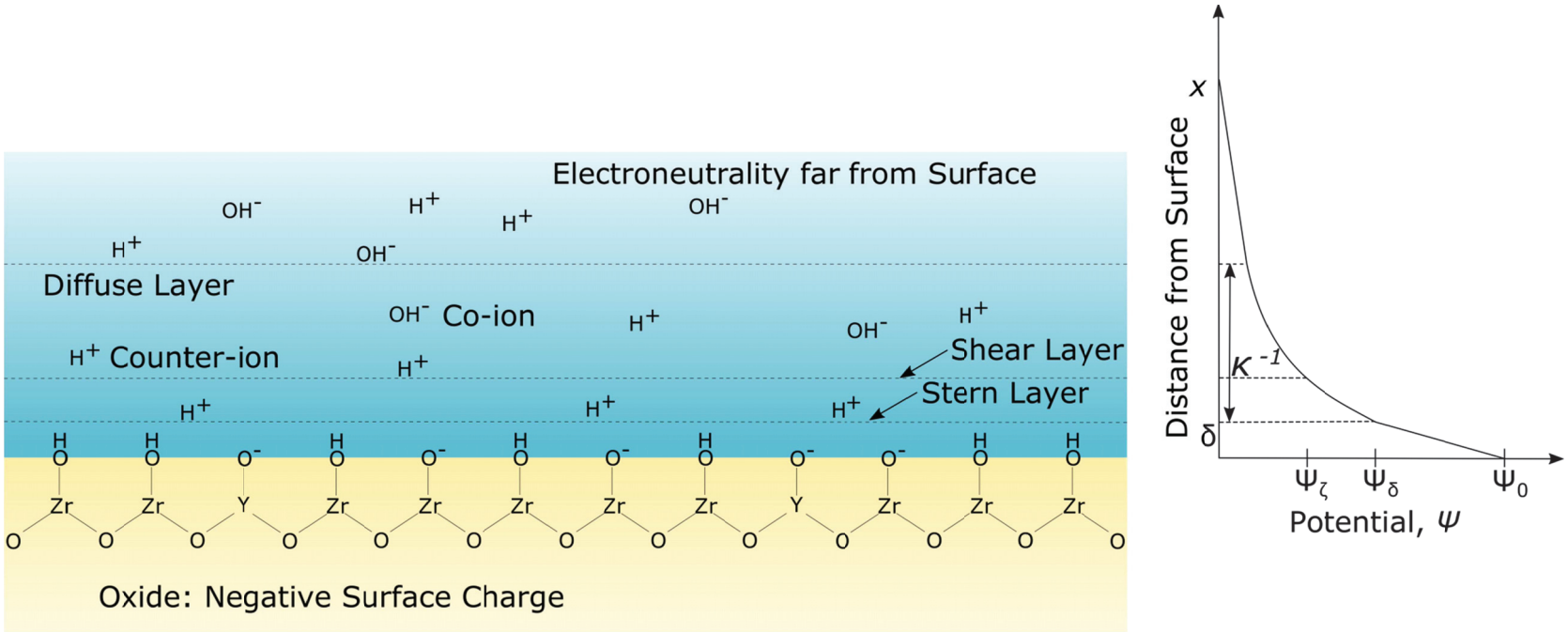

Fig. 3.4. Left: Sketch of the electric double layer on the YSZ surface, where the surface is slightly acidic and negative [1]. Protons are in majority and are counter-ions and hydroxide ions almost depleted as co-ions in pure water. The shear layer and Stern layer are indicated. Right: Surface potential as function of distance from surface. Potential drop is linear in the Stern layer and follows exponential in Gouy-Chapmann region outside the Stern layer. The "thickness" κ^{-1} of the double layer is indicated.

4 Methodology

This part describes the experimental work in this thesis and is intended as supplementary to the information given in the manuscripts.

4.1 Apparatus for electrical measurements

4.1.1 Measurement cell

Samples were mounted in a ProboStat measuring cell (NorECs, Norway) as described in Fig. 4.1. This setup allows for various types of electrical measurements in controlled atmospheres at desired temperatures. The temperature was controlled by a heating mantle placed around the measurement cell connected with a thermocouple placed next to the sample and a PID regulator (Eurotherm 2216). Small thermal fluctuation can affect the protonic conduction in porous oxides significantly, as described in the previous chapters. Based on experiences from logging of temperature, the thermal fluctuations are found to be less than 0.1 °C, resulting in stable conditions for electrical measurements.

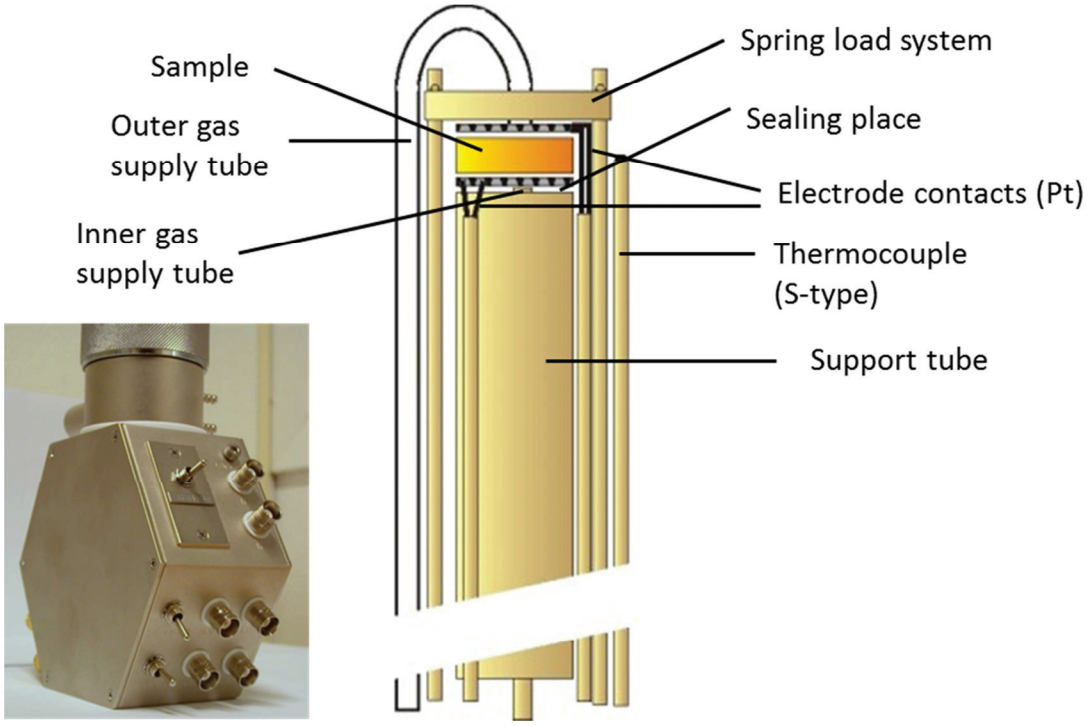

Fig. 4.1. Setup for electrical measurements. Left: ProboStat measurement cell with connections to electrodes with BNC connectors, Right: Schematic details from upper part of cell where the sample is mounted. All pictures/figures: NorECs, Norway (www.norecs.com).

The electrical properties of the samples were investigated by connecting electrode contacts in pairs of two of platinum wires to the electrodes on the sample. The electrodes were applied in different ways and described in detail in each manuscript. BNC cables were used to connect the measurement cell to the impedance analyser, shielding the electrical signals.

4.1.2 Humidification of gas

The partial pressure of water in the measurement cell was controlled by an in-house built gas mixer, schematically shown in Fig. 4.2. The gas mixer was either based on mass-flow-controllers (red-y, Vögtlin instruments) or rotameteres (Sho-Rate 1355, Brooks Instrument). The p_{H_2O} (or p_{D_2O}) was set by passing a fraction of the gas through water and then a saturated solution of KBr, and the other fraction through a drying stage (P_2O_5) or bypassing it. A saturated solution of KBr reduces the relative humidity to around 0.84, and ensures no condensation of water in the pipes and measurement setup. This setup allows varying the p_{H_2O} up to 0.026 atm at 25 °C. For measurements where a p_{H_2O} higher than 0.026 atm was needed, the gas was passed through a temperature controlled water stage. All pipes and the measurement cell were heated to higher temperature than dew point, to avoid condensation of water in this setup.

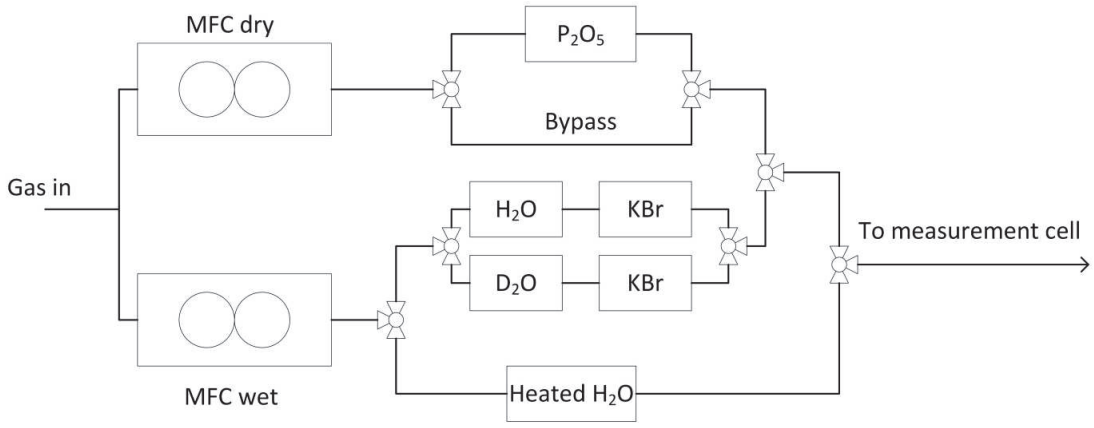

Fig. 4.2. Schematic drawing of the gas mixer used to humidify the gas for the electrical measurements.

When H/D isotope exchange measurements were performed, the gas was passed through D_2O instead of H_2O. The difference in the partial pressure of D_2O and H_2O is 0.003 atm at RT, a relatively large difference. This will lead to a significantly lower proton concentration in situations that is dependent on the absolute pressure of water vapour as in the chemisorbed water layer, but will be insignificant in situations where the amount of protons are dependent on the relative water vapour pressure, as in the physisorbed water layer (see Section 2.1.2 for detailed derivations of the amount of water in the samples).

4.2 Impedance spectroscopy

In this thesis, we deal with porous ceramics as YSZ and TiO_2 where the electrical properties at high temperatures are well characterised and understood (see *e.g.* [56, 64]). Impedance spectroscopy is used as the main technique in this thesis to understand how mobile species are transported under an electrochemical potential gradient in porous ceramics at low and intermediate temperatures. Introduction to impedance spectroscopy is therefore emphasised.

Impedance spectroscopy is a suitable technique to study ionic conductivity in ceramics because it allows differentiating transport processes with different time constants, *e.g.* grain interior and grain boundaries. Another important advantage is that the technique eliminates the need of reversible electrodes.

The impedance of the sample are measured over a broad range of frequencies, typically in the range between 10 MHz to 1 mHz in this thesis. A small AC perturbation (typically 0.1V), with frequencies corresponding to the different time constants, gives a phase shift between current and potential. By Fourier transformation, the complex relation between relaxation and phase shift is simplified from time to frequency domain. The impedance $Z(\omega)$ can then be expressed by its real and imaginary components:

$$Z(\omega) = Z' + iZ'' \tag{4.1}$$

A plot of Z' against Z'' over a given frequency range gives a so called Nyquist representation of the impedance data (See Fig. 4.3).

Impedance spectra obtained of the investigated samples are fitted to an equivalent circuit (See Fig. 4.3) for the electrical transport in the sample. For ceramic samples (*e.g.* YSZ), the high frequency part of the spectrum is related to bulk transport and the grain boundary and electrode response follows at lower frequencies and they are fitted to an equivalent circuit consisting of these three transport processes in series. For porous ceramics where transport along the pore surfaces must be considered in addition, no suitable equivalent circuit has up to now been developed. Before reviewing the strategies that have typically been employed for fitting impedance responses of these oxides, I will introduce the reader to some general concept for fitting of impedance spectra.

Ionic transport through bulk can be represented by a parallel circuit of a resistor (R) and a capacitor (C), due to charge transfer through the material and charge accumulation in the material. This parallel circuit is denoted as (RC). The capacitor behaviour of a polycrystalline material is usually not ideal, commonly attributed to a distribution in time constants from the individual grains. The capacitor is therefore often replaced with a constant phase element (CPE) which uses a normal distribution of the logarithm of the time constants, then denoted as (RQ). The impedance of a CPE is defined as:

$$Z_{\mathrm{CPE}} = \frac{1}{Y(i\omega)^n} \tag{4.2}$$

where $i = \sqrt{-1}$, and ω is the angular frequency. The parameter Y and n defines the CPE in such a way that for the special cases the where n=1, 0.5, 0, and -1, the CPE represent a pure capacitor, a Warburg element, a resistor, and an inductor, respectively. In this work, the CPE is only used for describing the non-ideal capacitive behaviour, when 0<n<1. A pseudo-capacitance (C_{CPE}) from the non-ideal capacitor can be calculated based on the values Y and n:

$$C_{\mathrm{CPE}} = Y^{-n} R^{(n^{-1}-1)} \tag{4.3}$$

The porous ceramics which are studied in literature (*e.g.* YSZ and GDC) and in this thesis have highly resistive grain boundaries; another (RC) circuit is added in series to the grain interior as depicted in Fig. 4.3. From Chapter 2 we know that the protons are transported in the water layer, and suggestions have been made to simply add a (RC) circuit for the surface transport inn parallel to the (RC)(RC) circuits for bulk and grain boundaries (See Fig. 4.3) [7, 65]. Further, the impedance data in those particular studies were deconvoluted using the (RC)(RC) circuits for bulk and grain boundaries for the high temperature data and just the (RC) circuit related to the protonic surface transport for the low temperature data.

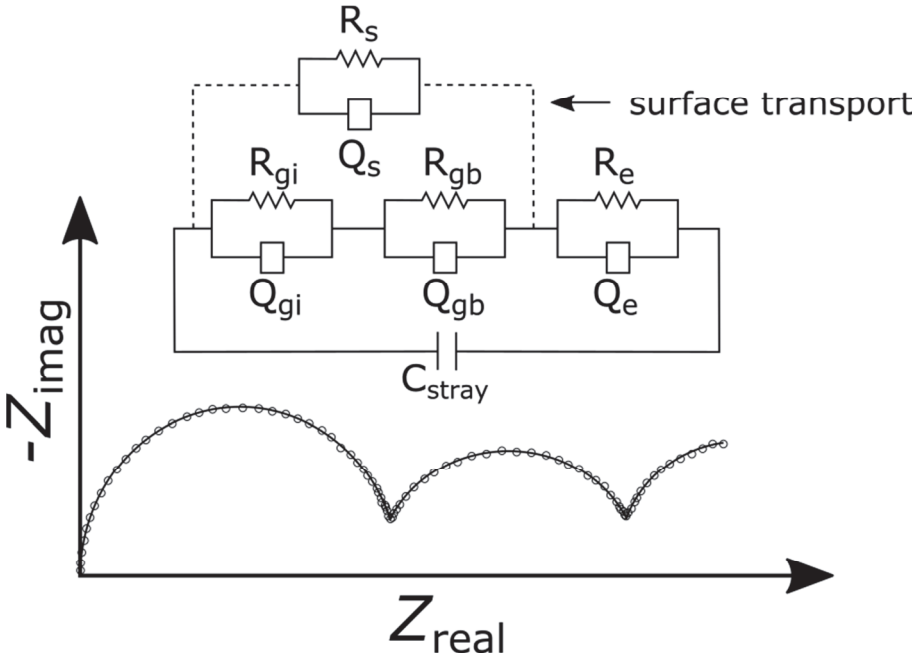

Fig. 4.3. Lower part: Nyquist plot of a typical polycrystalline material consisting of bulk response at high frequency followed by grain boundary and electrode response. Upper part: Equivalent circuit for a polycrystalline material (unbroken lines) consisting of three RQ-elements in series and the stray capacitance originated from the measurement setup. The equivalent circuit suggested for parallel protonic surface transport in literature [7, 65] includes the dashed rail.

An equivalent circuit for the total electrical transport in porous oxides which satisfactorily provides a complete analysis of the conductivity over large temperature and humidity spans will explicitly be presented and discussed in Manuscripts 1 and 2. Prior to that, the conditions that must be fulfilled to prove a correct equivalent circuit model will be discussed here.

The central criteria to prove the validity of the model are that the capacitances, and in additions the Y and n parameters, are stable or follow linearity within the considered temperature and water vapour pressure range. This condition proves that we are studying the same transport processes observed at different temperature and humidity. Fulfilling these requirements can be rather challenging for porous oxides, but nevertheless it is more important than to obey the best individual fit for each spectrum. There are two main reasons that it is challenging. Firstly, several transport processes with quite similar time constants simultaneously occur in parallel throughout the sample and secondly, that the ceramic matrix acts as stray capacitor, similar to the substrate in in-plane measurements of thin films.

The very high impedance at low temperatures and low RH of porous oxides can cause problems observing the true impedance of the sample. An impedance analyser with high input impedance is obvious. Of similar reasons, a measurement cell with higher impedance than the sample is important to avoid parallel leakage currents through the measurements. Another problem with high impedance samples is obtaining impedance data of sufficient quality due to interference with electrical equipment around the setup. An example can be observed for the data marked “without modifications” in Fig. 4.4. The largest source of noise was found to rise from the small current necessary to read the voltage from the thermocouple. We experienced that, by grounding the thermocouple and shielding the cell with aluminium foil, the noise was eliminated (see Fig. 4.4).

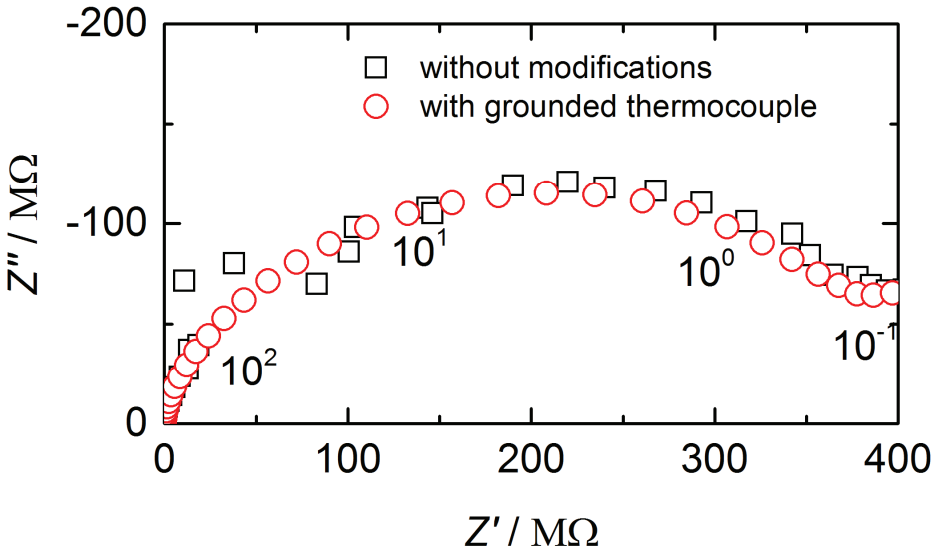

Fig. 4.4. Impedance response of a YSZ sample sintered at 1250 °C for 2 h measured at 100 °C in humidified atmosphere with and without grounding the thermocouple.

All the experimentally obtained impedance data were fitted using the ZView software from Scribner Associates, Inc.

4.3 Transport number measurements used to determine the protonic species

Transport number measurements are generally used to determine the fraction of ionic transport and different ionic species through the material. The transport number t_k of ion k is defined as:

$$t_k = \frac{\sigma_k}{\sigma_{tot}} \tag{4.4}$$

where σ_k and σ_{tot} is the conductivity of specie k and the total conductivity, respectively. Transport number measurements are in this thesis used to study the protonic transport in porous oxides, and as we will see later, it can be used to distinguish between protonic charge carriers.

In general, a gradient in the activity of a dissolved chemical species x will give rise to an electromotive force (*emf*) over a material. If there is only one dominating ionic charge carrier and the sample is equipped with two equal, inert electrodes at same absolute temperature T, and no external current is drawn, the measured voltage over the sample is [66]:

$$E_{II-I} = -\frac{k_B T}{ze}\int_{I}^{II} t_{x^z} d\ln a_x \tag{4.5}$$

where k_B is the Boltzmann constant, z is the charges, e is the elementary charge, a_x the activity of the neutral species x, and t_{x^z} is the transport number for species x.

When small activity gradients are used and a mean transport number can be assumed constant throughout the sample, Eq. 4.5 can be integrated to give:

$$E_{\mathrm{II-I}} = -t_{x^z} \frac{k_B T}{ze} \ln a_x \tag{4.6}$$

By exposing each of the sealed sample sides to different atmospheres (thus a_x^{I} and a_x^{II} is known), the mean transport number can be calculated from the measured voltage $(E_{\mathrm{II-I}})$ over the sample. (See Fig. 4.4 for set up.) A gradient in the activity of O_2 will set up a chemical gradient for all ions in equilibrium with O_2 in the system and give the total ionic transport number [66].

$$E_{\mathrm{II-I}} = -t_{\mathrm{M+O}} \frac{k_B T}{4e} \ln\left(\frac{p_{\mathrm{O_2}}^{\mathrm{II}}}{p_{\mathrm{O_2}}^{\mathrm{I}}}\right) \tag{4.7}$$

For evaluation of the protonic transport number and charge carrier mechanism for porous oxides under wet conditions, the chemical equilibrium between water and oxygen must be taken into consideration:

$$2\mathrm{H_2O} = 2\mathrm{H_2} + \mathrm{O_2} \tag{4.8}$$

Inserting H_2 for x in Eq. 4.6, and using the equilibrium above, Eq. 4.6 becomes:

$$E_{\mathrm{II-I}} = -t_{\mathrm{H^+}} \frac{k_B T}{2e} \ln\left(\frac{p_{\mathrm{H_2}}^{\mathrm{II}}}{p_{\mathrm{H_2}}^{\mathrm{I}}}\right) = t_{\mathrm{H^+}} \frac{k_B T}{4e}\left[-2\ln\left(\frac{p_{\mathrm{H_2O}}^{\mathrm{II}}}{p_{\mathrm{H_2O}}^{\mathrm{I}}}\right) + \ln\left(\frac{p_{\mathrm{O_2}}^{\mathrm{II}}}{p_{\mathrm{O_2}}^{\mathrm{I}}}\right)\right] \tag{4.9}$$

The transport number of protons can then be found measuring the sample under a gradient of water, with equal oxygen pressure. To figure out whether the protons move as free protons or are carried as OH^- or H_3O^+, or generally hydrated protons $(\mathrm{H_2O})_{\mathrm{m}}^{+}$ in porous oxides, the following equilibrium reactions must be taken into consideration:

$$4\mathrm{OH} = 2\mathrm{H_2O} + \mathrm{O_2} \tag{4.10}$$

$$2(2\mathrm{m}+1)\mathrm{H_2O} = 4(\mathrm{H}\cdot(\mathrm{H_2O})_{\mathrm{m}}) + \mathrm{O_2} \tag{4.11}$$

Where the activity of the neutral species "OH and $4(\mathrm{H}\cdot(\mathrm{H_2O})_\mathrm{m})$" (which exist statistically but in very minute amounts) will set up a chemical potential gradient for the respective ions. The related *emf* equations that can be evaluated are:

$$E_{\mathrm{II-I}} = t_{\mathrm{OH^-}} \frac{k_\mathrm{B}T}{2e}\left[2\ln\left(\frac{p^{\mathrm{II}}_{\mathrm{H_2O}}}{p^{\mathrm{I}}_{\mathrm{H_2O}}}\right)+\ln\left(\frac{p^{\mathrm{II}}_{\mathrm{O_2}}}{p^{\mathrm{I}}_{\mathrm{O_2}}}\right)\right] \tag{4.12}$$

$$E_{\mathrm{II-I}} = t_{\mathrm{H_{2m+1}O_m^+}} \frac{k_\mathrm{B}T}{4e}\left[-2(2m+1)\ln\left(\frac{p^{\mathrm{II}}_{\mathrm{H_2O}}}{p^{\mathrm{I}}_{\mathrm{H_2O}}}\right)+\ln\left(\frac{p^{\mathrm{II}}_{\mathrm{O_2}}}{p^{\mathrm{I}}_{\mathrm{O_2}}}\right)\right] \tag{4.13}$$

By measuring under a water vapor gradient only (and no gradient in $p_{\mathrm{O_2}}$), we see from Eqs. 4.9, 4.12 and 4.13 that the measured *emf* and the sign of the voltage will be dependent of the protonic charge carrier. If the transport is dominated by OH^-, the observed *emf* will have opposite sign compared to transport of protons or hydrated protons. Eq. 4.13 depicts that the measured *emf* voltage is $2m$+1 times higher for materials where hydrated protons are transported with m molecules of water constituting the vehicle. Materials dominated by hydroxonium ion (H_3O^+) transport will *e.g.* give an *emf* voltage three times higher than a pure proton conductor. By evaluating these equations the observed voltage can be used to determine whether the transport is dominated by Grotthuss type or vehicle mechanism, and, in the latter case, the degree of hydration of the protons.

For high impedance samples, parasitic current leakages cause problems for transport number measurements, as they cause polarisation and loss of *emf.* In our measurements, we have used a high impedance electrometer and driven shields to reduce this problem, see schematic in Fig. 4.5. Here, the DC voltage is measured over a cell with high DC resistivity due to large electrode impedance contributions. This could in principle be solved using reversible electrodes, but this is challenging for such low temperatures. Moreover, the measurements become challenging due to the relatively low *emf* voltages induces by the small water vapour gradients imposed over the sample.

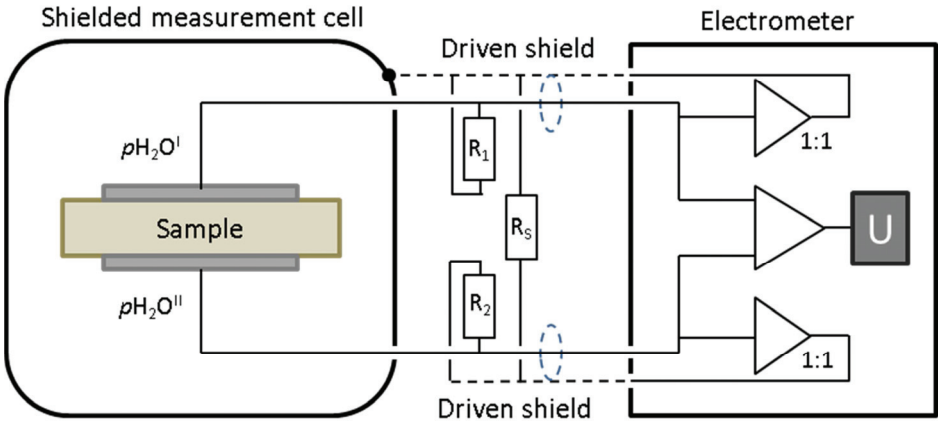

Fig. 4.5. Simplified circuit for measurements of the voltage of a sample under a gradient of water by using driven shields of the electrometer to eliminate leakage currents from the parasitic paths between signal and shield (R_1, R_2) and between shields (R_S).

One uses shielding of cell and wires to reduce noise, but as the figure shows, there are parasitic conductances between signal wires and shields (R_1 and R_2) and between the shields (R_S), providing the path for parasitic leakage between the two electrodes. The electrometer stops this by driving each shield to exactly the same potential as the signal wire itself. In this way, no current can run between each signal wire and its shield. There will run current in the path between the shields (R_S) but this has no consequence as long as the resistance R_S is reasonably large. The electrometer drives the shields by passing each signal potential through a high impedance amplifier so as not to load it with any additional current, and outputs it to the shield. In addition, the shielded cell is kept at the same potential as one of the electrodes and not connected to ground. Then there is no driving force for stray current between the cell chassis and the sample.

5 Manuscripts

I **On the interaction of grain boundaries and protonic surface transport in porous oxides**
Sindre Østby Stub, Einar Vøllestad, Per Martin Rørvik and Truls Norby
To be submitted

II **Protonic surface conduction controlled by space charge of intersecting grain boundaries in porous ceramics**
Sindre Østby Stub, Einar Vøllestad and Truls Norby
Submitted to Nature Communications

III **Protonic surface transport mechanism in porous oxides: example of YSZ**
Sindre Østby Stub, Einar Vøllestad and Truls Norby
Accepted for publication in The Journal of Physical Chemistry C

IV **Influence of acceptor and donor doping on protonic surface conduction of TiO_2**
Sindre Stub, Knut Thorshaug, Per Martin Rørvik, Einar Vøllestad and Truls Norby
To be submitted to Journal of the American Ceramic Society

6 Further results and summarising discussion

The Manuscripts presented in this thesis address various aspects of the fundamental properties of protonic conduction in porous oxides. Evidence for two protonic transport processes connected in series along surfaces was, for the first time, presented and discussed in Manuscript I and II. These are suggested to represent *intra-grain* transport – along the single grain's surface and *inter-grain* transport – across the intersection between two adjacent grains, where the latter is highly resistive at low relative humidity. Moreover, the protonic surface transport mechanism was investigated in Manuscript III, while influence of doping of the matrix on the protonic conduction was the focus in Manuscript IV. The key findings from the Manuscripts, supported by new and relevant results, will here be discussed collectively, thus allowing for new perspectives beyond the framework of each individual manuscript. The following discussion will be divided into aspects and properties related to the *intra-grain* and *inter-grain* transport.

6.1 Intra grain properties of materials

It was long debated in the literature whether the protons are conducted along the grain boundaries (*e.g.* in a space charge zone or in the very grain boundary core), or in the adsorbed water layer on the inner surfaces [4, 7, 14-17]. Prior to this work, it seemed clear that the protonic conduction occurs via chemisorbed and physisorbed water on the inner surfaces [18-21], which is supported by the results in this thesis. The concentration of mobile protonic species in the water layer is determined by the acid-base properties of the porous host oxide and surface chemistry as derived in Section 2 and Manuscript III [21, 28, 67]. Moreover, the type of protonic charge carrier and transport mechanism was in Manuscript III shown to change from protons and Grotthuss type at low relative humidity when the water layer show an "ice-like" structure, to hydroxonium ions (H_3O^+) and vehicular transport above 60% RH when the water layer shows liquid-like properties.

Prior to this work, the relation between the conductivity and the thickness of the water layer was poorly understood. This has been discussed in various forms in the Manuscripts, and will be central in the following discussion, related to the conduction both in the chemisorbed and physisorbed water layer. The section will end with a comparison between proton conduction in bulk of ceramic, chemisorbed and physisorbed water.

6.1.1 Concentration dependent conductivity

In this work, the protonic conduction in porous 8YSZ and TiO_2 has been investigated over wide ranges of relative humidity and temperatures. In Fig. 6.1 the temperature dependent conductivities measured under fixed partial pressure of water are shown together with literature data. The conductivities show similar behaviour as reported in literature [14, 18, 20, 26], decreasing conductivity with decreasing temperature at high temperatures, and increasing conductivity with decreasing temperature and increasing relative humidity at low temperatures. Furthermore, the temperature dependent conductivities measured under fixed RH are presented together with literature data in Fig. 6.2. The conductivities show Arrhenius behaviour in line with literature [10, 22, 27]. Moreover, the conductivity increases significantly with increasing RH, whereas the activation energies simultaneously decrease. The RH dependent conductivities collected at 25 ºC in the present work, are shown in Fig. 6.3 as a function of water layer thickness. Although the protonic conductivity of the samples investigated in this work and in literature shows consistency in temperature and humidity dependency, the spread in conductivity between the samples is large. Based on knowledge from Manuscript III and IV, the latter must be attributed to different specific surface area and surface acidity of the samples. The following discussion will evaluate the expression of the conductivity and in particular the dependency of water concentration.

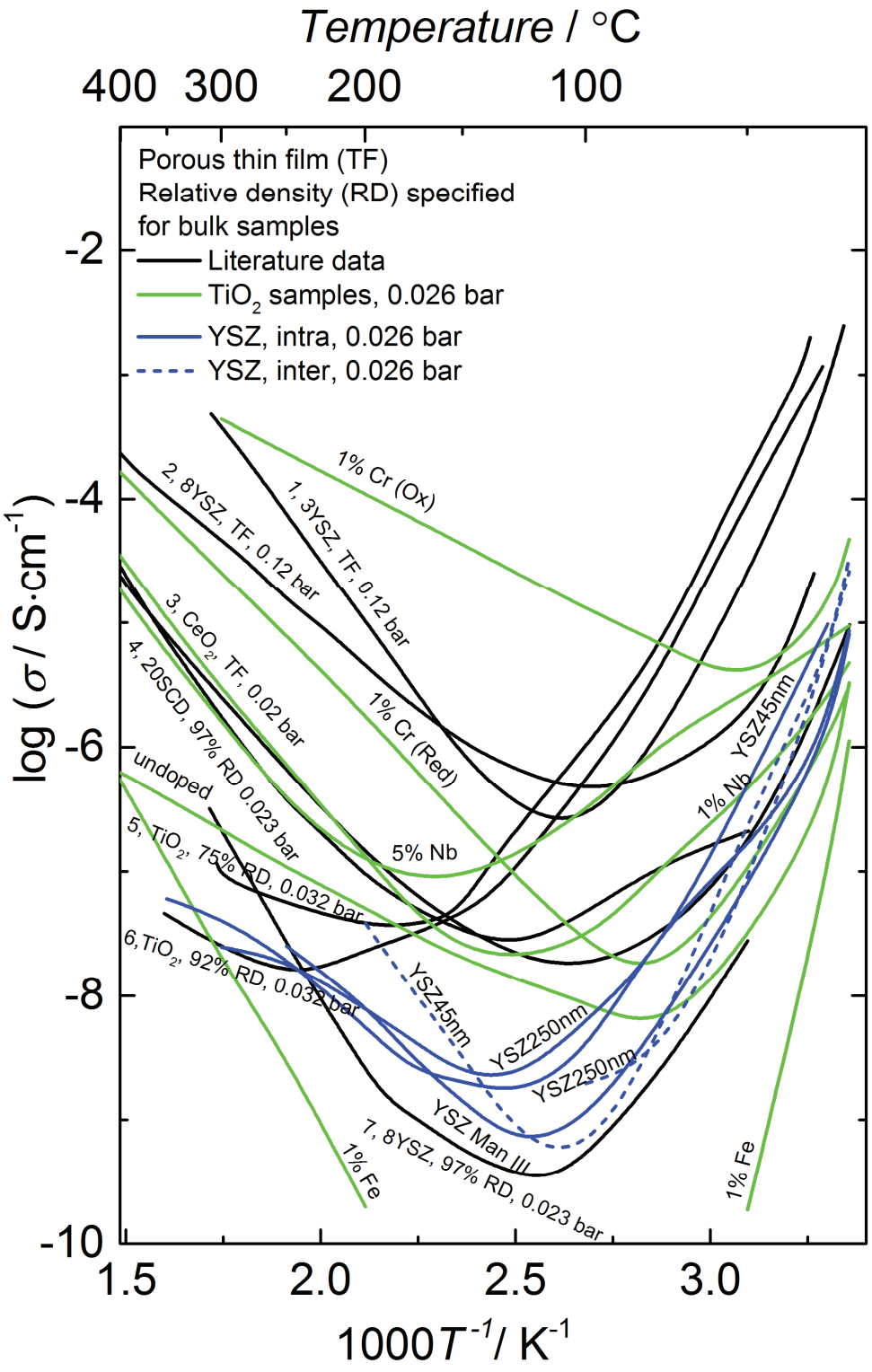

Fig. 6.1 Conductivities as a function of temperature at fixed partial pressure of water (given in bar). Data plotted in black and red taken from literature. Relative densities (RD) of samples are specified for bulk samples. 1: 3YSZ [18], 2: 8YSZ [18] 3: CeO_2 [14], 4: 20SCD [26], 5: TiO_2 [20], 6: TiO_2 [20], 7: 8YSZ [26], 8: SOH_3 functionalised SiO_2 [22], 9: TiO_2 [10], 10: Silica xerogel [27]. The conductivity of 8YSZ from Manuscript I-III is plotted in blue, and the conductivity of the TiO_2-samples from Manuscript IV is plotted in green.

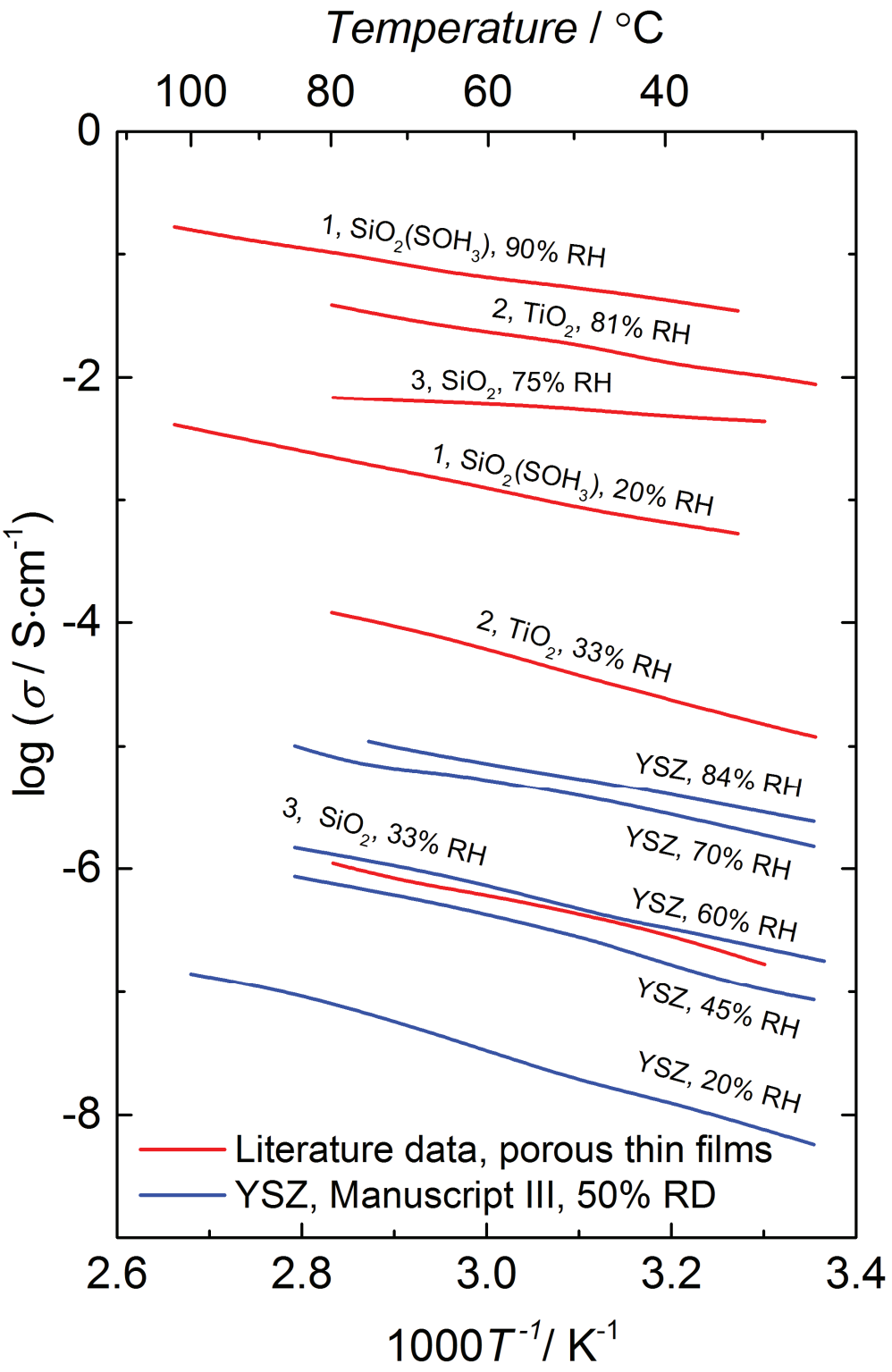

Fig 6.2. Conductivities as a function of temperature at fixed relative humidity (RH). Data plotted in red are taken from literature, all porous thin films. 1: SOH_3 functionalised SiO_2 [22], 2: TiO_2 [10], 3: Silica xerogel [27]. The conductivity of porous 8YSZ from Manuscript III (50% relative density) is plotted in blue.

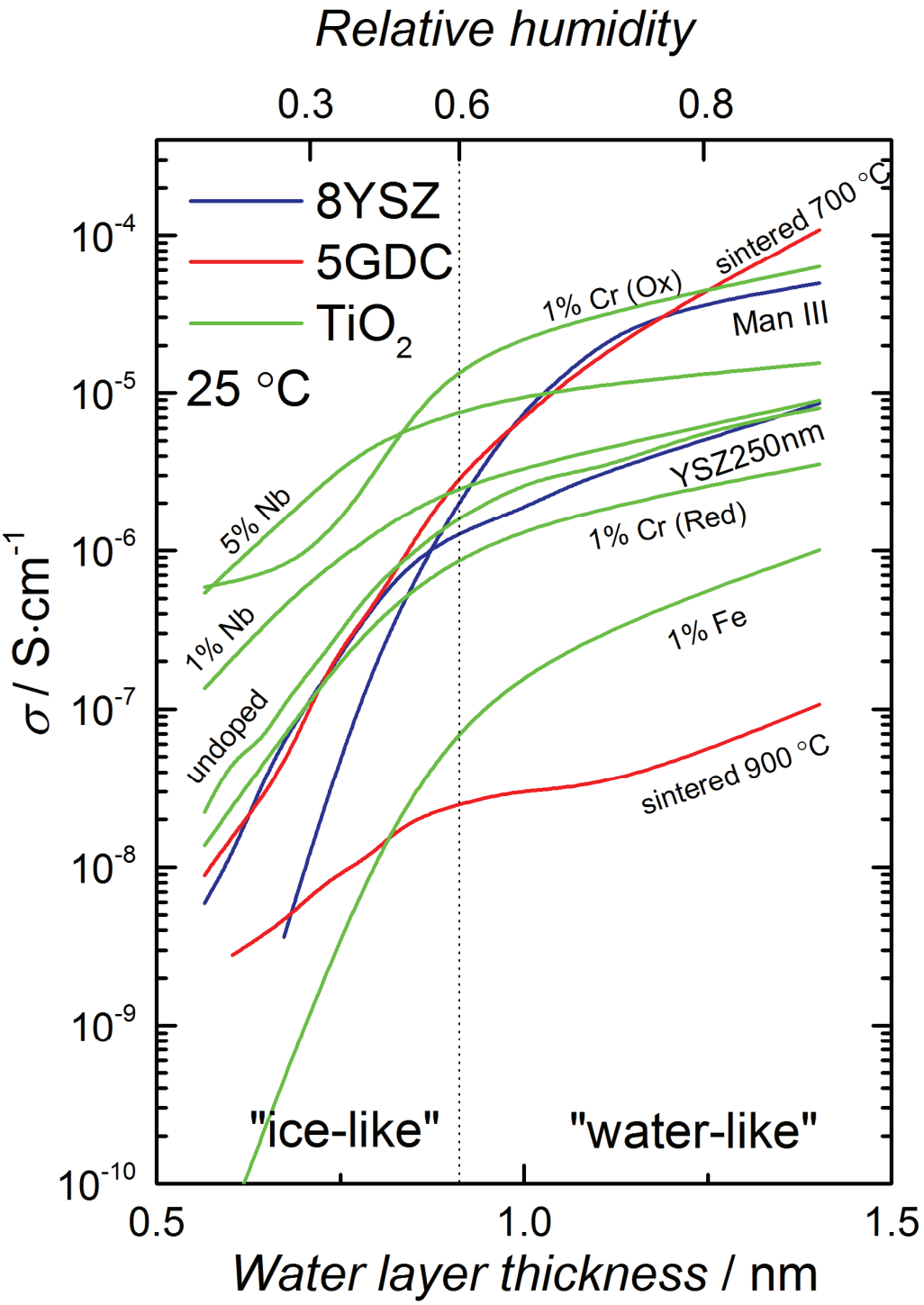

Fig. 6.3. Conductivities as function of water layer thickness of all samples measured in this work. The water layer thickness is to a first approximation assumed from water adsorption measurement on YSZ-powder (Manuscript II), adjusting it to the surface area of the sample (YSZ250nm), using a density of 4.6 water molecules per nm^2 in the water layer [68] and a corresponding thickness of the water layer of 2.82Å [31] for all samples.

The expression for the intra-grain conductivity as a function of partial pressure of water and temperature was derived in Section 2.3.4 (and Manuscript III):

$$\sigma_{\mathrm{ph}}(T,p)=\sqrt{\frac{c\left(\frac{p}{p_0}\right)v_m}{\left(1-\left(\frac{p}{p_0}\right)\right)\left(1+(c-1)\left(\frac{p}{p_0}\right)\right)}}\sqrt{[\equiv \mathrm{ZrOH_2}]^0 S_{\mathrm{BET}}\rho}\cdot \\ F\frac{\mu_{0,\mathrm{ph}}}{T}\exp\left(\frac{\Delta S_{\mathrm{D,ph}}}{2R}\right)\exp\left(-\frac{\frac{1}{2}\Delta H_{\mathrm{D,ph}}+\Delta H_{\mathrm{mob,ph}}}{RT}\right) \tag{6.1}$$

From Eq. 6.1 we see that the conductivity is proportional to the square root of the water concentration, given by the BET-equation. It should be noted that all concentrations are expressed in terms of mol per surface area. Thus, the water concentration shows a one to one correlation with the water layer thickness.

The water concentration dependency of the conductivity is, as pointed out in the manuscripts, much stronger than given in Eq. 6.1. Fig. 6.3 shows the measured concentration dependency directly, as the conductivity is plotted as a function of the water layer thickness. The conductivity of the samples increases several orders of magnitudes meanwhile the concentration of water only increases by a factor of approximately three in the experimental window. This strong dependency is in the literature attributed to a humidity or thickness dependent enthalpy of mobility, and enthalpy and entropy of defect formation [28]. In the following, the obtained activation energies and pre-exponentials for intra-grain conductivity in Manuscript III will be used to elucidate some important aspects of the concentration dependency.

Fig. 6.4 shows the obtained activation energies for intra-grain conductivity of YSZ (Manuscript III) as a function of water layer thickness. The activation energy for intra-grain transport in the hydrogen bonded water layer of YSZ45nm as found in Manuscript I is added for comparison (here recalculated for σT vs $1/T$). The water layer thickness is calculated based on water adsorption measurement on YSZ-powder (Manuscript II), adjusting it to the surface area of the sample (YSZ250nm), using a density of 4.6 water molecules per nm^2 in the water layer [68] and a corresponding thickness of the water layer of 2.82Å [31]. The hydrogen bonded layer corresponds to a water layer thickness of approximately 0.45 nm, assuming two monolayers.

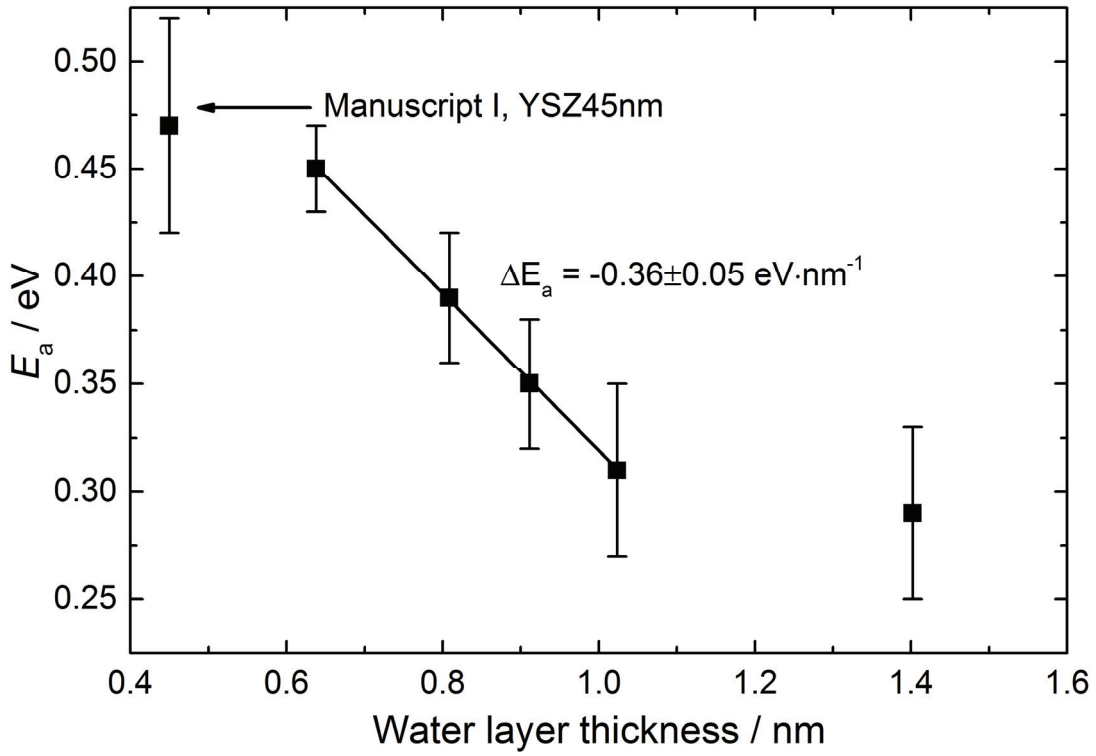

Fig. 6.4: Activation energies extracted in Manuscript I and III as a function of water layer thickness of 8 YSZ. By linear fitting the slope is found to be -0.36±0.05 eVnm^{-1} and the activation energy is extrapolated to be 0.68±0.05 eV for transport on the very surface.

The result indicates that the activation energy decreases linearly within a distance of approximately 1 nm from the surface. The slope is calculated to be -0.36±0.05 eV·nm^{-1} and the activation energy of the conductivity on the surface can be extrapolated to be 0.68±0.05 eV. However, the validity of this extrapolation to lower RH and thinner water layer thicknesses is uncertain. The activation energy of the intra-grain conductivity of the YSZ45nm sample for the hydrogen bonded layer (~0.45nm) in the temperature range 125 to 200 ºC was found to be 0.47±0.05eV. It may indicate that the activation energy differs from linearity in the chemisorbed water layer. It should be pointed out that this activation energy is extracted from another measurement and another sample. The activation energy at 0.45 nm is from transport in the chemisorbed water layer, whereas the others are extracted from transport in the physisorbed water. All in all, it cannot be concluded whether the linearity can be extrapolated to the surface or not.

The small difference in activation energy between the points at ~1 nm (70% RH) and ~1.4 nm (84% RH) indicates that the enthalpy of mobility and defect formation decrease to a constant level above a certain water layer thickness, approximately 1 nm . At ~1 nm water layer thickness, the thickness dependencies of the conductivities in Fig. 6.3 change as well, and the results are thus in good agreement with each other. The constant value of the

activation energy above 1 nm can be rationalised by the fact that the enthalpies will decrease to their water bulk levels at a certain water layer thickness. As earlier discussed in the Manuscripts, this coincides with the change of the water layer properties around 60% RH (~0.9 nm) [31], where the water layer starts to show liquid-like properties, such that bulk water values of the enthalpies can be expected. Similar observations are seen for proton conduction in Nafion, where the activation energy is thickness dependent and reaches a minimum level [53]. For further work, it would have been interesting to find the separate contributions from the enthalpy change of mobility and dissociation. The self-diffusion of protons can for example be studied directly by ^{1}H-NMR.

The pre exponential terms of the measured temperature dependent conductivities at fixed RH in Manuscript III fall within a narrow range (between 50 and 120 $S \cdot cm^{-1} \cdot K$) without any systematic correlation with water layer thickness. This result thus indicates that the entropy of proton formation $\left(\Delta S_D^0\right)$ and pre exponential term of mobility (μ_0) are independent on water concentration, in contradiction to the strong dependency of ΔS_D^0 claimed by Kreüer *et al.* [28]. However, it cannot be ruled out that ΔS_D^0 and μ_0 show opposite behaviour and thus cancel each other.

In the last part of this section I want to evaluate the direct water concentration dependency in Eq. 6.1. The full expression for the conductivity in the physisorbed water (Eq. 6.1) shows a square root dependency of the water concentration as a result of derivation presented in Chapter 2 and Manuscript III. The proton mobility in the chemisorbed water layer was in Section 2.3.3 derived to be dependent on vacant sites into which the protons can move and hence it is dependent on the water concentration. No such dependency was included in the expression of the mobility in the physisorbed water in Section 2.3.4, because the experience shows the mobility to be independent on the number of vacant sites. From the results in Figs. 6.1 and 6.3 I want to evaluate if the mobility expression in the physisorbed water also should be directly dependent on the concentration of physisorbed water. Then Eq. 6.1 should be multiplied with the water concentration and show a power of three half dependency instead of a square root dependency of the water concentration (BET-part of equation).

From Fig. 6.3 it is hard to verify one or the other, due to small changes in the concentration of water. However, in the temperature dependent measurements at fixed partial pressure of water (Fig. 6.1), the concentration of physisorbed water increases approximately 200 times upon reducing the temperature from 100 ºC to 25 ºC. In the same temperature interval the intra-grain conductivity of the YSZ samples increase by approximately four orders of magnitude. The strongly concentration dependent activation energies (Fig. 6.4) can account for one to two orders of magnitude increase in the conductivity in the same window. A square root dependency of the water concentration will result in additionally one order of magnitude of increase in the conductivity, whereas a power of three half will result in an increase of additionally three orders of magnitude. Thus, this indicates a stronger water dependency than

derived for the intra-grain conductivity in the physisorbed water layer (Eq. 6.1) and most probably that the mobility is dependent on the water concentration. However, there are many uncertainties in the data. More measurements, ideally for different materials, are necessary to conclude.

6.1.2 Relation between concentration of water and conductivity in the chemisorbed water layer

In Section 2.3.3 the sample specific conductivity in the chemisorbed water layer was derived to be linearly dependent on the concentration of water. The water dependency will in the following be evaluated based on some new results.

The protonic conductivity of porous CeO_2 (Sigma Aldrich, USA, CeO_2 particles <25 nm, sintered for 2h at 1000ºC) was studied isothermally as function of partial pressure of water (0.026 - 0.30 atm) at 400 ºC and the behaviour is depicted in Fig 6.5. The intra-grain conductivity increases with the partial pressure of water, whereas the inter-grain conductivity remains constant with increasing partial pressure of water and shifts to a higher level around p_{H_2O} = 0.2 atm.

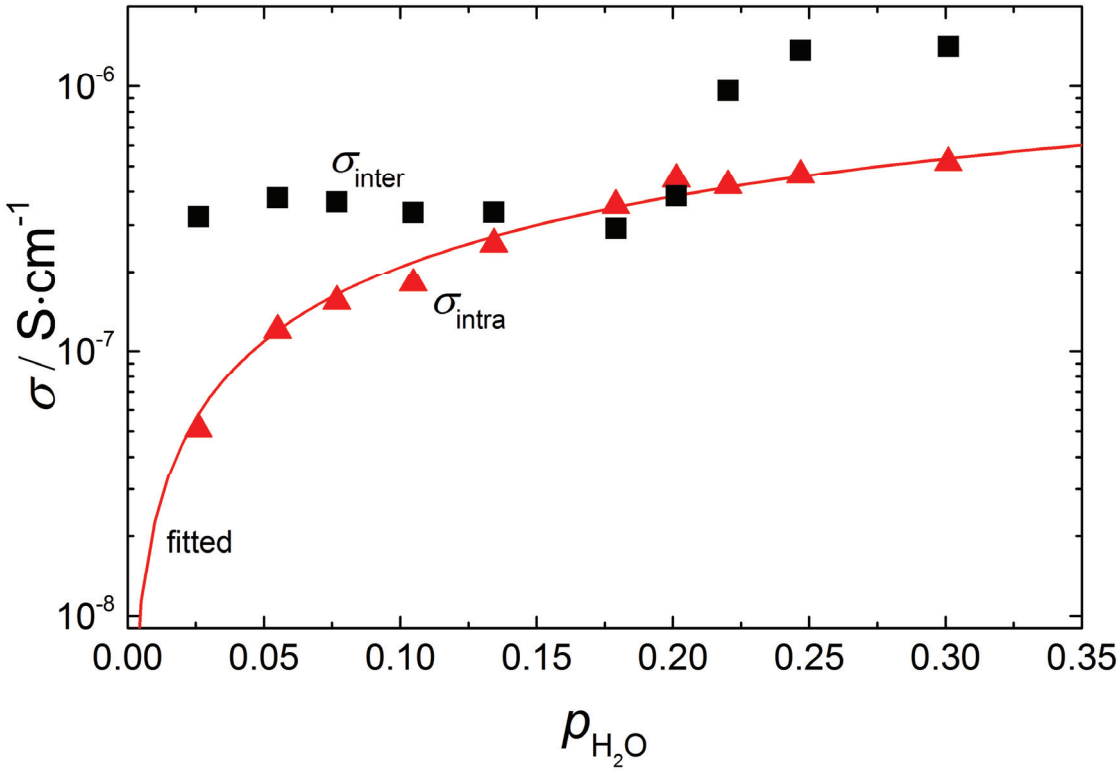

Fig. 6.5: The conductivity of the CeO_2 sample as function of partial pressure of water isothermally at 400 ºC.

Under isothermal conditions, the expression for the sample specific protonic conductivity in the chemisorbed layer (Eq. 2.24) can be simplified to:

$$\sigma_{\mathrm{ch}}(p_{\mathrm{H_2O}}) = \frac{\sigma_0}{\left(1 + p_{\mathrm{H_2O}}^{-1} K_0^{\mathrm{ch\text{-}1}} \exp\left(\frac{-60\,\mathrm{kJ\cdot mol^{-1}}}{673\,\mathrm{K}\cdot R\cdot \mathrm{J\cdot mol^{-1}K^{-1}}}\right)\right)} \tag{6.2}$$

where σ_0 is the conductivity at full coverage. From Eq. 6.2 we can see that the isothermal conductivity is solely dependent on the amount of water, given by the Langmuir isotherm. Given the heat of chemisorption of -60 kJ·mol^{-1} for CeO_2 from literature [69], the isothermal intra-grain conductivity can be fitted to Eq. 6.2 as shown in Fig. 6.5, where σ_0 and K_0^{ch} are determined to be 2.4×10^{-6} S·cm^{-1} and 2.0×10^{-5} atm^{-1}, respectively. The fitting to the Langmuir expression strongly indicates that there is a one to one relation between the conductivity in the chemisorbed water layer and the concentration of water. Thus, this result supports the derived behaviour in Section 2.3.3.

6.1.3 Comparison of properties and protonic conduction in bulk of ceramic, chemisorbed and physisorbed water

The protonic surface conductivity was in Manuscript IV shown to be higher for donor doped than acceptor doped porous oxides, strictly opposite to proton conduction in bulk of ceramics, where oxides are acceptor doped to improve the proton conductivity. With this section, I want to highlight similarities and differences between protonic surface conduction and ceramic bulk conduction to gain a better understating of protonic conduction overall.

The origin of protonic surface conduction in porous oxides is, as derived in Section 2, described by two reactions, the adsorption reactions (Eqs. 2.2 and 2.3) and the acid-base reactions between the oxide surface and water (Eqs. 2.8 and 2.15). The origin of protons in bulk is only described by one reaction: the hydration reaction of oxides:

$$\mathrm{O_O^{\times}} + \mathrm{v_O^{\bullet\bullet}} + \mathrm{H_2O\,(g)} = 2\mathrm{OH_O^{\bullet}} \tag{6.3}$$

For ceramic bulk proton conductors, an acceptor dopant is added to form oxygen vacancies which are needed for the material to hydrate and form protons according to the reaction in Eq. 6.3. Hydration of bulk is among other dependent on the basicity of the material and concentration of dopants. If we further focus on the role of dopants with respect to the proton conductivity, as adressed in Manuscript IV, it has been demonstrated that the enthalpy of hydration is significantly more exothermic for strong electronegative dopants in $BaCeO_3$ and $BaZrO_3$, a phenomenon caused by strong association energies between dopants and protons [70, 71]. High association energies simultaneously result in strong trapping of protons and thus, overall lower conductivity [70].

A similar trend can be observed for protonic surface conduction. In Manuscript IV, Fe-doped TiO_2 shows significantly lower protonic conductivity than Cr-doped and undoped TiO_2. The electronegativity for the studied species is 1.83, 1.66, and 1.54 for Fe, Cr, and Ti, respectively. Thus, the larger electronegativity for Fe than Cr and Ti can maybe explain why Fe-doped TiO_2 shows much lower conductivity than Cr-doped and undoped TiO_2, both dopants considered trivalent [72, 73].

Kreuer *et al.* claim that there is a relation between the enthalpy of hydration of surfaces (chemisorption) and the enthalpy of defect formation of protons, as they both seem to be of similar values [28]. Literature data indicates that higher acceptor concentrations lead to slightly more exothermic heat of adsorption [37] and the results from Manuscript IV indicate that decreasing average valence of the surface cations leads to decreasing concentration and mobility of protons. For ceramic bulk proton conductors, acceptor dopants that give rise to more negative hydration enthalpies also show lower mobility and lower concentrations of mobile protons (stronger association between dopants and protons) [70]. Thus, both surface transport and ceramic bulk transport of protons show similarities in relation to formation of protons and mobility of protons, and this substantiates that the hypothesis stated by Kreuer *et al.* may be right. Based on current knowledge it is however difficult to prove or disprove it, but it is an interesting question that should be studied further.

Although protonic surface and ceramic bulk transport properties are affected very differently by donor doping of the materials, protonic surface transport shows clear similarities with proton transport in ceramic bulk such as dopant influence on mobility and concentration of protons, and most probably the hydration thermodynamics. Roughly speaking, proton conduction in the chemisorbed layer can be seen as an extension of the bulk proton conduction where the protons jump from site to site and are limited by the association energy between the defect and proton (trapping, as discussed Manuscript I), whereas proton conduction in the physisorbed water layer must be understood as a clear two-phase system where the water layer and the oxide show totally different transport properties. This distinction is important when it comes to application where protonic porous oxides are intended used either at high or low temperature, or more precisely at low or high RH. At high temperature the heat of adsorption can be an important factor for hydration, and hence the choice of dopant. When conduction in the physisorbed water layer dominates, focus on acidic materials with high dissociation and mobility is important. Further investigation is however, important to fully understand the comparison and differences between protonic transport in ceramic bulk, chemisorbed water and physisorbed water. A summary of what is understood based on the results from the present work can be found in Table 1.

Table 1. Comparison of proton conduction in ceramic bulk, chemisorbed and physisorbed water layer.

	Ceramic bulk	Chemisorbed	Physisorbed
Phases	One-phase system	Hydroxyl layer: surface of the bulk. Hydrogen bonded layer: borderline	Two-phase system
Hydration enthalpy	Dependent on dopants and material [70]. Most probably dependent on degree of hydration [74].	Strongly dependent on material and degree of hydration [37, 69, 75, 76]. Most probably dependent on concentration of dopants [37].	Almost independent on coverage, dopants, and material.
Charge carrier and mechanism	H^+ Grotthuss type	H^+ (protons or "proton holes") Grotthuss type	<60% RH: H^+ (protons or "proton holes") Grotthuss type >60%: H_3O^+ or OH^- vehicular transport
Charge carrier concentration	~2[Acc] Dependent on type of dopant	Dependent on acidity of surface, $K_{a,ch}$, (dopants)	Dependent on acidity of surface, $K_{a,ph}$, (dopants) Strongly dependent on concentration of water.
Mobility	Dependent on trapping.	Most probably dependent on valence of dopants. Proportional to $[H_2O]$ in hydrogen bonded layer.	Most probably dependent on valence of dopants. Strongly dependent on concentration of water.

6.2 Origin and properties of the high inter-grain resistance

This section will focus on properties of the *inter-grain* transport process, which was presented in Manuscript I and II. An additional observation of two transport processes was given for Nb-doped TiO_2 in Manuscript IV. To substantiate that this is general for protonic surface conduction, results of protonic conduction in porous 5 mol% gadolinium-doped CeO_2 (5GDC) will be presented. Furthermore, the dependency of water concentration on the inter-grain conductivity will be discussed based on new results of activation energies extracted from temperature dependent conductivity measurements performed under fixed RH. This section will end with a derivation of a mathematical relation between the inter grain conductivity and water layer thickness.

6.2.1 Observation of two transport processes in 5GDC

Figure 6.6 a) shows the intra-grain and inter-grain conductivity of two porous 5GDC samples sintered at 700 ºC or 950 ºC. The YSZ sample from Manuscript II is added for comparison in b). The water layer thickness is to first approximation assumed to be equal for 8YSZ and 5GDC as a function of RH, and calculated as explained in Section 6.1.1. The GDC samples are made by a co-precipitation method, described in detail in Ref. [77], cold pressed isostatically at 150 MPa and sintered at 700 ºC or 950 ºC for two hours. The crystallite sizes are by Le Bail fitting of the X-ray diffractograms estimated to be 10±1 nm and 26±1 nm and the relative densities are measured by the geometric method to be 55% and 71% for the one sintered at 700 ºC and 950 ºC, respectively.

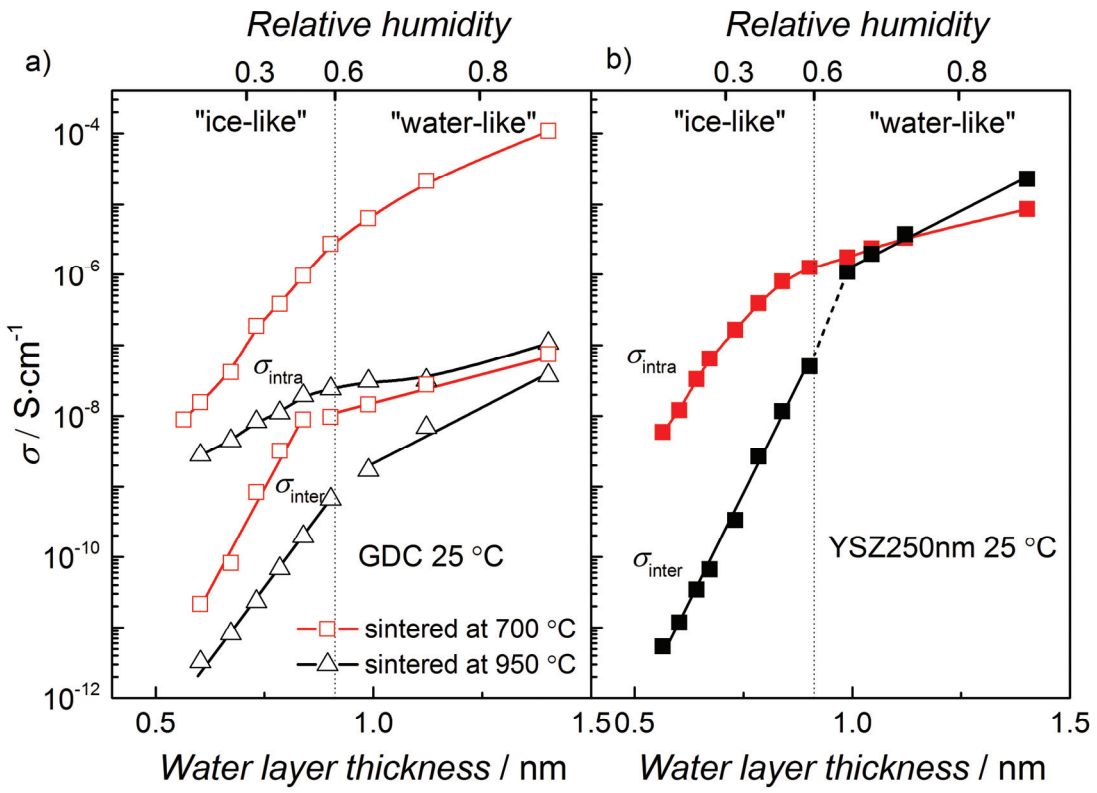

Fig. 6.6. Isothermal conductivity of a) GDC samples and b) YSZ250nm recorded at 25 °C under various relative humidity. Lines are guides to the eye only.

The intra-grain conductivity of the two samples shows different behaviour. Since this is out of the scope of this section, I will leave it there. However, the inter-grain conductivity of the GDC samples, which is in focus here, show similar behaviour as YSZ: an exponential relation between the conductivity and the water layer thickness and a distinct change in the slope around 60% RH. The high inter-grain resistance was in Manuscript I and II related to depletion of protonic charge carriers in the water layer above the highly positive grain boundaries. GDC has, like YSZ, shown to have highly positive grain boundary cores and subsequent space charge layers highly depleted of positive charge carriers [56, 62, 64, 78, 79]. The observation of two transport processes in GDC with similar behaviour thus supports the theory for highly resistive inter-grain conductivity presented in Manuscript I and II.

6.2.2 Concentration dependency on the inter-grain barrier of YSZ

In Manuscript III, the temperature dependent intra-grain conductivity of 8YSZ, measured at fixed RH, was presented. The corresponding results of the temperature dependent inter-grain conductivity are presented in Figure 6.7. The conductivity increases with increasing temperature and shows Arrhenius behaviour. The activation energies for the inter-grain conductivity are found by linear fitting of σT vs $1/T$ and are seen to decrease with increasing RH, similar to the activation energies for the intra-grain conductivity. The fitted values of the

pre exponentials fall within a narrow range (between 10^3 - 10^5 S·cm^{-1}·K) without any systematic change with RH. This indicates consistency of the electrical behaviour of the inter-grain process.

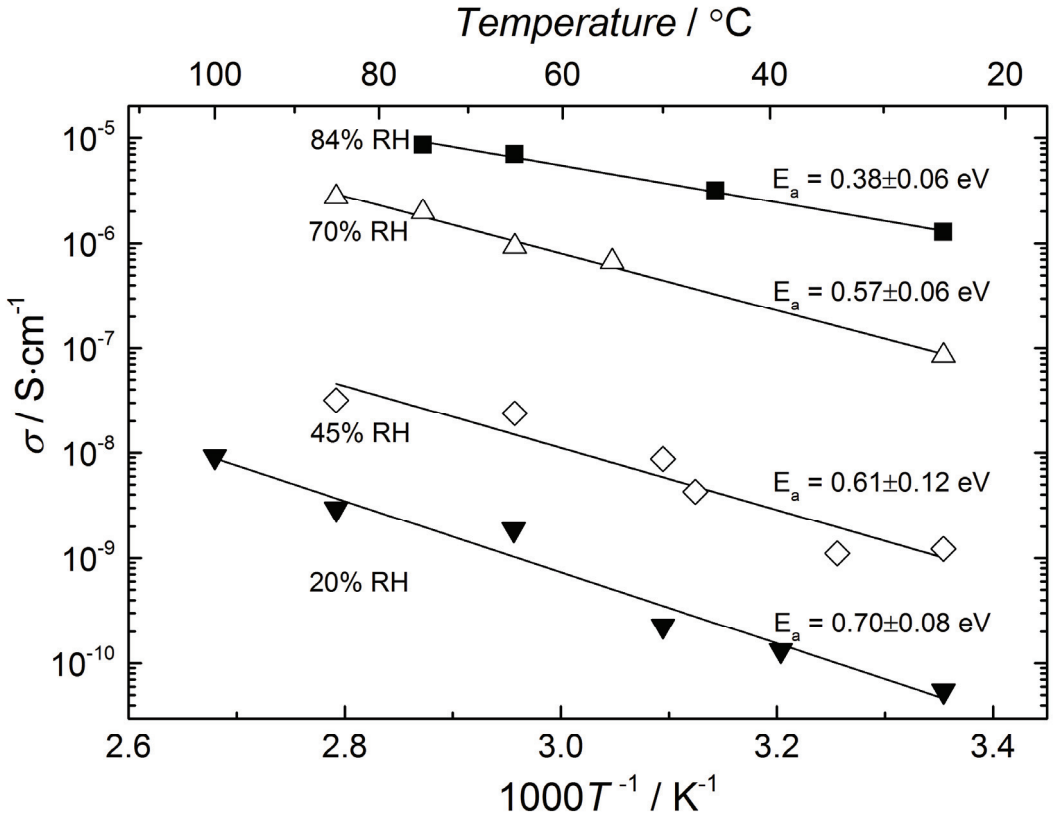

Fig. 6.7. Inter-grain conductivity of 8YSZ (used in Manuscript III) as function of temperature at fixed RH. The lines show the fitted activation energies.

Fig. 6.8 shows the activation energies extracted from Figure 6.7 as a function of water layer thickness. The activation energy for the inter-grain conductivity of YSZ45nm sample in Manuscript I is added for comparison (recalculated from σT vs $1/T$). The results indicate a linear decrease with a slope of 0.42±0.08 eVnm^{-1} for the activation energy as a function of the water layer thickness in the physisorbed part of the water layer. The activation energy extracted from the inter-grain conductivity in the hydrogen bonded water layer in Manuscript I deviates from the linear behaviour in the physisorbed water, indicating a different behaviour of inter-grain barrier in the chemisorbed and physisorbed water layer. This is not unlikely given the different transport properties in the chemisorbed and physisorbed water. By extrapolation of the linear fitting, the inter-grain barrier is calculated to effectively vanish when the water layer is 2.3±0.2 nm. This thickness will be achieved when the relative humidity exceeds approximately 95%.

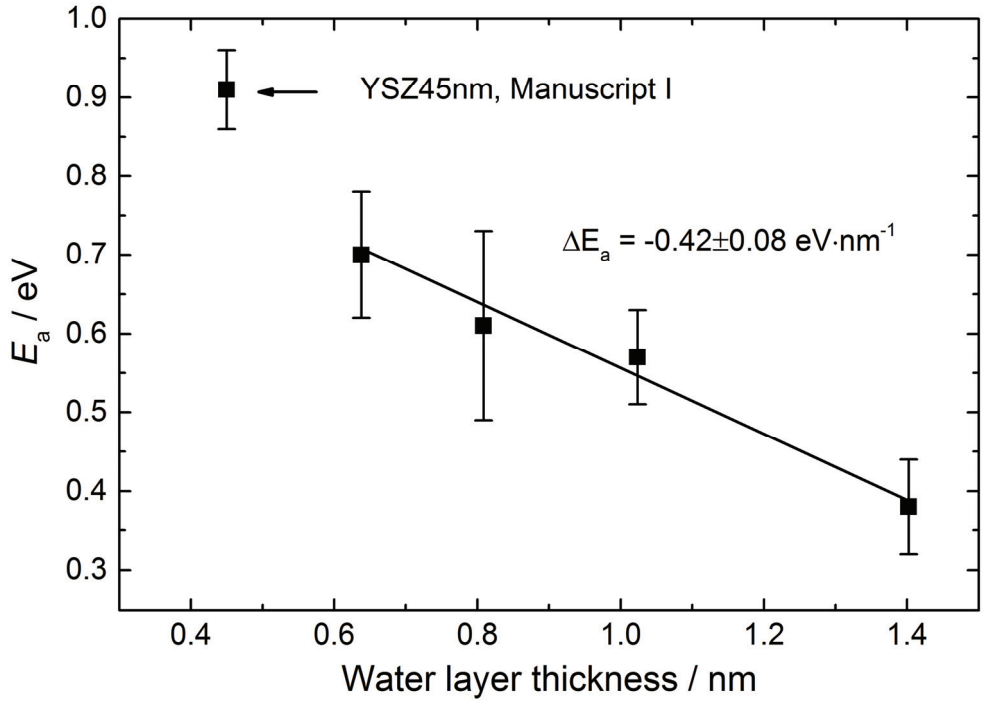

Fig. 6.8. Activation energies extracted from Fig. 6.7 and from Manuscript I as a function of water layer thickness. The slope of the fitted line is 0.42±0.08 eVnm^{-1}, and the fitted line is extrapolated to intersect the x-axis at 2.3±0.2 nm.

The results indicate that the activation energy decreases linearly throughout the experimental window in the physisorbed water, opposite to the activation energies of the intra-grain transport (Fig. 6.4) which was found to reach a constant value when the water layer showing bulk and "liquid-like" properties with a thickness above ~1 nm. The inter-grain barrier is caused by depletion of protonic charge carriers in the water layer above the highly positive grain boundaries. According to the theory of electrical double layers presented in Section 3.3 the concentration of co-ions (here protons) increases exponentially with the distance from the surface. The barrier will vanish at the thickness where the concentration of protons above the grain boundaries is approximately equal to the proton concentration above the surface, such that there is no depletion of protons. Thus this rationalises why the thickness dependencies of the activation energy is different for the intra-grain and inter-grain transport.

6.2.3 Mathematical expression for the inter-grain conductivity

In this section, a mathematical expression for the inter-grain conductivity as a function of water layer thickness will be derived, and substantiate that the large inter-grain resistance is caused by depletion of charge carriers. I will start with a description of the situation and present the assumptions before the mathematical relation is derived.

In Manuscript I and II, the origin of the resistive inter-grain transport was proposed to be the same as that of resistive grain boundaries in YSZ, namely the formation of a highly positive

grain boundary core between adjacent grains and subsequent space charge layers highly depleted of positive charge carriers [56, 62, 64, 78]. For the surface, the depletion zone then reaches into the adsorbed water layer. In contrast, the surface itself of YSZ is found to be negative – in agreement with a slightly acidic point of zero charge (pH~6) [1]. A schematic representation is presented in Fig. 6.9.

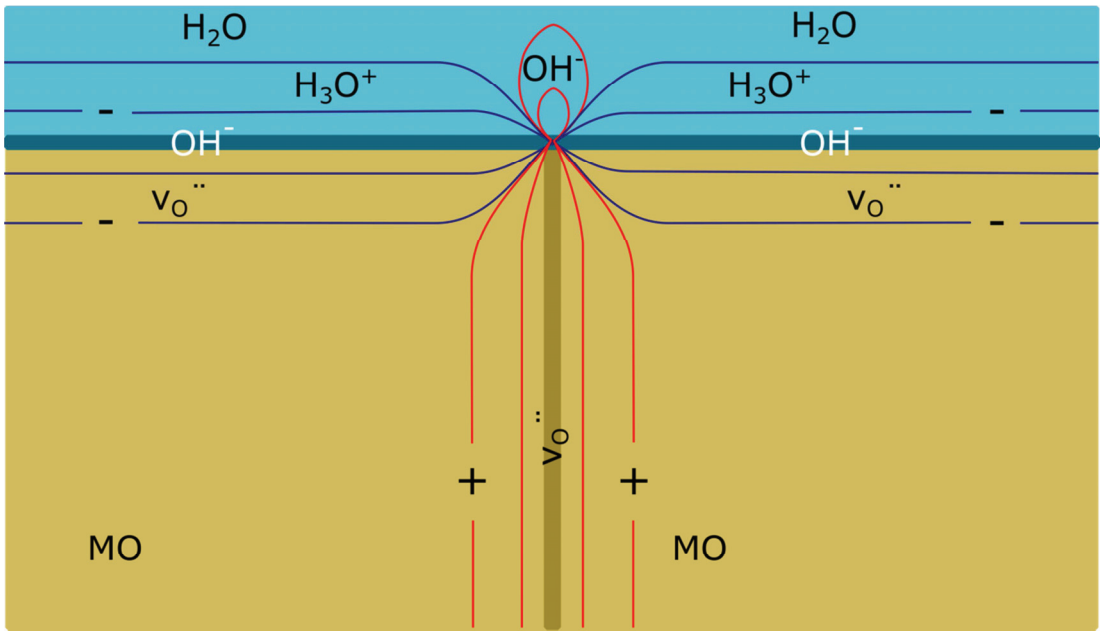

Fig. 6.9. Schematic illustration of the effects of space charges in the intercept of a grain boundary with adsorbed water on the surface of a ceramic oxide MO, taken from Manuscript II. The grain boundary core is positive from excess of effectively positive oxygen vacancies, while the surface is negative from excess of terminating hydroxide ions (thick lines). The resulting positive and negative potentials in the nearby space charge regions are represented by equipotential (thinner) lines. Charge carrying species enhanced in the space charge regions are indicated.

Fig. 6.10 shows a schematic of the extension of the space charge zone in the *x*-direction with the corresponding concentrations of protons and hydroxide ions as a function of water layers *dz* with the distance *z* from the surface. The depletion region consists of a core region above the grain boundary dominated by the co-ions (hydroxide ions) depleted of protons and two adjacent transition regions partly depleted of protons. The concentration of protons in the depletion core is much lower than in the subsequent transition regions, such that the limiting concentration of protons for the inter-grain conductivity is given by the concentration above the core region. Furthermore, it is reasonable to assume that the extension of the core and the subsequent transition area reduces in the *x* direction with the distance *z* from the surface, due to point charges along the grain boundary. However, the decreased extension of the space charge region is assumed to be small compared to the change in concentration in the *z* direction. Thus, the charge carrier concentration can to a first approximation be assumed to be a step function, and the problem can be described mathematically.

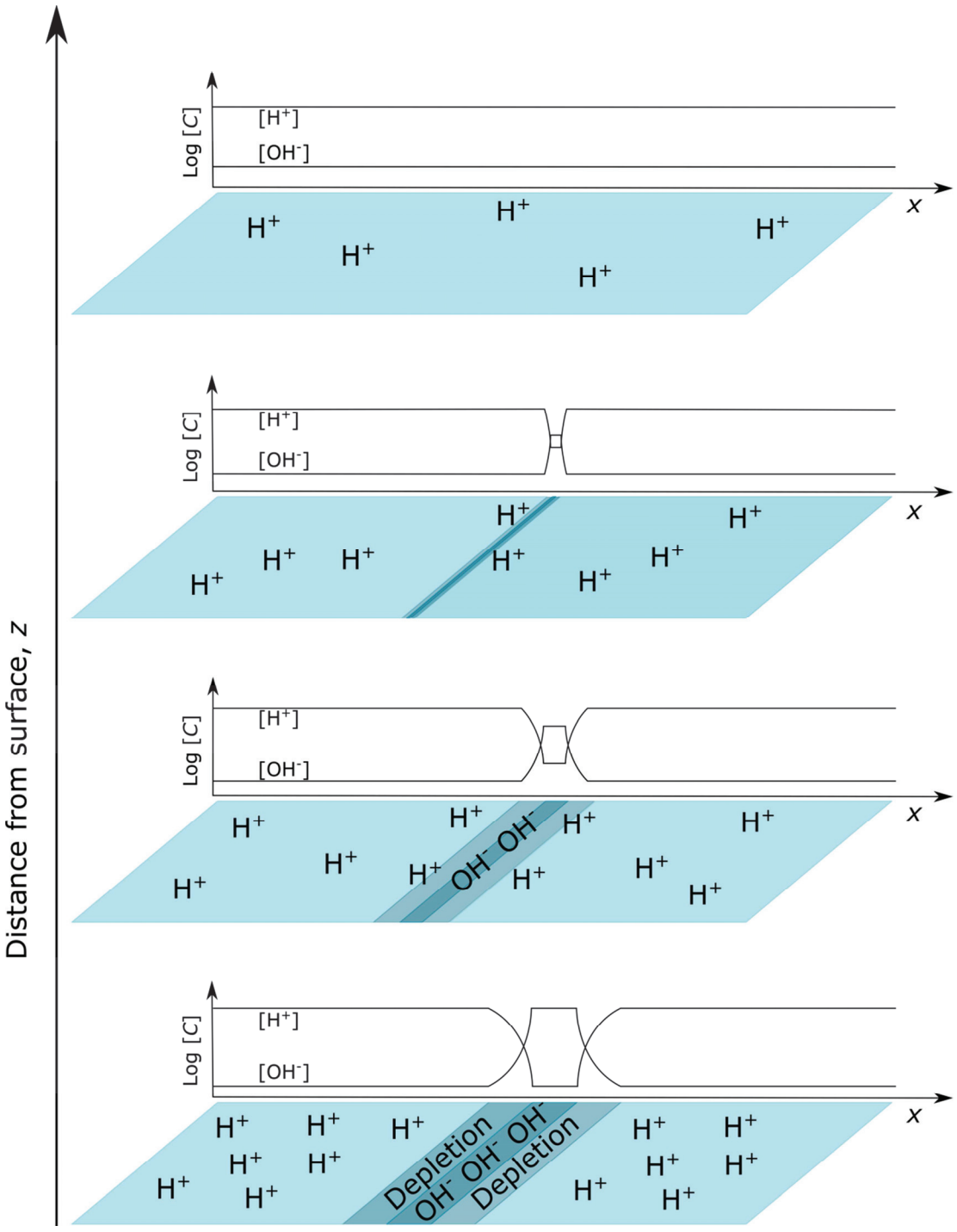

Fig. 6.10. Schematic illustrations of water layers as function of distance *z* from the surface with corresponding concentrations profiles as function of *x*. The concentration of OH^- (counter-ions) above the grain boundary – region marked in dark blue –is decreasing with distance *z* from the surface. The concentration of protons (co-ions) is in the same region increasing with distance *z*. Simultaneous the depletion region extension in the *x* direction is diminishing due to lower concentrations. It should also be marked that the concentration of protons above the surface – light blue – decreases with the distance z from the surface according to the double layer theory.

The concentration of positive protonic charge carriers in the water layer above the positive core can to a first approximation be expressed as a function of distance z into the water layer using a statistical Boltzmann distribution:

$$c(z) = c^0_{H^+} \exp\left(-\frac{e\Psi(z)}{k_B T}\right) \tag{6.4}$$

where $c^0_{H^+}$ is the proton concentration given in mol per surface area in the bulk region of the water, e the elementary charge, k_B the Boltzmann constant, T the absolute temperature and $\Psi(z)$ the net surface potential at distance z.

The water layer is of finite thickness, which has great influence on its charge distribution and limits the space to counter-balance the charged surface and grain boundary. The adsorbed water layer is at low RH thinner than what is normally mentioned as the Stern layer (approximately 1 nm or ~3 water layers [63]). The potential drop in the water layer is therefore assumed to be linear, considering the finite thickness is smaller than the Stern thickness and finally expressed as:

$$\Psi(z) = \frac{-Q_s}{\varepsilon_r \varepsilon_0} z \qquad \text{for z< 1 nm} \tag{6.5}$$

Where Q_s is the charge density of the surface given in charge per surface area and can be considered frozen in. ε_0 is the dielectric constant of vacuum and ε_r is the relative dielectric constant of the water phase.

Combining Eqs. 6.4 and 6.5, and integrating the concentration of protons from the very surface to the water layer thickness, z, gives the effective concentration of mobile charge carriers (protons), in mol per surface area, in the part of the water layer above the grain boundaries and contributing to the conduction in the x-direction:

$$c(z) = \int_0^z c(z')dz' = \int_0^z c^0_{H^+} \exp\left(\frac{eQ_s}{\varepsilon_r \varepsilon_0 k_B T} z'\right) dz' = c^0_{H^+} \frac{\varepsilon_r \varepsilon_0 k_B T}{eQ_s}\left(\exp\left(\frac{eQ_s}{\varepsilon_r \varepsilon_0 k_B T} z\right) - 1\right) \qquad \text{for z< 1 nm} \tag{6.6}$$

The boundary conditions gives that the concentration $c(z)$ equals zero at zero water layer thickness and diverges at infinite thickness as should be reasonable. At finite thickness as studied in this work, Eq. 6.6 reduces to

$$c(z) = c^0_{H^+} \frac{\varepsilon_r \varepsilon_0 k_B T}{eQ_s} \exp\left(\frac{eQ_s}{\varepsilon_r \varepsilon_0 k_B T} z\right) \qquad \text{for z< 1 nm} \tag{6.7}$$

since $\exp\left(\frac{eQ_s}{\varepsilon_r\varepsilon_0 k_B T} z\right) >> 1$.

Moreover, if we multiply the expression (Eq. 6.7) by the specific surface area (S_{BET}) and the gravimetric density of the sample (ρ), the charge carrier concentration can be expressed in terms of mol per volume sample. If we further take the grain boundary length to grain length ratio (g/G) into account, the concentration can be specified for the inter-grain volume of the sample. The grain boundary length to grain length ratio can be assumed from impedance measurements under dry conditions applying a Brick Layer model, see *e.g.* Ref [80]. The expression for the concentration given for the specific inter-grain volume in the sample then reads:

$$c(z) = c^0_{H^+} \frac{\varepsilon_r\varepsilon_0 k_B T}{eQ_s} S_{BET}\rho\left(\frac{g}{G}\right)\exp\left(\frac{eQ_s}{\varepsilon_r\varepsilon_0 k_B T} z\right) \qquad \text{for z< 1 nm} \qquad (6.8)$$

We have now expressed the thickness dependency of the concentration of protons in the inter-grain region of the water layer. Let us move on and do the same analysis for the mobility.

The mobility is dependent on the distance z into the water layer, and can to a first approximation be assumed to be dependent on the enthalpy only.

$$\mu(z) = \frac{\mu_0}{T}\exp\left(\frac{-\Delta H(z)}{k_B T}\right) \qquad (6.9)$$

From the result and discussion given in Section 6.1.1 this assumption is reasonable. By using the results from Section 6.1.1 and further assuming that the linearity holds for both the mobility and defect formation, $-\Delta H(z)$ can be expressed as $-\Delta H(z) - \Delta H_{mob} + \alpha z$, where ΔH_{mob} is the enthalpy of mobility at the surface and α is the slope related to the change in the enthalpy given in eV·nm^{-1}. Moreover, assuming the mobility is independent on the concentration; Eq. 6.9 can be integrated from the oxide surface to the thickness z to get the mobility in the total water layer:

$$\mu(z) = \int_0^z \mu(z')dz' = \int_0^z \frac{\mu_0}{T}\exp\left(-\frac{\Delta H^0 + \alpha z'}{k_B T}\right)dz' = \frac{\mu_0 k_B}{\alpha}\left(\exp\left(-\frac{\Delta H^0 + \alpha z}{k_B T}\right) - \exp\left(-\frac{\Delta H^0}{k_B T}\right)\right) \qquad (6.10)$$

Eq. 6.10 can be simplified to

$$\mu(z) = \frac{\mu_0 k_B}{\alpha} \exp\left(-\frac{\Delta H^0 + \alpha z}{k_B T}\right) \qquad \text{for z<1nm} \qquad (6.11)$$

since the mobility is much higher far from the surface, mathematically shown by:

$$\exp\left(-\frac{\Delta H^0 + \alpha z}{k_B T}\right) >> \exp\left(-\frac{\Delta H^0}{k_B T}\right) \qquad (6.12)$$

Above 1 nm the mobility is found to be constant with the water layer thickness and Eq. 6.11 takes the value at 1 nm.

With both an expression for the charge carrier concentration and mobility as function of water layer thickness, an expression for the sample specific inter-grain conductivity can be found by multiplying Eqs. 6.8 and 6.11 with the Faraday constant *F*. The expression then reads:

$$\sigma(z) = c^0_{H^+} \frac{\varepsilon_r \varepsilon_0 k_B T}{eQ_s} S_{BET} \rho \left(\frac{g}{G}\right) \exp\left(\frac{eQ_s}{\varepsilon_r \varepsilon_0 k_B T} z\right) \cdot \frac{\mu_0 k_B}{\alpha} \exp\left(-\frac{\Delta H^0 + \alpha z}{k_B T}\right) \cdot F \qquad \text{for z< 1 nm} \qquad (6.13)$$

On a logarithmic form, we see that the equation gives a straight line in a plot of the logarithm conductivity versus water layer thickness:

$$\ln \sigma_{inter}(z) = \frac{eQ_s - \varepsilon_r \varepsilon_0 \alpha}{\varepsilon_r \varepsilon_0 k_B T} z + \ln\left(F c^0_{H^+} \frac{\varepsilon_r \varepsilon_0 k_B T}{eQ_s} S_{BET} \rho \left(\frac{g}{G}\right) \frac{\mu_0 k_B}{\alpha}\right) - \frac{\Delta H^0}{k_B T} \qquad (6.14)$$

which is observed for the inter-grain conductivity in the “ice-like” region of the water layer for the samples of YSZ and GDC in Fig 6.6. Thus, depletion of charge carriers due to inversion of co- and counter-ions in the electric double layer above the grain boundary core rationalizes the large transport barrier observed for inter-grain protonic transport.

We also note from Eq. 6.14 that the dielectric constant of the water phase will affect the slope of inter-grain conductivity, which agrees well with the abrupt changes observed for both YSZ and GDC in Figure 6.6. The change in slope occurs at the point where the water layer changes from an “ice-like” to a “liquid-like” structure, associated with a drastic change in the dielectric constant [35, 81]. Moreover, as we saw in Section 6.1.1, the enthalpy of mobility seems to reach its bulk value of proton transport in liquid water approximately 1 nm out from the surface. Thus, part of the abrupt change in the slope around ~1 nm is therefore attributed to that the mobility of the protons reaches their bulk value of mobility in water and no longer changes with water layer thickness. Furthermore, it should be noted that the Eq. 6.14 is not strictly applicable outside ~1 nm, since Eqs. 6.5 to 6.8 are based on the Stern approximation.

However, a change in the slope caused by the aforementioned reasons should be observed whether the potential drop is linear (Stern) or exponential (Poisson Boltzmann) outside 1 nm.

Through this section we have seen similar behaviour for the inter-grain conductivity in both YSZ and GDC, two different materials which show high grain boundary resistance caused by highly positive grain boundary cores and charge depletion in the adjacent layers [56, 62, 64, 78, 79]. Furthermore, the observed exponential relation between the inter-grain conductivity and the water layer thickness was mathematically derived to be caused by charge depletion of protons. Moreover, transport through a charged depleted region can also be seen as an energy barrier described by an Arrhenius equation. This is exactly what is observed for the inter-grain conductivity measurements presented in Figs. 6.7 and 6.8., where a linear decrease of the activation energies with water layer thickness is observed. Thus, there is consistency between all observations and it can be concluded that the large inter-grain resistance is caused by depletion of protons above the highly positive grain boundaries. This finding should also have general applicability also for other ionic surface transport.

7 Concluding remarks and outlook

Prior to this work, many questions about the fundamentals of protonic transport in porous oxides were unanswered. The relation between the conductivity, the degree of hydration, the acid-base properties of the oxide matrix and concentration of protonic charge carriers of a sample was to a small degree understood. The fundamentals of how the interface between the surface and the water affects the conductivity were barely identified as a question. By using the existing knowledge from literature, with dedicated measurements and investigations in the present work, many of these questions have been addressed.

The discovery of the two series connected transport processes along surfaces, and the understanding of how the interface between the oxides' surface and water layer affects the behaviour of the intra-grain and inter-grain surface conductivity, has brought us a big step forward into understanding the fundamentals of protonic conduction in porous oxides and on oxides' surfaces. The intra-grain conductivity is to a large extent influenced by the interface properties of the water layer and the large inter-grain barrier is shown to be a result of charge depletion caused by the positive grain boundaries in the oxide. This understanding, together with the model for the total ionic transport in porous oxides, opened for more dedicated experiments and analysis to sort out what is affecting the protonic surface transport. The type of protonic charge carrier in porous oxides and the type of charge carrier mechanism is found to be dependent on the acid-base properties of the oxide matrix and the relative humidity. In particular, for acidic surfaces it is shown to change from Grotthuss type migration of protons to a vehicular transport of hydroxonium ions above 60% RH, the humidity level where the water layer starts showing "liquid-like" properties. Moreover, by aliovalent doping of the TiO_2 matrix the acidity of the surface and protonic surface conductivity was shown to increase by donor doping and decrease by acceptor doping the porous oxide. More acidic surfaces lead to higher proton mobility and higher proton concentrations in the water layer.

Many interesting questions about the protonic conduction in porous oxides still remain open. For example, a possible relation between the heat of adsorption, the formation of protons and conductivity is not proven, and the charge carrier in the water layer on strong basic oxides is still to be confirmed to be hydroxide ions. However, more interesting and maybe more important are the aspects that can realise surface protonics for energy conversion purposes, which will be the topic in the rest of this section.

The present work has focused on protonic conduction in porous oxides where the protonic conductivity is many orders of magnitude higher than volume conductivity at ambient conditions. Thus, they can typically be characterised as electrolyte materials for fuel cells and electrolysers, where the material is pure protonic conducting. To realise fuel cells and

electrolysers of porous oxides, development of supporting electrode materials is a key issue. Porous oxides may through an electron-conducting matrix offer a route for efficient mixed-conducting electrodes and hydrogen-separation membranes. A schematic of four types of ceramic-based composite membrane structures and possible applications are shown in Fig. 7.1. Strategies to improve the electrolyte and to develop electrode materials will in the following be discussed briefly.

7.1 Electrolytes – material aspect and optimising

The best protonic conductivity of a porous oxide in this work is found to be in the order of ~10^{-5} S·cm^{-1}. In comparison, the conductivity of a porous nanocrystalline TiO_2 [20] and a porous thin film of 3YSZ [18] is earlier reported to be as high as 10^{-3} S·cm^{-1}, which is grossly one order of magnitude lower than required to utilise the material in energy conversion applications [2]. Through this thesis we have touched upon many parameters that control the protonic surface conductivity. Among the most important are the morphology and specific surface area, and the acidic properties of the surface. Interestingly, a material that is largely optimised in relation to these parameters is already reported. Fujita *et al*. [22] have shown protonic conductivity of porous sample as high as approximately 0.1 S·cm^{-1} at 80 ºC and 90% RH by incorporating sulfonic acid groups in highly ordered mesoporous silica.

An optimised material must, to function as an electrolyte material, be gas tight. With a nano-dimensional pore structure, the electrolyte can be made gas tight by taking advantage of capillary condensation at high RH, intended illustrated in Figure 7.1. Operating at high RH coincides favourably with the highest mobility and concentration of protons. Moreover, the smaller the size of the pores, the easier it is to achieve capillary condensation and simultaneously have a high specific surface area of the material. However, the pores must be large enough to achieve bulk like properties of the water phase yielding high mobility and charge carrier concentration. Obviously, an optimised pore dimension of the material can be found.

The large drawback of porous oxides compared to polymers is that the humidity needs to be kept high during operation to have a gas tight membrane. An advantage is that porous oxides can tolerate higher temperatures than the polymers. Thus, it is easier to foresee porous oxides for electrolysis than for fuel cell purposes, since high steam pressure is advantageous in hydrogen production. All in all, more research focused on finding stable acidic membranes with high surface area should be done. The success of porous oxides relies however, on production of a complete cell included compatible electrode materials.

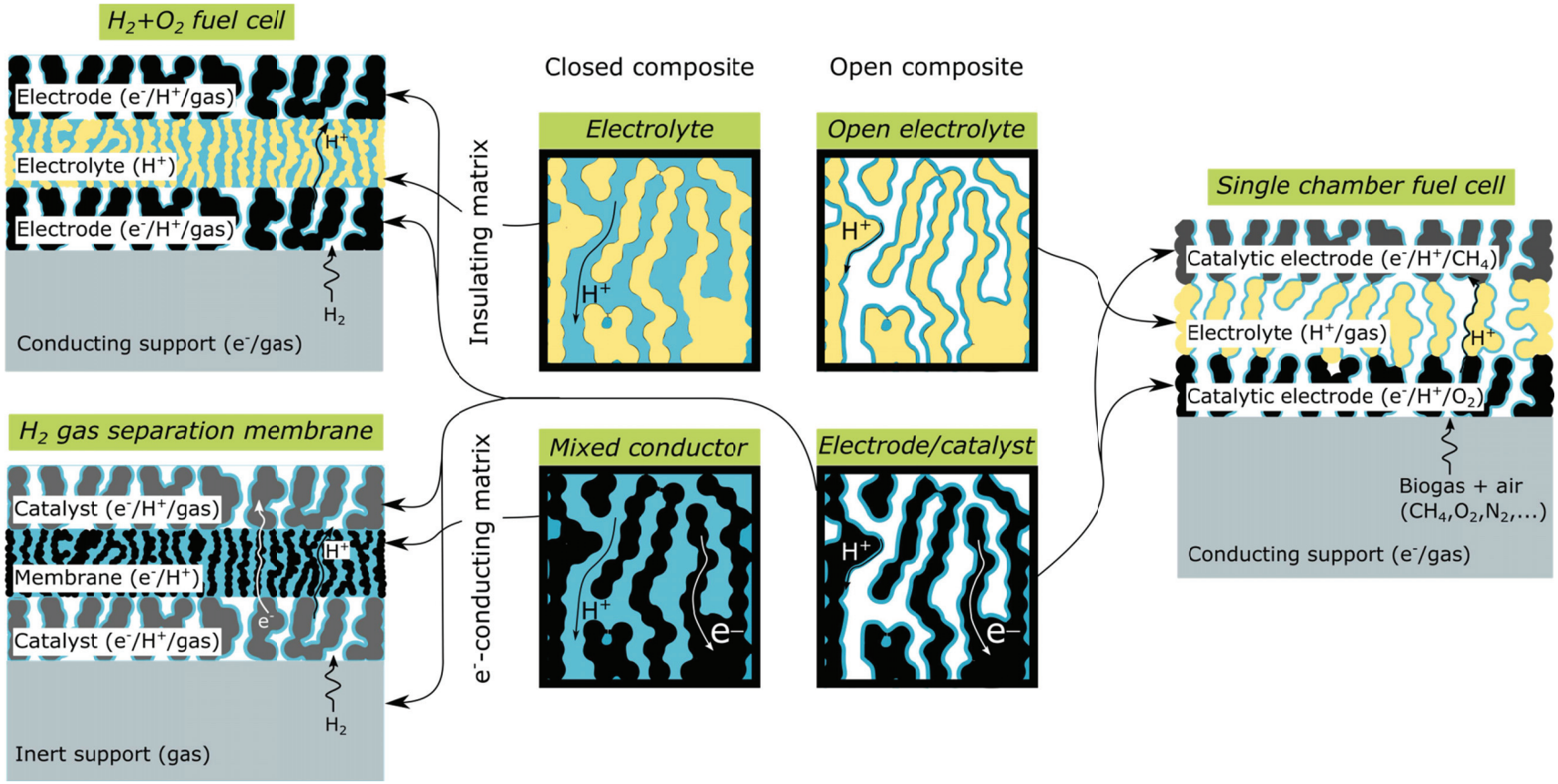

Fig. 7.1. Schematic of the four types of ceramic-based composite membrane structures (middle). The left part shows how a fuel cell (or similarly an electrolyser) and a hydrogen gas separation membrane are assembled with dense ionic or mixed conducting membranes and electrode viz. surface catalyst structures. The right part shows similarly a single chamber fuel cell by using an open electrolyte and two selectively catalytic electrodes.

7.2 Electrodes and mixed conductors – the need for new materials

High efficiency and cheap electrode materials have been challenging to make for all types of proton conducting fuel cells. The largest problems are related to the slow kinetics at the cathode. For the polymers this has been solved by using slurries of nanoparticles of platinum and active carbon. Search for mixed ionic and electronic conducting oxides is the strategy for high temperature proton conductors. Mixed ionic and electronic conduction can to some extent counteract for slow kinetics, by increasing the active area beyond the triple phase boundaries.

The possible parallel transport of protons in the water layer and electronic conduction through the ceramic matrix must be seen as a great advantage when it comes to development of electrodes for porous oxides. Electrodeposited MnO_2 is in literature already proven to show a mixed conduction through the water layer and the matrix with a protonic conductivity of approximately 10^{-4} $S \cdot cm^{-1}$ and an electronic conductivity of approximately 0.01 $S \cdot cm^{-1}$ at 24 ºC under wet conditions (p_{H_2O}=0.022 atm) [82]. By increasing the temperature to 100 ºC and keeping the RH constant, the protonic conductivity of MnO_2 can be estimated to be approximately 10^{-3} $S \cdot cm^{-1}$ assuming similar activation energy as found for 8YSZ in Manuscript III. Increasing the temperature, and consequently the partial pressure of water, is obviously necessary to reach both good protonic and electronic performance and more importantly: higher temperature leads to better catalytic properties. In addition to high active surface area, the catalytic properties of the electrodes are important for fast oxidation and reduction of hydrogen and oxygen, respectively.

Good catalytic reactivity, especially related to the splitting of oxygen and water, is a challenge that must be solved. Doping and introduction of nano particles can be strategies. The discovery of enhanced surface protonic conductivity by donor doping the matrix in Manuscript IV is thus in particularly interesting, as donor doped materials typically display high electronic conductivity and doping usually opens for better catalytic performance. A breakthrough for porous oxides is largely dependent on development of new catalytic electrode materials that perform well at low and intermediate temperatures, and exhibit low material and production costs. Good electrolyte performance is to some extent already proven [10, 20, 22, 27].

References

[1] S. Ramanathan, K.P.K. Kumar, P.K. De, S. Banerjee, *Bull Mater Sci* **28** (2005) (2) 109.

[2] Y. Yamazaki, R. Hernandez-Sanchez, S.M. Haile, *Chemistry of Materials* **21** (2009) (13) 2755.

[3] S.M. Haile, *Acta Materialia* **51** (2003) (19) 5981.

[4] S. Kim, U. Anselmi-Tamburini, H.J. Park, M. Martin, Z.A. Munir, *Advanced Materials* **20** (2008) (3) 556.

[5] C. Wagner, *Berichte der Bunsen-Gesellschaft* **72** (1968) (7) 778.

[6] E. Ruiz-Trejo, J. Kilner, *J Appl Electrochem* **39** (2009) (4) 523.

[7] S. Kim, H.J. Avila-Paredes, S. Wang, C.-T. Chen, R.A. De Souza, M. Martin, Z.A. Munir, *Physical Chemistry Chemical Physics* **11** (2009) (17) 3035.

[8] G. Chiodelli, F. Maglia, U. Anselmi-Tamburini, Z.A. Munir, *Solid State Ionics* **180** (2009) (4–5) 297.

[9] K.D. Kreuer, *Annual Review of Materials Research* **33** (2003) (1) 333.

[10] M.T. Colomer, *Advanced Materials* **18** (2006) (3) 371.

[11] K.-D. Kreuer, *Chemistry of Materials* **8** (1996) (3) 610.

[12] D.J.L. Brett, A. Atkinson, N.P. Brandon, S.J. Skinner, *Chemical Society Reviews* **37** (2008) (8) 1568.

[13] H.J. Avila-Paredes, J. Zhao, S. Wang, M. Pietrowski, R.A. De Souza, A. Reinholdt, Z.A. Munir, M. Martin, S. Kim, *Journal of Materials Chemistry* **20** (2010) (5) 990.

[14] G. Gregori, M. Shirpour, J. Maier, *Advanced Functional Materials* **23** (2013) 5861.

[15] M. Shirpour, G. Gregori, R. Merkle, J. Maier, *Physical Chemistry Chemical Physics* **13** (2011) (3) 937.

[16] H.J. Avila-Paredes, C.-T. Chen, S. Wang, R.A. De Souza, M. Martin, Z. Munir, S. Kim, *Journal of Materials Chemistry* **20** (2010) (45) 10110.

[17] S. Miyoshi, Y. Akao, N. Kuwata, J. Kawamura, Y. Oyama, T. Yagi, S. Yamaguchi, *Solid State Ionics* **207** (2012) (0) 21.

[18] B. Scherrer, M.V.F. Schlupp, D. Stender, J. Martynczuk, J.G. Grolig, H. Ma, P. Kocher, T. Lippert, M. Prestat, L.J. Gauckler, *Advanced Functional Materials* **23** (2013) (15) 1957.

[19] S. Miyoshi, Y. Akao, N. Kuwata, J. Kawamura, Y. Oyama, T. Yagi, S. Yamaguchi, *Chemistry of Materials* **26** (2014) (18) 5194.

[20] I.G. Tredici, F. Maglia, C. Ferrara, P. Mustarelli, U. Anselmi-Tamburini, *Advanced Functional Materials* **24** (2014) (32) 5137.

[21] S. Raz, K. Sasaki, J. Maier, I. Riess, *Solid State Ionics* **143** (2001) (2) 181.

[22] S. Fujita, A. Koiwai, M. Kawasumi, S. Inagaki, *Chemistry of Materials* **25** (2013) (9) 1584.

[23] J.J. Fripiat, A. Jelli, G. Poncelet, J. André, *The Journal of Physical Chemistry* **69** (1965) (7) 2185.

[24] Z. Chen, C. Lu, *Sensor letters* **3** (2005) (4) 274.

[25] K.-S. Chou, T.-K. Lee, F.-J. Liu, *Sensors and Actuators B: Chemical* **56** (1999) (1–2) 106.

[26] H.J. Avila-Paredes, E. Barrera-Calva, H.U. Anderson, R.A. De Souza, M. Martin, Z.A. Munir, S. Kim, *Journal of Materials Chemistry* **20** (2010) (30) 6235.

[27] M.T. Colomer, F. Rubio, J.R. Jurado, *Journal of Power Sources* **167** (2007) (1) 53.

[28] K.D. Kreuer, W. Weppner, A. Rabenau, *Materials Research Bulletin* **17** (1982) (4) 501.
[29] I. Langmuir, *Journal of the American Chemical Society* **38** (1916) (11) 2221.
[30] S. Brunauer, P.H. Emmett, E. Teller, *Journal of the American Chemical Society* **60** (1938) (2) 309.
[31] D.B. Asay, S.H. Kim, *The Journal of Physical Chemistry B* **109** (2005) (35) 16760.
[32] E.-M. Köck, M. Kogler, B. Klötzer, M.F. Noisternig, S. Penner, *ACS Applied Materials & Interfaces* **8** (2016) (25) 16428.
[33] R. Sato, S. Ohkuma, Y. Shibuta, F. Shimojo, S. Yamaguchi, *The Journal of Physical Chemistry C* **119** (2015) (52) 28925.
[34] E.L. Fuller, H.F. Holmes, C.H. Secoy, J.E. Stuckey, *The Journal of Physical Chemistry* **72** (1968) (2) 573.
[35] E. McCafferty, A.C. Zettlemoyer, *Discussions of the Faraday Society* **52** (1971) (0) 239.
[36] G. Korotcenkov, Editor, *Chemical Sensors: Simulation and Modeling Volume 3: Solid-State Devices, Volum 3*, Momentum Press (2012).
[37] G.C.C. Costa, S.V. Ushakov, R.H.R. Castro, A. Navrotsky, R. Muccillo, *Chemistry of Materials* **22** (2010) (9) 2937.
[38] P.C.H.a.R. Rajagopalan, *Principles of colloid and surface chemistry*, CRC Press (1997).
[39] A.L. Buck, *Journal of Applied Meteorology* **20** (1981) (12) 1527.
[40] W. Thomson, *Phil. Mag. S.* **42** (1871) (282) 448.
[41] M.L. González-Martín, L. Labajos-Broncano, B. Jańczuk, J.M. Bruque, *J Mater Sci* **34** (1999) (23) 5923.
[42] Y. Shimizu, H. Arai, T. Seiyama, *Sensors and Actuators* **7** (1985) (1) 11.
[43] E.G. Derouane, J.C. Védrine, R.R. Pinto, P.M. Borges, L. Costa, M.A.N.D.A. Lemos, F. Lemos, F.R. Ribeiro, *Catalysis Reviews* **55** (2013) (4) 454.
[44] J.H. Anderson, G.A. Parks, *The Journal of Physical Chemistry* **72** (1968) (10) 3662.
[45] H. Mizoguchi, M. Hirano, S. Fujitsu, T. Takeuchi, K. Ueda, H. Hosono, *Applied Physics Letters* **80** (2002) (7) 1207.
[46] G. Tocci, A. Michaelides, *The Journal of Physical Chemistry Letters* **5** (2014) (3) 474.
[47] G.A. Parks, *Chemical Reviews* **65** (1965) (2) 177.
[48] H.H. Kung, *Journal of Solid State Chemistry* **52** (1984) (2) 191.
[49] S.H. Lee, J.C. Rasaiah, *The Journal of Chemical Physics* **139** (2013) (12) 124507.
[50] D. Riccardi, P. König, X. Prat-Resina, H. Yu, M. Elstner, T. Frauenheim, Q. Cui, *Journal of the American Chemical Society* **128** (2006) (50) 16302.
[51] S. Kale, J. Herzfeld, *Angewandte Chemie International Edition* **51** (2012) (44) 11029.
[52] K.D. Kreuer, I. Stoll, A. Rabenau, *Solid State Ionics* **9–10, Part 2** (1983) (0) 1061.
[53] K.-D. Kreuer, S.J. Paddison, E. Spohr, M. Schuster, *Chemical Reviews* **104** (2004) (10) 4637.
[54] M.J.G. Jak, S. Raz, L.N. van Rij, J. Schoonman, I. Riess, *Solid State Ionics* **143** (2001) (2) 205.
[55] J. Hinterberg, A. Adams, B. Blumich, P. Heitjans, S. Kim, Z.A. Munir, M. Martin, *Physical Chemistry Chemical Physics* **15** (2013) (45) 19825.
[56] X. Guo, J. Maier, *Journal of The Electrochemical Society* **148** (2001) (3) E121.
[57] X. Guo, W. Sigle, J. Fleig, J. Maier, *Solid State Ionics* **154–155** (2002) 555.
[58] H.J. Avila-Paredes, K. Choi, C.-T. Chen, S. Kim, *Journal of Materials Chemistry* **19** (2009) (27) 4837.
[59] X. Guo, W. Sigle, J. Maier, *Journal of the American Ceramic Society* **86** (2003) (1) 77.

[60] C. Kjølseth, H. Fjeld, Ø. Prytz, P.I. Dahl, C. Estournès, R. Haugsrud, T. Norby, *Solid State Ionics* **181** (2010) (5–7) 268.
[61] J. Maier, *Progress in Solid State Chemistry* **23** (1995) (3) 171.
[62] X. Guo, R. Waser, *Progress in Materials Science* **51** (2006) (2) 151.
[63] M.A. Brown, A. Goel, Z. Abbas, *Angewandte Chemie International Edition* **55** (2016) (11) 3790.
[64] N.H. Perry, S. Kim, T.O. Mason, *J Mater Sci* **43** (2008) (14) 4684.
[65] C. Tande, D. Perez-Coll, G.C. Mather, *Journal of Materials Chemistry* **22** (2012) (22) 11208.
[66] T. Norby, *Solid State Ionics* **28–30, Part 2** (1988) 1586.
[67] M. Yoon, K. Suh, S. Natarajan, K. Kim, *Angewandte Chemie International Edition* **52** (2013) (10) 2688.
[68] H. Knözinger, *The Hydrogen Bond-Recent Developments in Theory and Experiments*, North-Holland, Amsterdam (1976).
[69] S. Hayun, T.Y. Shvareva, A. Navrotsky, *Journal of the American Ceramic Society* **94** (2011) (11) 3992.
[70] A. Loken, T.S. Bjorheim, R. Haugsrud, *Journal of Materials Chemistry A* **3** (2015) (46) 23289.
[71] H. Takahashi, I. Yashima, K. Amezawa, K. Eguchi, H. Matsumoto, H. Takamura, S. Yamaguchi, *Chemistry of Materials* (2017).
[72] K. Rokyeon, C. Suyeon, P. Won-Goo, C. Deok-Yong, O. Se-Jung, S.-M. Romuald, B. Patrick, P. Je-Geun, Y. Jaejun, *Journal of Physics: Condensed Matter* **26** (2014) (14) 146003.
[73] L.-H. Ye, A.J. Freeman, *Physical Review B* **73** (2006) (8) 081304.
[74] A. Løken, *To be submitted* (2017).
[75] A.A. Levchenko, G. Li, J. Boerio-Goates, B.F. Woodfield, A. Navrotsky, *Chemistry of Materials* **18** (2006) (26) 6324.
[76] L.T. Zhuravlev, *Colloids and Surfaces A: Physicochemical and Engineering Aspects* **173** (2000) (1–3) 1.
[77] S. Kim, J. Maier, *Journal of the European Ceramic Society* **24** (2004) (6) 1919.
[78] O.J. Durá, M.A. López de la Torre, L. Vázquez, J. Chaboy, R. Boada, A. Rivera-Calzada, J. Santamaria, C. Leon, *Physical Review B* **81** (2010) (18) 184301.
[79] S. Kim, J. Maier, *Journal of The Electrochemical Society* **149** (2002) (10) J73.
[80] S. Haile, *Journal of materials research* **13** (1998) (06) 1576.
[81] O. Björneholm, M.H. Hansen, A. Hodgson, L.-M. Liu, D.T. Limmer, A. Michaelides, P. Pedevilla, J. Rossmeisl, H. Shen, G. Tocci, E. Tyrode, M.-M. Walz, J. Werner, H. Bluhm, *Chemical Reviews* **116** (2016) (13) 7698.
[82] S.W. Donne, F.H. Feddrix, R. Glöckner, S. Marion, T. Norby, *Solid State Ionics* **152–153** (2002) (0) 695.